

Evaluation of digital x-ray imaging technologies for tuberculosis screening

by

Ryan Scott Mann

A thesis
presented to the University of Waterloo
in fulfillment of the
thesis requirement for the degree of
Master of Applied Science
in
Electrical and Computer Engineering

Waterloo, Ontario, Canada, 2014

© Ryan Scott Mann 2014

Author's Declaration

I hereby declare that I am the sole author of this thesis. This is a true copy of the thesis, including any required final revisions, as accepted by my examiners.

I understand that my thesis may be made electronically available to the public.

Abstract

Tuberculosis is a major concern in low- and middle-income countries, but may be diagnosed using standard chest x-rays. Conventional film-screen x-ray detectors require more maintenance than digital x-ray detectors and need a good supply chain of developer chemicals and film, which make them difficult to maintain in low-infrastructure areas of the world. Current digital x-ray technology is prohibitively expensive for this market, although it brings the possibility of tele-radiology and tele-medicine, quicker diagnosis time, and virtually no cost per test compared to other diagnostics for tuberculosis. This thesis examines the requirements on a small-sized, low-cost digital x-ray detector for this application.

Two small x-ray detectors were integrated into x-ray systems, then characterized for detector performance using metrics known as modulation transfer function, noise power spectrum, and detective quantum efficiency. The system designs and the results of the experiments are shown. Details are also shown about the setup of the x-ray lab, including the door interlock system for a lead-lined x-ray cabinet.

To determine whether a smaller x-ray detector is diagnostically accurate enough for tuberculosis diagnosis compared to full-size chest radiography equipment, a medical study was designed and run using a web-based survey of radiologists in Pakistan, where tuberculosis is a recognized disease.

In an attempt to compare x-ray detector performance, MATLAB® code was written to measure the modulation transfer function, noise power spectrum, and detective quantum efficiency of x-ray systems. The details about this code, and challenges in simulating the performance of physically different detectors are explained in the thesis.

Acknowledgements

I would like to thank my supervisor, Professor Karim Karim, for giving direction, suggestions, and feedback throughout the journey of these past 20 months of my life. You are a great mentor and I have received a lot from you as a professor, an engineer, and a family man.

Thanks to all my fellow research group members over the past years: Dr. Nicholas Allec, Dr. Shiva Abbaszadeh, Umar Shafique, Kyung-Wook Shin, Chris Scott, Sina Ghanbarzadeh, Max Palumbo, Zhechen George Du, Mursal Ashrafi, Saeedeh Ghaffari, and Ahmet Camlica. You have made this journey so much easier with your positive and helpful attitudes and amazing work ethic.

Thank you to those who have helped me with my work: Thank you, André Fleck, for helping with experiments at the Grand River Hospital. Thank you, Dr. Ian Cunningham, for valuable advice, and to both you and Mike McDonald for help characterizing the x-ray detectors. Thank you, Greg Friday and Richard Barber, for helping me set up the x-ray lab safely. Thank you, Dr. Waseem Mirza, Kainat Baig, and Mohammad Yusuf at the Aga Khan University Hospital in Karachi, Pakistan, for all your help with the tuberculosis efficacy study. Thank you, Daniel Severn, for your contribution to the statistical analysis of the efficacy study. Thank you Dr. Carí Borrás, Prof. Jock Mackay, Prof. Stefan Steiner, Plinio Morita, Leila Rezai, Prof. Cecilia Cotton and Susanne Santi for helping me design the medical studies or to critique them.

Thank you, Kevin and Sarah, Kyle, Karl, Ben, Aaron, Matt, Nic, Aaron, Darren, and others, for your support and encouragement.

Thank you, Mom and Dad: Your encouragement over these past couple of years, and your genuine interest in my work have been invaluable. Thanks for praying, caring, and listening. Thank you, Janessa: You are a great sister and friend, and I have learned so much from you. Thank you, Deanna, for believing in me, and for keeping me company through any weather. You are my best friend and encourager.

Finally, the best thanks to Jesus Christ: You are my daily motivation and my source of hope and joy. This is all for you.

To my parents, to Deanna,
And to Jesus Christ.

Table of contents

Author's Declaration	ii
Abstract	iii
Acknowledgements	iv
List of tables	x
List of figures	xii
1 Introduction	1
1.1 Motivation	1
1.2 Tuberculosis	1
1.3 Tuberculosis diagnostics	2
1.4 X-ray technology	3
1.4.1 Digital x-ray imaging	3
1.4.2 Indirect vs. direct detection	4
1.4.3 Cost reduction by detector area reduction	4
1.5 Detector quality comparison metrics	4
1.5.1 Spatial resolution	5
1.5.2 Edge spread function	5
1.5.3 Line spread function	5
1.5.4 Modulation transfer function	6
1.5.5 Noise power spectrum	6
1.5.6 Detective quantum efficiency	7
1.6 Diagnostic quality comparison metrics	7
1.7 Outline of the report	8

2	X-ray system design	10
2.1	Design goals	10
2.2	X-ray system	10
2.3	X-ray generator	11
2.3.1	Laboratory setup	12
2.3.2	X-ray cabinet interlock	13
2.3.3	X-ray source characterization	14
2.4	Industrial, indirect-detection x-ray detector	14
2.4.1	System design	15
2.4.2	FPGA software design	16
2.4.3	Synchronization circuit design	18
2.4.4	Lab setup	19
2.4.5	Issues	20
2.5	Neo-natal, direct-detection x-ray detector	21
2.5.1	System design	21
2.5.2	Lab setup	23
2.6	Personal computer	24
2.7	Discussion	24
2.7.1	X-ray detector	24
2.7.2	Personal computer	25
2.8	Summary	25
3	Industrial x-ray detector characterization	27
3.1	Phantom characterization	27
3.2	Detective quantum efficiency	28
3.3	Discussion	31
3.4	Summary	32
4	Neo-natal x-ray detector characterization	33
4.1	Phantom characterization	33
4.1.1	Phantom design	33
4.1.2	Images	34
4.2	Modulation transfer function	35
4.3	Discussion	38
4.4	Summary	39

5	Region-of-interest efficacy study	40
5.1	Objective	40
5.2	Methods	40
5.2.1	Statistical analysis	41
5.2.2	Patients	42
5.2.3	Image cropping	43
5.2.4	Image selection	43
5.2.5	Radiologists	43
5.3	Results	43
5.3.1	Outliers	45
5.3.2	Qualitative questionnaire	45
5.4	Conclusions	46
5.5	Summary	46
6	DQE simulations	47
6.1	Summary	49
7	Conclusions and recommendations	50
7.1	Contributions	50
7.2	Conclusions	50
7.2.1	X-ray generator	51
7.2.2	X-ray detector	51
7.2.3	Tuberculosis efficacy study	52
7.2.4	DQE simulations	52
7.3	Recommendations	53
7.3.1	X-ray generator	53
7.3.2	X-ray detector	53
7.3.3	Tuberculosis efficacy study	53
7.3.4	DQE simulations	54
	References	55
	APPENDICES	58
A	Synchronization FPGA code	58

B	Synchronization boards	63
C	X-ray source cabinet	65
D	Parts lists	72
E	Detector images	74
F	Efficacy study information letter	78
G	Monte Carlo simulations of an indirect x-ray detector	80
	G.1 Summary	80
	G.2 Background	80
	G.3 Development of simulation code	81
	G.3.1 Linear attenuation coefficient calculation	81
	G.3.2 X-ray absorption	82
	G.3.3 X-ray scattering	82
	G.3.4 Creation of electron-hole pairs	83
	G.3.5 Electron travel and scatter	83
	G.3.6 Trajectories of visible-spectrum photons	84
	G.3.7 Code	84
	G.4 Results	84
	G.4.1 Standard screen results	85
	G.4.2 Plus screen results	86
	G.4.3 High screen results	88
	G.5 Analysis	89
H	DQE MATLAB® code	90
I	Photos	92
	Glossary	98

List of tables

2.1	Comparison of portable x-ray sources.	12
2.2	PerkinElmer XRD0820 properties.	15
2.3	XRD0820 DE2 push button functionality, from left to right.	17
2.4	XRD0820 frame grabber serial port pinout.	19
2.5	Relevant properties of the Texas Instruments SN65LVDS050D.	19
2.6	X-ray detector purchase options.	21
2.7	Relevant properties of the ON Semiconductor MC14049.	23
2.8	Properties of the computing system.	24
3.1	PerkinElmer XRD0820 design criteria ranking.	32
4.1	Comparison of phantom choices.	33
4.2	DRTech FLAATZ-330N design criteria ranking.	38
5.1	The number of radiologists/raters in each survey are shown.	41
5.2	The number of x-rays in each survey are shown.	41
5.3	The number of rater observations in each survey are shown.	42
5.4	Overall sensitivity and specificity results for tuberculosis.	44
5.5	Radiologists' perception of difficulty of diagnosis.	46
7.1	X-ray detector design criteria ranking.	52
D.1	Parts for the x-ray cabinet interlock	72
D.2	Parts included with the XRD0820	72
D.3	Parts for the synchronization circuitry	73
D.4	Parts used with the FLAATZ-330N	73
G.1	Relevant properties of DRZ scintillator screens.	81

G.2	Relevant chemical properties of Gd, O, and S.	82
G.3	Numerical settings and results for DRZ Standard simulation.	85
G.4	Numerical settings and results for DRZ Plus simulation.	86
G.5	Numerical settings and results for DRZ High simulation.	88

List of figures

1.1	Collapse of right upper lobe due to TB.	2
1.2	Comparison of the relative cost for the system and for each diagnosis, the sensitivity, and the time to diagnose of three major technology-based tuberculosis diagnostics [8], [9].	3
1.3	Direct and indirect conversion detector schema.	4
1.4	An x-ray opaque edge over a detector creates a pattern to measure the modulation transfer function (MTF).	5
1.5	Examples of ESF, LSF and ideal MTF curves.	6
1.6	Venn diagram to depict “sensitivity” and “specificity” metrics.	8
2.1	Digital x-ray system diagram.	11
2.2	X-ray generator cabinet and safety interlock.	13
2.3	Estimated X-ray energy spectrum of the SR-115 source.	14
2.4	Digital x-ray system diagram using the PerkinElmer XRD0820.	15
2.5	Timing diagram for capturing an x-ray frame with the XRD0820.	16
2.6	Usage of the DE2’s buttons, switches, LEDs and hex displays.	17
2.7	FPGA software state machine design	18
2.8	Digital x-ray system diagram using the DRTech FLAATZ-330N.	21
3.1	X-ray phantom setup at the Grand River Hospital.	28
3.2	XRD0820 with the DQE <i>Pro</i>	28
3.3	DQE for XRD0820.	29
3.4	LSF for XRD0820.	29
3.5	MTF for XRD0820.	30
3.6	NPS for XRD0820.	30
3.7	Comparison of the XRD0820 with other x-ray systems.	31

4.1	Custom anthropomorphic phantom with tuberculosis.	34
4.2	Phantom images, taken with the FLAATZ-330N.	35
4.3	FLAATZ-330N set up for DQE measurements.	36
4.4	ESF for FLAATZ-330N.	36
4.5	LSF for FLAATZ-330N.	37
4.6	MTF for FLAATZ-330N. The green dashed line represents the ideal modulation transfer function (MTF).	37
4.7	ESF and MTF for FLAATZ-330N, calculated by Dr. Ian Cunningham. . .	37
5.1	Examples of questions on web survey.	41
5.2	Diagram showing important body parts included in cropped images.	43
5.3	For each radiologist, full sense./spec. is compared with two-image.	44
5.4	Percentages of incorrect non-TB diagnoses seen by each rater.	45
B.1	Synchronization board schematic for XRD0820.	63
B.2	Synchronization board layout for XRD0820.	64
B.3	Synchronization board schematic for FLAATZ-330N.	64
B.4	Synchronization board layout for FLAATZ-330N.	64
C.1	3D Front/Top View	65
C.2	Cabinet front view	66
C.3	Door top view	67
C.4	Top view	68
C.5	Side view	69
C.6	Cable feedthrough (Bottom 3D View)	70
C.7	Interlock board schematic	70
C.8	Interlock board layout	71
E.1	Edge image for calculating MTF in the x-direction of the XRD0820.	74
E.2	Edge image for calculating MTF in the y-direction of the XRD0820.	75
E.3	Edge image for calculating MTF in the x-direction of the FLAATZ-330N . .	76
E.4	Edge image for calculating MTF in the y-direction of the FLAATZ-330N. .	77
G.1	Simulated x-ray photon and electron absorption locations, standard DRZ screen.	85

G.2	Lateral spread of visible-wavelength photon absorption locations, standard DRZ screen.	86
G.3	Simulated x-ray photon and electron absorption locations, plus DRZ screen.	87
G.4	Lateral spread of visible-wavelength photon absorption locations, plus DRZ screen.	87
G.5	Simulated x-ray photon and electron absorption locations, high DRZ screen.	88
G.6	Lateral spread of visible-wavelength photon absorption locations, high DRZ screen.	89
I.1	X-ray phantom setup at the Grand River Hospital	92
I.2	X-ray setups at the Grand River Hospital and Robarts Research Institute.	92
I.3	SourceRay SR-115 on its stand	93
I.4	X-ray source safety labels	93
I.5	X-ray cabinet door interlock system	94
I.6	University of Waterloo lab setup with PC	94
I.7	Robarts Research Institute lab setup with FLAATZ-330N	95
I.8	Robarts Research Institute lab setup for FLAATZ-330N characterization	95

“Ask yourselves what you would want others to do for you, then do it for them first.”

— Jesus

1 | Introduction

1.1 Motivation

Lung diseases are some of the biggest causes of death today. Diseases like asthma, chronic obstructive pulmonary disease (COPD), pneumonia, and tuberculosis (TB) are treatable, but have a higher toll on low-income countries. Currently 235 million people suffer from asthma, a disease that primarily affects children [1]. In 2005, 3 million people died of COPD, accounting for 5% of all deaths worldwide that year [2]. Pneumonia kills around 1.2 million children under the age of 5 every year, which is more than AIDS, malaria and TB combined [3].

Lung diseases like these can all be diagnosed with standard chest radiography. As a proof of concept, tuberculosis has been chosen for this project as the target lung disease. This report examines the design and characterization of a digital x-ray system for region-of-interest tuberculosis diagnosis.

1.2 Tuberculosis

According to the 2011 estimates from the World Health Organization, over 1.4 million people worldwide died as a result of tuberculosis; 60% of TB cases were in south-east Asia and the western Pacific, and one quarter were in Africa; less than 2% of TB-related deaths were in the Americas [4]. In Pakistan, the National Tuberculosis Control Programme quotes WHO's statistics to say that 177/100,000 people are tested positive with tuberculosis every year [5]. Tuberculosis is treated with pharmaceuticals, but many people in developing countries are not diagnosed early enough for the drugs to be effective. TB screening reduces the mortality of tuberculosis-infected people in many developing countries, if only it could be made inexpensive and accessible to rural areas.

In developing a digital x-ray screening system for tuberculosis, specific requirements for diagnosis were drafted. They are based on the visual characteristics of pulmonary tuberculosis, radiation safety considerations, and the specifications of industrial-grade (and therefore less expensive) x-ray detectors.

Tuberculosis appears differently in the chest radiograph in primary and reactivation tuberculosis [6]. Primary tuberculosis prefers to reside in the upper lobes of the lung; and

anterior and posterior segments can be involved. The air-space in the lungs is homogeneous with no well-defined borders. Miliary (lesions resembling millet seeds) development occurs less than 3% of the time, especially in children less than 3 years old. The hilar (upper right lung near the spine) and paratracheal (throat) lymph nodes swell up (denoted “adenopathy”), and in 15% of cases, bilateral hilar adenopathy may also occur. Sometimes the only evidence for primary tuberculosis is a single pleural effusion (buildup of fluid between the layers of tissue that line the lungs and chest cavity). The most common places for TB are the anterior segment of the right upper lobe (See Figure 1.1) or the middle segment of the right middle lobe. Unfortunately, primary tuberculosis most commonly appears as a normal chest radiograph [6].

In reactivation tuberculosis, the most likely places to find it in the lungs are in the upper lobes and the higher portion of the lower lobes. The front of the upper lobes is almost never the only place that it can be found. Radiologists look for an air-space consolidation that appears patchy or confluent [6], increased linear density to the hilum on the same side of the lungs, cavitation, but not for lymph node swelling. In chronic cases, the lesions become more irregular and pronounced. Cavities that may develop have a somewhat thick wall, smooth inner surface, and no air-fluid level. It would appear as multiple shadows.

In general, when choosing an x-ray detector for pulmonary tuberculosis, image contrast is most important, and resolution is important, but less so [7]. In general, the size of tuberculosis is not the major concern for a standard x-ray system, and requirements will be driven largely by the contrast ratio, x-ray sensitivity, and cost of the system.

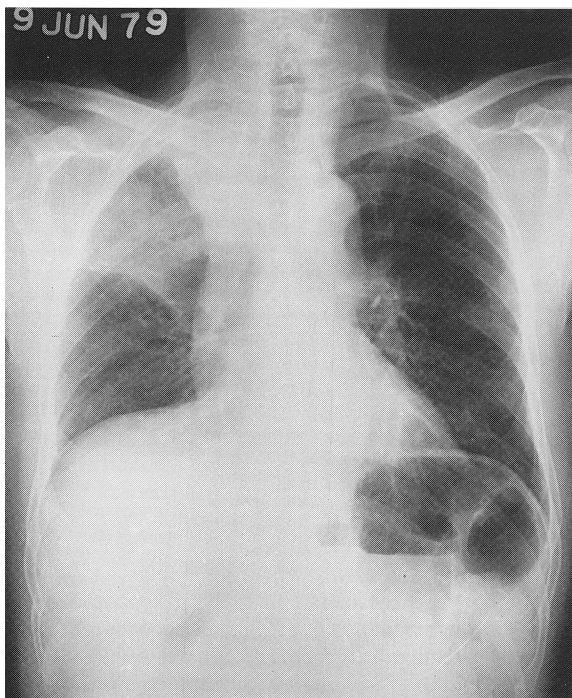


Figure 1.1: Collapse of right upper lobe due to TB. Also an elevated right side of diaphragm and prominent right side of heart border [6].

1.3 Tuberculosis diagnostics

There are several current methods for diagnosing tuberculosis worldwide. Besides simple symptom questionnaires, tuberculosis is diagnosed by sputum and smear microscopy, chest radiography, and a nucleic acid amplification test (NAAT) called the Xpert MTB/RIF system. While the diagnostic accuracy of the Xpert MTB/RIF system is the highest of all the methods, and the cost of an LED fluorescence microscopy (FM) system is the lowest, the cost per test and the time to result of digital chest x-ray suggest a more affordable,

accurate alternative for low-income countries that requires no consumables. Some comparisons of the three technology-based methods are shown in Figure 1.2.

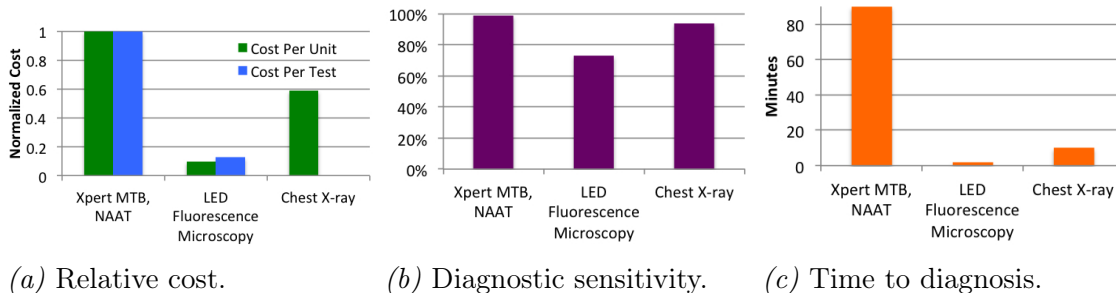


Figure 1.2: Comparison of the relative cost for the system and for each diagnosis, the sensitivity, and the time to diagnose of three major technology-based tuberculosis diagnostics [8], [9].

1.4 X-ray technology

For more than a century, x-ray radiation has been used to peer into the way things work with a deeper understanding. It was on November 8, 1895 when Wilhelm Roentgen first discovered these high-energy photons, and soon imaging systems were being created worldwide [10]. The first famous image from this new discovery was Roentgen’s own wife’s hand, and immediately x-ray imaging became an amazing advancement in the field of medicine, allowing accurate diagnosis of bone fractures and breaks, followed by innumerable other injuries, illnesses and diseases. Roentgen was awarded the Nobel Prize for physics in 1901 [10].

X-ray detectors have gone through an evolution in the past hundred years from the first rugged field radiological vehicles used by Marie Curie in WWI [11] to today’s state-of-the-art digital x-ray detectors for mammography, radiography, fluoroscopy and computed tomography. For decades, film-screen detectors were used, requiring photo development before a radiologist or technician could determine if the image had the right exposure and focus. One step in the right direction was called computed radiography (CR), which consisted of phosphoric materials—either in a powder or a columnar film structure—that stored charge when radiated with x-rays. The phosphor screens could be read out by shining a particular wavelength of red light in a raster pattern and detecting the emitted blue or green light.

1.4.1 Digital x-ray imaging

Digital flat-panel x-ray imagers have several distinct advantages. First, just as digital cameras lowered the cost per photo and the time to develop dramatically, a digital x-ray detector allows for instant readout by the radiologist, allowing for repositioning of the patient or a change of x-ray exposure or dose levels without forcing the patient to wait minutes or hours before being allowed to leave the radiology room. Besides this, digital

x-rays are more portable, easily stored, and easily edited or enhanced for more accurate diagnosis.

1.4.2 Indirect vs. direct detection

Two basic types of digital x-ray detectors exist on the market, separated by the process of converting x-rays to charge. Indirect x-ray detectors rely on a material that absorbs x-ray photons while emitting visible-spectrum photons to a thin film photodiode array or a charge coupled device array that converts light into charge carriers.

These phosphor-based layers are called scintillators. Direct x-ray detectors, such as those based on amorphous selenium, rely on a material that directly absorbs x-ray photons and converts the energy into charge carriers that can be collected by a thin-film transistor (TFT) array. The two types of detectors are shown in Figure 1.3.

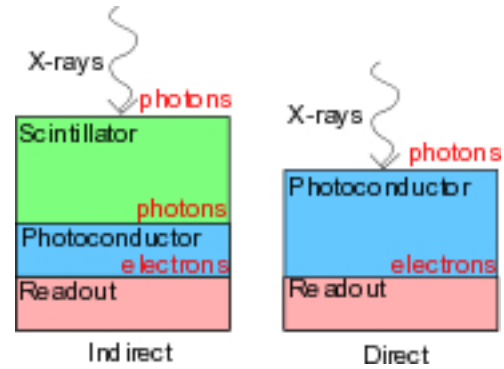


Figure 1.3: Direct and indirect conversion detector schema.

1.4.3 Cost reduction by detector area reduction

To make the cost of digital x-ray technology accessible in developing countries, this project examines the efficacy of a digital x-ray system based on a smaller-than-average x-ray detector. The cost of a smaller x-ray panel decreases because of three main aspects of the design: First, because TFT arrays are manufactured on a glass substrate with a certain large area, building a smaller panel would mean more panels could be constructed at the same time, decreasing the average cost per panel. Second, with fewer pixels in the array, there will be fewer off-panel integrated circuits required to read out the electrical signals or to control the gates of the transistors. Finally, the cost of the scintillator is highly dependent on its area, so in total, a smaller panel is less expensive to build.

Instead of using a conventional 17-inch square flat-panel x-ray detector, two smaller flat-panel x-ray detectors were chosen to be characterized: one that is 8 inches square, and one that is 8" x 10". These x-ray detectors are characterized in chapters 3 and 4.

Given that a smaller x-ray detector is not large enough to x-ray the average adult's full chest, a medical study was carried out to investigate the impact on the diagnostic accuracy of using two single-lung images rather than a full chest x-ray. This medical study is explained in chapter 5.

1.5 Detector quality comparison metrics

To determine the quality of x-ray detectors, there are several measurements that can be done. These include spatial resolution, the edge spread function, line spread function,

modulation transfer function, noise power spectrum, and the detective quantum efficiency.

1.5.1 Spatial resolution

The spatial resolution of a detector is essentially the measurement of the ability of a detector to resolve two small distinct and adjacent objects. A higher spatial resolution shows that a detector can resolve smaller, closer objects. In this document, spatial resolution will typically be measured in line pairs per millimeter (lp/mm) or cycles per millimeter.

1.5.2 Edge spread function

The edge spread function (ESF) is a one-dimensional array of pixel intensities that are calculated from the average pixel intensities in each column, or in each row, where an opaque object with a straight edge is covering half of the row or column, as shown in Figure 1.4. This technique is known as the “slanted edge test” [12]. Near the straight edge, there will be a distribution of light intensity that denotes the blurring or spreading of photons or charge within the detector photosensitive material. The slanted edge is used to estimate the “pre-sampled” theoretical curve before the spatial discretization due to the finite pixel pitch. With increased rows and columns to sample the ESF, the pre-sampled curve’s estimation accuracy is increased. The ESF can be described by:

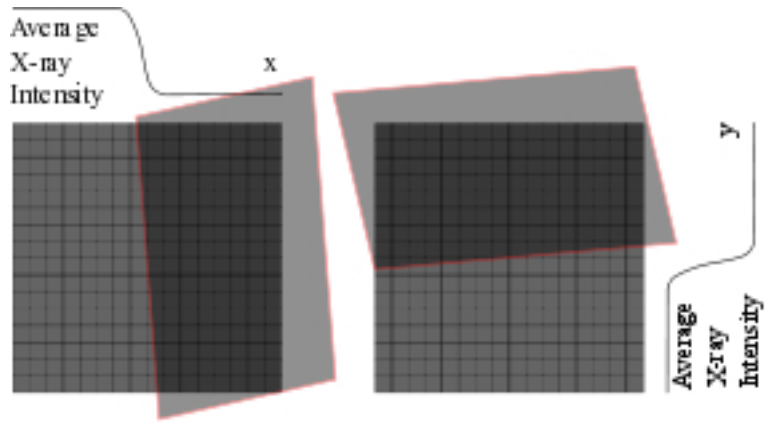


Figure 1.4: An x-ray opaque edge over a detector creates a pattern to measure the modulation transfer function (MTF).

Where x is the pixel in the row, X is the input array of pixel intensities, μ is the average pixel intensity, and σ is the standard deviation. An example of an ESF is in Figure 1.5a.

$$ESF(x) = \frac{X - \mu}{\sigma}$$

Where x is the pixel in the row, X is the input array of pixel intensities, μ is the average pixel intensity, and σ is the standard deviation. An example of an ESF is in Figure 1.5a.

1.5.3 Line spread function

The line spread function (LSF) is the numerical differentiation of the edge spread function with respect to space. Because the ideal ESF is shaped as a step function, the line spread function (LSF) typically resembles a single peak, with the ideal curve (before sampling, which is limited by the pixel pitch) being a Dirac-Delta function. It can be described by:

$$LSF(x) = \frac{d}{dx}ESF(x)$$

An example of a line spread function is in Figure 1.5b.

1.5.4 Modulation transfer function

The modulation transfer function is the Fourier transform of the line spread function, in the spatial domain. The ideal MTF curve, limited only by the pixel pitch, is in the shape of the modulus of a sinc function ($|\sin(x)/x|$). It can be described by:

$$MTF(\omega) = \frac{|LSF(\omega)|}{|LSF(0)|} = \frac{|\mathcal{F}[LSF(x)]|}{|\mathcal{F}[LSF(x)]|_{\omega=0}}$$

An example of an ideal modulation transfer function is in Figure 1.5c.

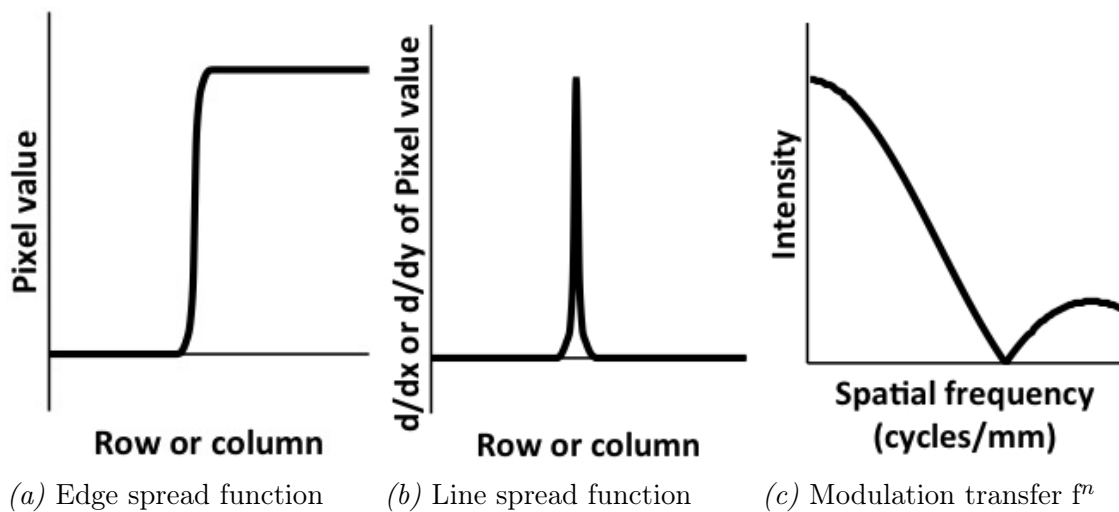


Figure 1.5: Examples of an edge spread function, its line spread function, and an ideal modulation transfer function.

1.5.5 Noise power spectrum

The noise power spectrum is a measure of the noise (random pixel values) that occurs in a detector image, in the spatial domain. It measures the noise power spectral density at each spatial frequency. Thus, a noise power spectrum is visualized as a two-dimensional array to show spatial frequencies in both rows and columns simultaneously.

To measure the noise power spectrum, several unilluminated images would be captured using the detector. At each row and column pixel location, the average pixel value is taken for the same pixel across all images. A Fourier transform of this 2D pixel array of average dark values reveals the noise power spectrum.

1.5.6 Detective quantum efficiency

The detective quantum efficiency is a spatial frequency-dependent noise figure of merit. The detective quantum efficiency (DQE) is the change between the input SNR_i and the output SNR_o of a cascaded imaging system (See [13]). It can therefore be described as this ratio:

$$DQE_i(\omega) = \frac{SNR_i^2(\omega)}{SNR_{i-1}^2(\omega)}$$

The DQE can also be derived from the MTF and the noise power spectrum (NPS), as follows:

$$DQE(\omega) = \frac{G \times MTF^2(\omega)}{q \times X \times NPS(\omega)}$$

In this equation, G is the gain factor of the system stage, X is the exposure in mR , and q is the SNR^2 per exposure ($no./mm^2mR$).

Because the DQE can be derived from the NPS and MTF, any detector system (digital x-ray, digital optical, or even film) can be characterized and compared this way. The DQE measurement provides an objective comparative tool to compare detector systems with respect to both signal-to-noise ratios and spatial resolution simultaneously. It is a standard metric used by medical physicists to determine the quality and safety of medical diagnostic devices.

1.6 Diagnostic quality comparison metrics

In terms of the efficacy or capability of a particular diagnostic system or procedure, one can measure the sensitivity (proportion of true positives) or specificity (proportion of false negatives). For example, in a sampling of N diagnostic tests, let us say that T represents the true number of tuberculosis cases, F is the true number of disease-free cases, τ is the number of tuberculosis cases measured by the diagnostic system in question, and ϕ is the number of disease-free cases measured by the diagnostic system. Thus the sensitivity (s_{sense}) and specificity (s_{spec}) would be described as such:

$$s_{sense} = \tau/T$$

$$s_{spec} = \phi/F$$

As shown, N does not figure into the equations. While it is true that $N = T + F$, even so:

$$s_{sense} \neq 1 - s_{spec}$$

Because of this, these two metrics must be estimated separately, as depicted in Figure 1.6. For a very good estimation, one must find a diagnostic method that can very closely approximate T and F , the true number of cases that have or do not have disease, respectively. This diagnostic method would be considered the “gold standard.” For tuberculosis, bacterial culturing is considered the gold standard.

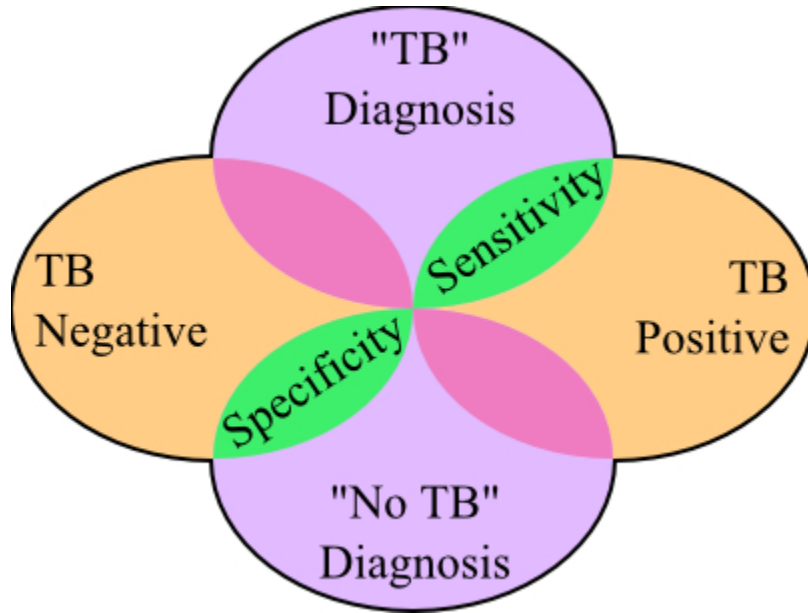


Figure 1.6: This Venn diagram depicts the “sensitivity” and “specificity” metrics for a Tuberculosis efficacy study. The left and right ovals represent the true diagnoses of the patients, either TB -free or TB-positive, respectively. The top and bottom ovals represent the diagnoses of the radiologists using the particular diagnostic technique, which may include correct and incorrect diagnoses. The green sections of the diagram represent the proportion of correct diagnoses.

1.7 Outline of the report

This introductory section described the intended application of the project: region-of-interest tuberculosis screening using digital chest x-rays. Following this, other diagnostic alternatives to digital chest x-rays were mentioned, and some background on x-ray technology was shown. Also described were various ways to compare the performance of x-ray detectors (namely ESF, LSF, MTF, NPS, and DQE) and diagnostic tools (namely the sensitivity and specificity).

In this project, there were three main components:

X-ray system integration and characterization

X-ray system integration (Chapter 2) and characterization (Chapters 3 and 4) was done to investigate possible digital x-ray systems that would be feasible for use in tuberculosis screening programs in the developing world. Using an industrial, indirect-detection x-ray detector, a neo-natal direct-detection x-ray detector, and x-ray sources in the lab at the University of Waterloo and at Robarts Research Institute, three system integrations were required:

1. Industrial x-ray detector with the Robarts x-ray source
2. Neo-natal x-ray detector with the University of Waterloo lab x-ray source
3. Neo-natal x-ray detector with the Robarts x-ray source

Region-of-interest tuberculosis diagnosis medical study

Because the cost reduction mechanism in this project is the smaller area of the x-ray detectors, this medical study (Chapter 5) investigated the effect on diagnostic accuracy of radiologists when shown two single-lung x-rays rather than a full chest x-ray, which is the standard procedure.

DQE simulations

Following on from the ROI TB medical study, these simulations (Chapter 6) were intended to be a way to determine if the digital x-ray systems under test would result in high diagnostic accuracy without performing any clinical trials.

2 | X-ray system design

2.1 Design goals

The main goal of this project is to determine the technical requirements for a low-cost digital x-ray system for tuberculosis diagnosis. The systems designed and experiments run during this project should help determine what characteristics of low-cost digital x-ray systems will be appropriate for region-of-interest pulmonary tuberculosis diagnosis. Here are some of the problems this project should solve:

- Required x-ray detector performance for the application
- Cost feasibility for low-income or middle-income countries
- Efficacy of region-of-interest tuberculosis diagnosis using small chest x-rays

Here are some of the overall criteria on the x-ray system design that will be considered, in order of importance:

- Component cost
- Portability and ruggedness
- AC power compatibility overseas
- Ease of integration
- Image performance compared to the medical-grade chest x-ray detectors

More specific criteria for each system component will be discussed in the following sections.

2.2 X-ray system

Two low-cost digital x-ray systems were designed using a combination of purchased parts and custom hardware and software. An overall system diagram is shown in Figure 2.1. This diagram contains four main components:

- Portable x-ray source/x-ray generator
- Digital flat panel x-ray detector
- Control interface and source-detector synchronization
- Personal computer (PC) and monitor

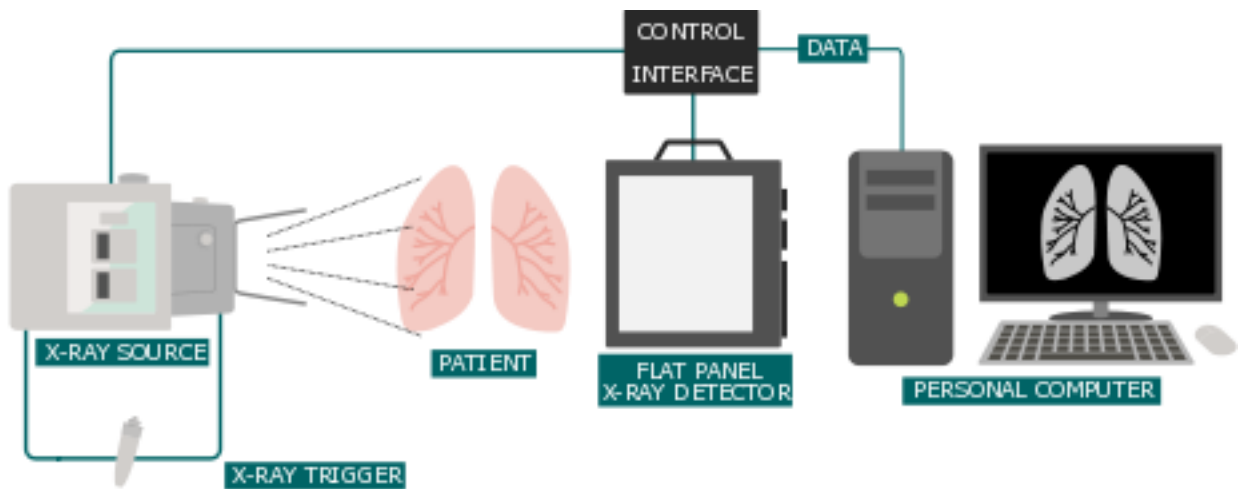


Figure 2.1: Digital x-ray system diagram. This, and other system diagrams were designed by Deanna Loewen.

Each of the components will be explained further in the following sections.

2.3 X-ray generator

For the application of remote tuberculosis screening, the choice of an x-ray generator has several criteria, based on some precedents of tuberculosis screening [14]:

- Must be portable, for use in the field
- Must be powerful enough for chest radiography (100 kVp)
- Must be able to work in 110V and 230V power grids, for use in the lab and in the field
- Should come equipped with a stand, for use in the field
- Must meet Canadian, US or European federal regulations, for use in the lab
- Should be under \$15000

Table 2.1: Comparison of portable x-ray sources.

Manufacturer	MinXray		SourceRay	
Product Name	HF100+	HF120	SR115	SR130
Cost for unit	\$10805	\$15243	\$11095	\$13644
Cost with stand	\$14030	\$18468	\$12095	\$15144
Power at 70kV	1.8kW	2.2kW	1kW	2.1kW
Tube voltage (kV)	40-100	40-120	40-100	40-100
Tube current (mA)	20, 25, or 30	14-60	15	15 or 30
Exposure duration (s)	0.08 - 4	0.01 - 5	0.01 - 4	0.01 - 4
Source heat capacity (kHU)	20	65	20	30
System weight (lb)	90.5	96.5	80	100
Input power	100-140 or 200-260V, must specify	100-260V, 50/60Hz	115/230V, 50/60Hz	115/230V, 50/60Hz

Two portable x-ray source distributors in the United States (SourceRay and MinXray) had possible options. Each of the portable sources available has a stationary anode type, rather than a rotating anode, and is certified for use in North America. Relevant specifications are shown in Table 2.1.

The HF100+, though the cheapest option, was not a good choice because of its inability to work in both 110V and 220V power systems. The next cheapest option was the **SourceRay SR115**, and it met all the requirements. Although it is the lowest power and is limited to a single value of tube current, it should be good for the proof of concept, and perhaps in the field, and its price tag is competitive.

2.3.1 Laboratory setup

In the laboratory at the university, the portable x-ray generator must be contained within a lead-lined cabinet so that the radiation level is suitable for daily use by researchers. Though a stand was purchased with the SR115 (See Figure I.3 in Appendix I), the generator had to be hung inside a lead-lined cabinet with an interlocking mechanism to shut off the x-rays when the cabinet door is open, as shown in Figure 2.2a. Detailed drawings of the x-ray cabinet may be found in Appendix C. A red lightbulb is connected to the power switch of the x-ray generator, so the light will illuminate whenever the x-ray generator is powered on. This cabinet and x-ray source setup were safety certified by the Ontario Electrical Safety Authority and the Ontario Ministry of Labour's Health and Safety department.



(a) X-ray generator in the cabinet.

(b) X-ray interlock and hand switch.

Figure 2.2: X-ray generator cabinet and safety interlock.

2.3.2 X-ray cabinet interlock

In order to ensure that the x-ray source will not radiate x-rays while the door is open, an interlock switch was built. This switch breaks the connection between the x-ray trigger hand switch and the x-ray generator. When the door is closed, the connection is made, and it is now possible to trigger an x-ray exposure.

The x-ray hand switch (pictured in Figure 2.2b), has a four-wire modular connector like a phone cable. The hand switch has two active switch positions - one to prepare the x-ray beam, and one to cause the actual exposure. If the “exposure” button is not held down for the full x-ray duration set on the x-ray generator, the exposure is canceled.

The interlock switch consists of a mechanical switch already built into the x-ray cabinet from previous usage, and a custom interlock with modular connectors and the four signals required for operation. The four wires contain the following signals:

- X-ray Exposure
- X-ray Exposure ground/return
- X-ray Prep
- X-ray Prep ground/return

The mechanical switch in the interlock is used to break the connection in the “X-ray Exposure” signal. In this way, the x-ray beam may be prepared, but the x-ray exposure cannot happen until the door is completely shut. For the x-ray interlock circuit and corresponding printed circuit board (PCB), see Appendix C.

2.3.3 X-ray source characterization

The SourceRay SR-115 x-ray source was characterized using “Spekcalc Light”, a free program for estimating the spectrum of tungsten anode x-ray sources. The software uses three references ([15], [16], [17]). Using an anode theta of 15 degrees, 0.7mm of aluminum filtration, and a peak energy of 100keV, the spectrum shown in Figure 2.3 was estimated. The smooth curve is due to *bremstrahlung* (“braking radiation”), and the two peaks are due to electromagnetic radiation from the k-alpha and k orbitals of tungsten. For a better approximation, more specific details would need to be known about the x-ray source.

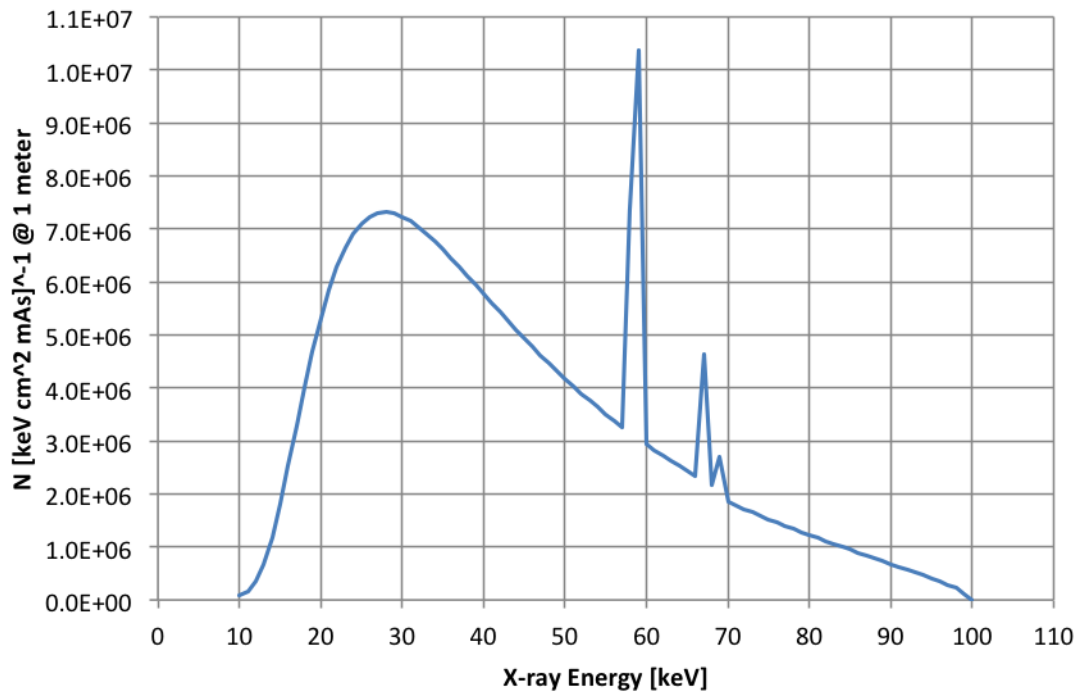


Figure 2.3: Estimated X-ray energy spectrum of the SR-115 source.

2.4 Industrial, indirect-detection x-ray detector

Central to the x-ray diagnostic system is the digital x-ray detector. The majority of the cost of an x-ray system comes from the detector. During the project, two different x-ray detectors were used, with different characteristics and capabilities. The first to be purchased and used was a small, 8-inch square, industrial-grade indirect-detection digital

x-ray detector from PerkinElmer. An older model, the XRD0820 was built for industrial purposes, not for medicine, but was useful for initial prototyping. The XRD0820 x-ray sensing is based on a Gadox scintillator. For more information on Gadox scintillators and their physics, please refer to Appendix G.

Table 2.2 displays the pertinent information about the x-ray detector.

Table 2.2: PerkinElmer XRD0820 properties.

Detector architecture	Indirect detection with scintillator
Scintillator	Gd ₂ O ₂ S DRZ-Plus (208μm thick)
Pixel architecture	a-Si TFT pixels
Active area	204.8x204.8mm ²
Number of pixels	1024x1024
Pixel pitch	200μm
ADC	16 bits

2.4.1 System design

To set up the XRD0820 as a system with an x-ray generator, several components had to be designed and built, described in the following sections. The detector comes with a peripheral component interconnect (PCI) frame -grabber card. A new frame capture can be triggered using signals on an RS232 serial cable. A simple visual depiction of the system that was used for detector characterization is in Figure 2.4.

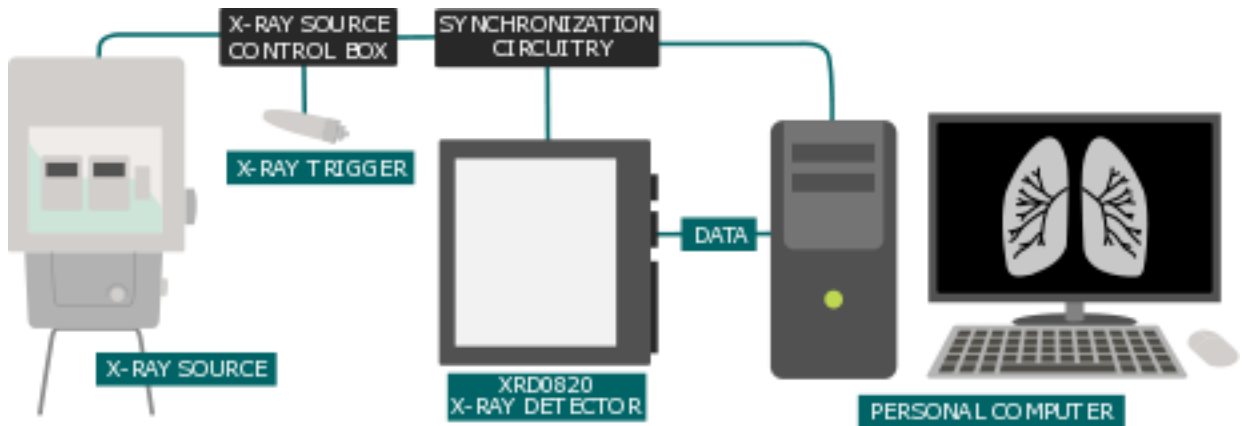


Figure 2.4: Digital x-ray system diagram using the PerkinElmer XRD0820.

There are some intricacies to the functionality of the XRD0820. First of all, an image (or an array of pixel values) is called a “frame”. While powered on and connected to the x-ray imaging software (XIS) on the computer in “continuous integration mode,” the biasing voltage across the pixels is powered on, and light photons from the scintillator are collected as electron-hole pairs. Until the charge stored at the pixel—corresponding to the pixel value—is reset by the software, the charge will continue to be collected on the pixel capacitor.

To synchronize the detector’s frame integration with a set x-ray generator exposure time, it is necessary to first read out the image from the detector. This readout simultaneously sends the image data to the frame grabber PCI card on the computer and also resets all the charges integrated on the pixels, thereby zeroing the frame. Since the photodetector bias voltage is not turned off in this mode, the pixels will immediately recommence their charge integration. It is at this time that the x-ray beam should be turned on in order to create a useful radiographic image. After the intended exposure length, the frame is read out again, this time with useful information. To synchronize with the x-ray source, which can have a BNC cable input or output, two TTL signal are sent from the x-ray source indicating, first, that the x-ray beam is being prepared, and second, that the x-ray exposure is about to occur. A timing diagram (Figure 2.5) will suffice to show the needed circuit design. It is important to note that the XIS detector software had to be in “external trigger” mode for this scheme to work.

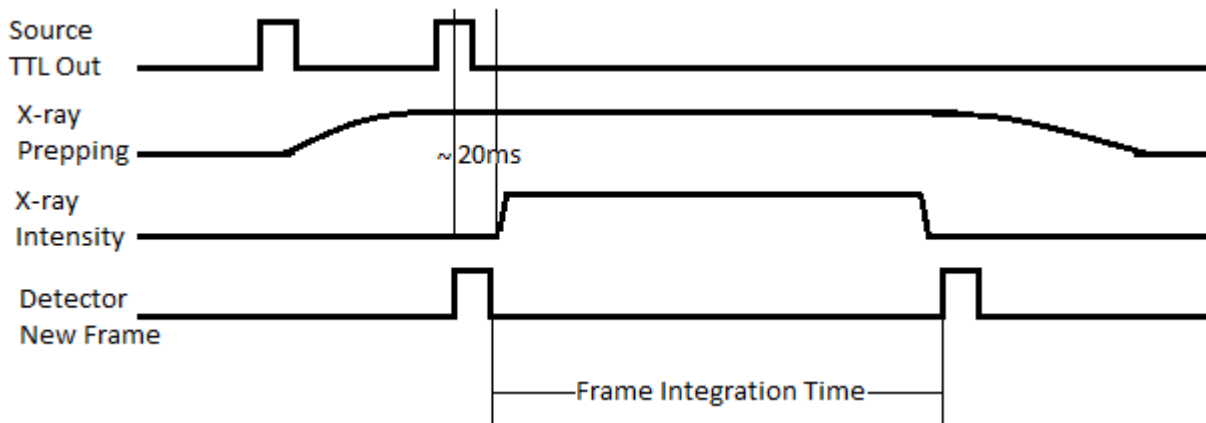


Figure 2.5: Timing diagram for capturing an x-ray frame with the XRD0820.

2.4.2 FPGA software design

Since an Altera DE2 field programmable gate array (FPGA) education board was available in the laboratory, it was used as the software for the synchronization. The DE2 comes with several toggle switches, a hexadecimal display, and push buttons. The basic usage of the board is shown in Figure 2.6. The system was designed to have two “modes”: the EDIT mode, in which the desired frame exposure time is selected in terms of seconds and milliseconds, and RUN mode, which acts as a slave to the x-ray generator and resets the detector frame bits and captures a new image.

The DE2 board is used as follows:

- The hexadecimal display shows the duration of the image integration in seconds, as 00.000. Times may be selected in 10ms increments, and in 1s increments.
- The “Integration LED” is lit when the software is waiting for the frame to integrate (is illuminated for the number of seconds that are set).

- The EDIT mode switch switches between EDIT and RUN modes. The LED above the switch illuminates to show that the system is in EDIT mode.
- The Input LED illuminates when a signal is being sensed from the x-ray generator control box, which is used to trigger a new x-ray frame integration.
- The Trigger LED illuminates when a signal is being sent to the XRD0820 frame grabber card to initiate the “grabbing” of a new frame from the detector.
- The push buttons are used in EDIT mode to select the frame integration time. They operate as shown in Table 2.3.

Table 2.3: XRD0820 DE2 push button functionality, from left to right.

Button	1	2	3	4
Increment or Decrement	Inc.	Dec.	Inc.	Dec.
Interval	1s		10ms	

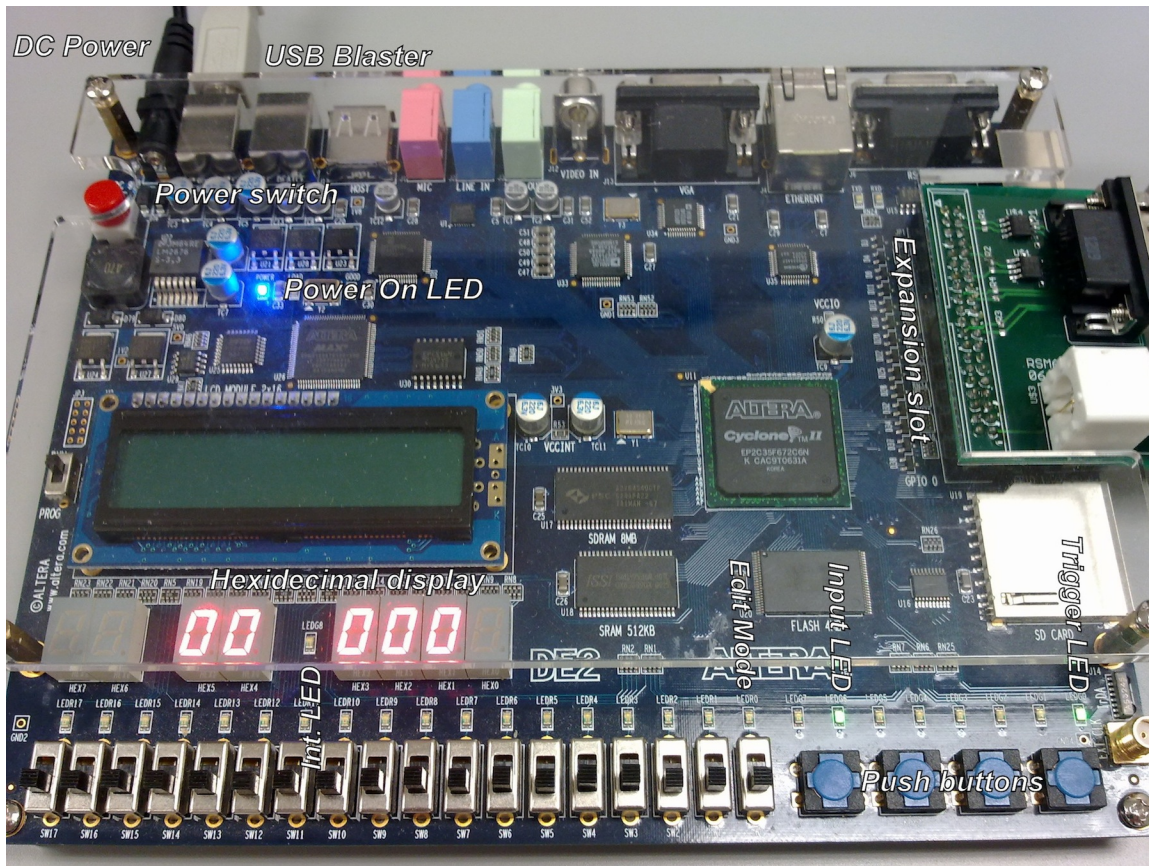


Figure 2.6: Usage of the DE2’s buttons, switches, LEDs and hex displays.

The FPGA software design of the synchronization circuit revolved around the state machine shown in Figure 2.7. The Altera DE2 uses VHDL to program its FPGA. This language

TBView Controller Software State Machine

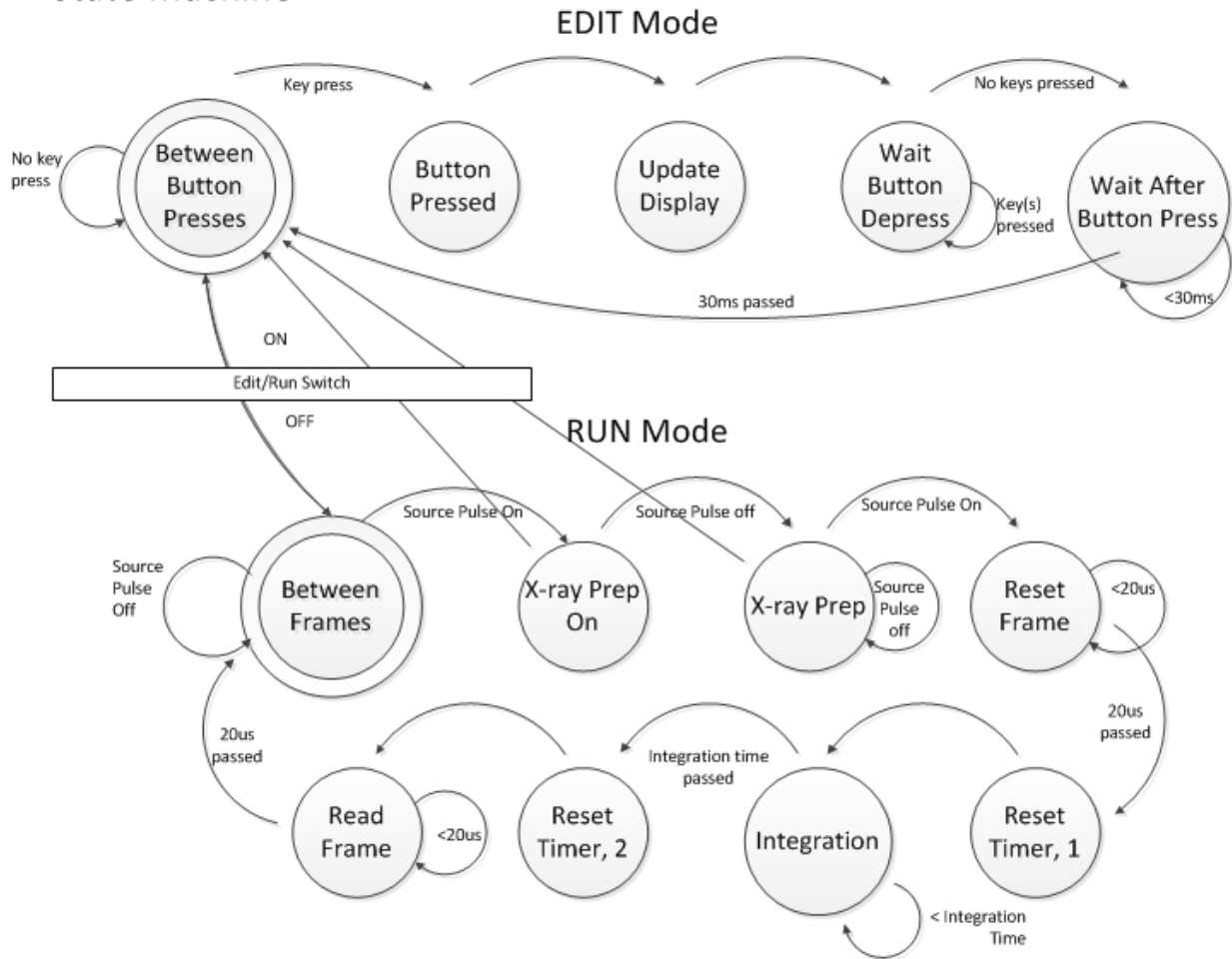


Figure 2.7: FPGA software state machine design

was used to implement the state machine. For the commented VHDL code, please refer to Appendix 7.3.4.

2.4.3 Synchronization circuit design

Since the Altera DE2 board comes with two slots for general purpose input/output (GPIO) pins, these were used as the interface to the x-ray source (with a BNC cable) and to the XRD0820 frame grabber PCI card (with a DB9 serial cable). The FPGA software handles the incoming pulses from the x-ray source, and sends signals to the frame grabber card to initiate frame resets.

The frame grabber uses low-voltage differential signaling (LVDS) over the serial cable. Seven of the nine pins are used, as shown in Table 2.4. For the synchronization scheme described in Section 2.4.2, only the TRIG IN signals were used, but all were connected from the cable to the Altera board in case they were needed in the future.

Table 2.4: XRD0820 frame grabber serial port pinout.

Signal	Type	Function	Pin
TRIG IN ⁺	input	Trigger a frame read	3
TRIG IN ⁻			8
FR EN ⁺	output	Frame enabled	1
FR EN ⁻			6
FR SYNC ⁺	output	Frame synchronization	2
FR SYNC ⁻			7
NA ⁺	N/C	Unused	4
NA ⁻			9
GND	ground	Ground	5

To send a signal using LVDS, an integrated circuit (IC) was used that takes two inverted signals from separate GPIO pins and converts them into the specified levels for LVDS. The LVDS chip chosen was the Texas Instruments SN65LVDS050D. It is designed to drive 100Ω loads and operate from a 3.3V power supply, which is available on a GPIO pin of the DE2 board. Relevant information about this chip is shown in Table 2.5.

Table 2.5: Relevant properties of the Texas Instruments SN65LVDS050D.

Property	Value	
Unit price	\$5.10	
Supply voltage	3.3V	typical
High-level input voltage	2V	minimum
Low-level input voltage	0.8V	maximum
Driver output voltage	0V	2.4V
Current supply	10mA (typ)	16mA (max)

No conversion was necessary for the signals that acted as inputs to the GPIO board from the frame grabber, as the FPGA software was able to handle these inputs using a simple subtraction of the two signals.

A PCB was designed and built that would easily sit on top of the DE2 board, onto a 40-pin header connector. For details on the circuit and board, please refer to Appendix B.

2.4.4 Lab setup

To use the x-ray detector (XRD) in the laboratory for characterization, several components were necessary:

- XRD power supply and cables
- XRD 0820 detector and data interface cable
- Desktop PC, power cable, keyboard and mouse

- HD monitor, power cable and HDMI cable
- Altera DE2 FPGA board, power cable, and USB Blaster cable
- Custom trigger board, DB9 cable, and BNC cable

Once all the system components are properly connected, the DE2 board must be programmed via USB, and the x-ray imaging software (XIS) must be set up with the following steps:

1. Start the XIS program in Windows XP.
2. A dialog box will ask if you wish to start in Interrupt Mode. Select “Yes.” The XIS will attempt to connect to the XRD0820 if properly connected via the data interface cable.
3. From the XIS menu, select Detector → Mode → Ext. Trigger mode, which allows the x-ray source to control the frames.
4. To acquire an image, set up XIS by selecting Acquire → Continuous mode and select a number of frames that is at least double the number of images you wish to acquire.
5. When the acquisition is over, save, and/or restart continuous acquisition mode.

If necessary, there is offset and gain correction in XIS to correct for non-linearity of and non-uniformity of pixels within the array. The XRD0820 was shipped with a CD containing offset and gain correction files for the default pixel gain setting. The software can link to these files, and the current and following images will all have this correction applied.

2.4.5 Issues

The XRD0820 was not ideal, for a few reasons:

- The type of scintillator did not lead to high enough quality images, and could not be replaced due to the manufacturing process used.
- The PC image software was originally written in German, and not fully translated into English. Specifically, more advanced menu options were not translated.
- The system relies on proprietary cable systems.
- Designing and building a product synchronization system would not be cost-effective, and would require a larger quality management system and more regulation.

2.5 Neo-natal, direct-detection x-ray detector

The MTF results for the XRD0820 were low, due to the low pixel pitch and the thickness of the scintillator. DRTech in Korea produces a high-MTF, direct conversion, amorphous-selenium-based, small x-ray detector for neo-natal use. This detector was chosen for its low cost and high resolution (by virtue of the direct-conversion photoconductive layer), among other small-size x-ray detector options, tabulated in Table 2.6. The cost of the FLAATZ-330N is normally higher for regular customers.

Table 2.6: X-ray detector purchase options.

Manufacturer	DRTech	Teledyne Dalsa	PerkinElmer
Product	FLAATZ 330N	SkiaGraph8	XRD0822
Quote (USD)	\$15000	\$44000	\$29500
Detector architecture	TFT and a-Se direct conversion layer	CMOS and Gadox scintillator	TFT and Gadox scintillator
Active area (mm ²)	264x198	196x192	204.8x204.8
Number of pixels	2048x1536	2048x2000	1024x1024
Pixel pitch (μm)	129	96	200
ADC bits	14	12	14

2.5.1 System design

A digital x-ray system can be easily built with the FLAATZ-330N digital x-ray detector. The unit comes with a control box, a frame -grabber Ethernet PCI card for a Windows computer, a hand switch to trigger x-rays, and a hand switch control box to synchronize the detector to an x-ray source. A simple visual depiction is in Figure 2.8. An Ethernet

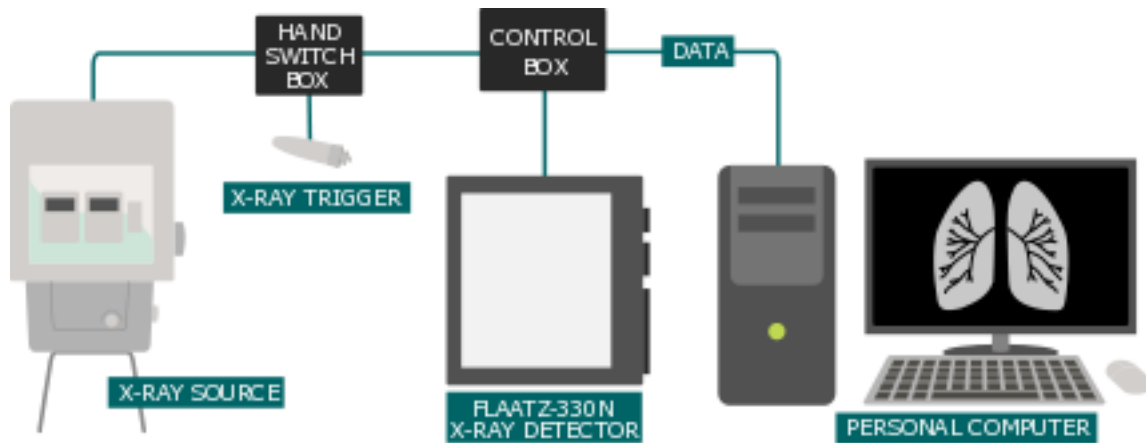


Figure 2.8: Digital x-ray system diagram using the DRTech FLAATZ-330N.

connection is made between the x-ray detector’s control box, and the frame grabber I/O

expansion card. Using a command line application (“Terminal Emulator”), the settings on the x-ray detector can be changed:

- Ready/PREP delay time (1s). This is the time for the x-ray beam to be prepped.
- Exposure delay time (0ms). This is the time between pressing the x-ray beam button and the time the x-ray beam will begin.
- Exposure window time (250ms). This is the length of time the detector will integrate the image.

For setup with the University of Waterloo lab, the system was used as follows:

1. User presses the hand switch fully, which sends the PREP and Exposure signals at the same time. The x-ray generator receives both signals and preps the x-ray beam.
2. The SR115 is designed to begin the x-ray exposure exactly 1 second after the prep button is pressed, if the exposure button is also pressed. The detector begins to integrate the collected charge at this time.
3. The x-ray beam continues for the preset time on the SR115, and the detector integrates the image for the duration of the Exposure Window Time.

Thus, the time settings should be as follows:

- Detector Ready/PREP delay time = 1000ms
- Detector Exposure delay time = 0s
- Detector Exposure window time = 100ms + Source Timer
- Source Timer= 3.0mAs (100ms) or more

The calibration software that comes with the detector combines the gain and offset correction files from the manufacturer, then prompts for several x-ray exposures to make sure the average pixel values are in the center of the 14-bit numerical range. In the laboratory, a setting on the source of 45kVp, and 3.0mAs resulted in the best image quality after running the calibration software.

The DRTech detector was compatible with the SR-115 portable x-ray source without modification or customization. However, for the DQE measurements, one PCB had to be built to connect another x-ray source to the detector from a BNC connector. The schematics and layout of this PCB are found in Appendix B.

The main circuit functionality comes from two 6.8k Ω pull-up resistors that draw the Ready/Prep or Exposure signals up to 10V after the x-ray trigger is released. Because of a TTL-level (5V) inverter (MC14049 legacy chip), the Exposure signal is 0V when the x-ray trigger is not being pressed, but rises to 10V when the trigger shorts the signal to ground. The input of the x-ray source controller circuit has a low input resistance, and requires the inverter to drive at least 9V, thus the power supply used was a 10V dc source. Relevant properties of the ON Semiconductor MC14049 are shown in Table 2.7.

Table 2.7: Relevant properties of the ON Semiconductor MC14049.

Property	Value	
Supply voltage V_{DD}	3V (min)	18V (max)
Output voltage V_{OH}	$(V_{DD} = 10V)$	9.95V (typ)
Output voltage V_{OL}	$(V_{DD} = 10V)$	0V (typ)
Output Drive Current I_{OH}	$(V_{DD} = 10V)$	-2.6mA source (typ)
Output Drive Current I_{OL}	$(V_{DD} = 10V)$	16mA sink (typ)

2.5.2 Lab setup

For these measurements, which were performed at Robarts Research Institute in London, Ontario, the detector acted as the master, and the source as the slave. This scheme was easier to implement than the opposite scheme, which was used for the XRD0820. In this case, the hand switch for the phone cable to the x-ray generator was sensed on a custom circuit board, pulled up to 5V by a power supply, and then inverted by a transistor-transistor logic (TTL)-level CMOS inverter chip. When the X-ray Exposure switch was closed on the hand switch a 5-volt pulse was sent across a cable to the x-ray source controller, causing the emission of x-rays.

The following equipment was required for the measurements at Robarts:

- FLAATZ 330N detector
- Detector data cable, Ethernet cable, long 4p4c phone cable
- Control box, power cord, power adapter, 120-240V transformer
- Switch box, hand switch
- Custom PCB for synchronization, DC power supply
- BNC to BNC cable
- PC power cords x3, monitor cable
- Desktop computer, mouse, keyboard, monitor
- Hardware security key, USB stick

To acquire images, the following steps must be taken.

1. Open Terminal Emulator in Windows 7. Turn on the detector control box. Set the timing of the detector as specified. Turn off the detector. Close Terminal Emulator.
2. Open FConsole1 image acquisition software. Start a new work session (“Emergency” works fine, to avoid entering patient information).
3. When prepping the x-ray beam, press and hold the hand switch in the first position.

4. When the x-ray beam is ready, press and hold the hand switch in the second position until the x-ray exposure is complete.
5. After several seconds, the image will appear on the screen. It may be edited, and saved to disk.

2.6 Personal computer

The personal computer component of the system consists of a desktop tower computer, a high definition monitor, a keyboard, and a mouse. The choice of the PC had only three specific criteria:

- Must have a full-size PCI expansion slot
- Should have high definition video for monitor
- Must run Windows XP for x-ray detector software

Listed in Table 2.8 are some properties of the computing system:

Table 2.8: Properties of the computing system.

Operating systems	Windows 7 Professional, 64-bit
	Windows XP Professional, 32-bit
Processor	Intel Core i5-2320 @ 3GHz
Memory (RAM)	4GB
Expansion slots	PCI (32-bit)
	PCIe x1 (2 available)
	PCIe x16
Monitor	24.0" LCD
	1920x1080
	HDMI, DVI & D-Sub

2.7 Discussion

This section discusses some of the pros and cons of design decisions made in the project.

2.7.1 X-ray detector

Since the performance of the x-ray detector is central to the success of the system, there exist several good reasons to move from the PerkinElmer XRD0820 to the DRTech FLAATZ-330N. In terms of weight and bulk, the XRD0820 is much more cumbersome,

making transportation more difficult. However, it would more likely survive if dropped. The system integration was also much easier with the FLAATZ-330N, not requiring custom parts and PCBs. The FLAATZ line of products also comes with an optional feature of “auto-triggering,” which means that the synchronization between the generator and detector would occur automatically, with no wires or cables required.

From a government regulation perspective, the XRD0820 is worse because it is considered an industrial x-ray detector, not “medical-grade”. However, the FLAATZ-330N comes with software that requires bug fixes and downloads, which could make it more difficult to certify, because each new software fix would require new certification. The XRD0820’s XIS is more stable. That said, the XRD0820 requires custom FPGA code that would also require re-certification if ever a bug needed to be fixed.

In terms of logistical considerations: The FLAATZ detector can only be operated in temperatures between 5 degrees and 35 degrees Celsius, because of the selenium layer that could shatter or peel off. Besides this, the unit must be stored in temperatures between 0 degrees and 40 degrees Celsius. These, and other environmental specifications, would make it difficult to be used in less temperate locations, and specifically the target locations for low-cost digital x-ray systems.

Simply on the merits of being an easy-to-integrate, user-friendly experience, the FLAATZ-330N is a better choice going forward. In the end, the performance of these devices will have the final say. These results are shown in Chapters 3 and 4.

2.7.2 Personal computer

In the ideal situation, the PC component would be reduced to a simple laptop, rather than a desktop tower computer, a monitor, and a keyboard and mouse. In the case of the x-ray detectors under test, the limiting factor was the need for a PCI expansion slot, which is not compatible with any laptop. With another x-ray detector interface, a laptop may be a better option for the application.

2.8 Summary

In this chapter, an overall system design was conceived for the purposes of tuberculosis screening, based on a portable x-ray source, a flat-panel, digital x-ray detector, a computer, and a synchronization or control interface. Using the criteria of a rural tuberculosis screening program, a portable x-ray source (SR-115) was found. Two x-ray detectors were purchased; one was an industrial, indirect-detection x-ray detector (PerkinElmer XRD0820), and the other was a neo-natal, direct-detection x-ray detector (DRTech FLAATZ-330N). These x-ray detectors were integrated into working x-ray systems in the lab at the University of Waterloo (with the SR-115) and at the Robarts Research Institute, using the required custom hardware and software. The designs, schematics, and code were documented.

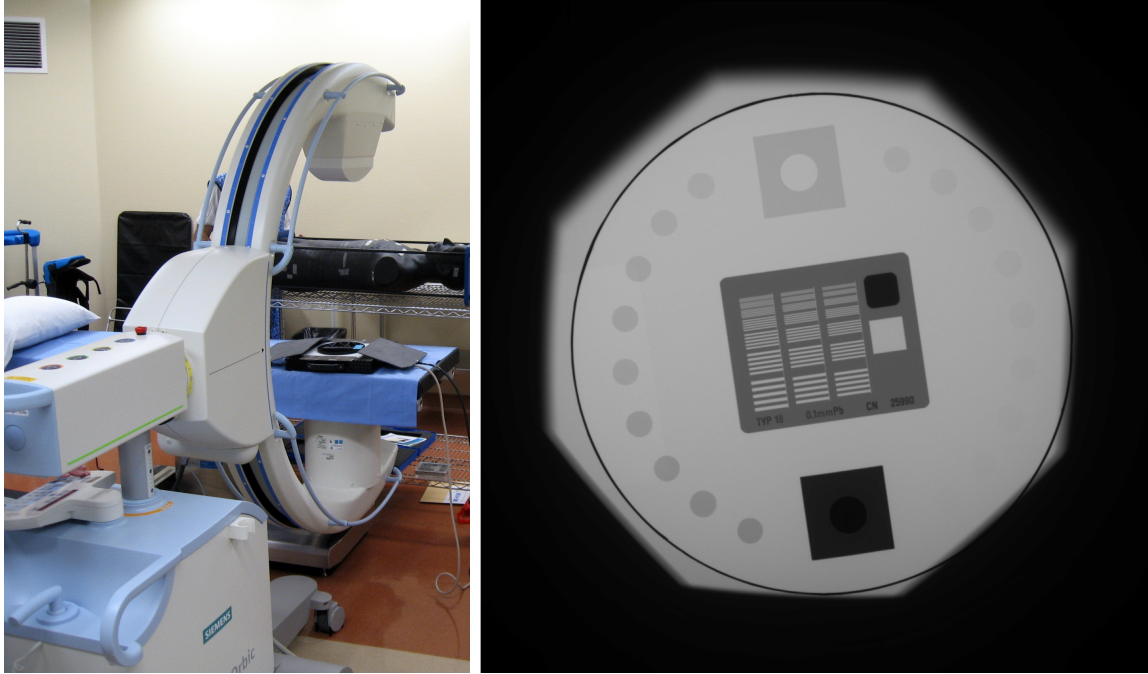
The next two chapters will present the characterization of the two x-ray detectors, starting with the PerkinElmer XRD0820 industrial, indirect-detection x-ray detector. Being able to compare the performance of these detectors to medical-grade chest radiography x-ray detectors will give an idea of their feasibility for the application of tuberculosis screening.

3 | Industrial x-ray detector characterization

This chapter explains the characterization of the PerkinElmer XRD0820 8" square industrial digital x-ray detector, based on the system integration described in Section 2.4. This characterization will enable the comparison between x-ray detectors currently used for chest radiography, and this industrial x-ray detector, which is less expensive than the full-size, medical-grade alternatives.

3.1 Phantom characterization

Initial x-ray device characterization of the PerkinElmer XRD0820 was done with a Leeds Quality assurance phantom and with a Siemens Arcadis C-arm x-ray source. The setup at the Grand River Hospital in Waterloo is shown in Figure 3.1a. The Leeds QA phantom is used to characterize spatial resolution and contrast. Setting the C-arm's source to 110kV and 5mA, with the x-ray detector integrating for 66ms, a visual inspection of the phantom in the image shows a spatial resolution of 2.5 cycles/mm, and a low-contrast sensitivity of 0.002. The octagon in the image (Figure 3.1b) is produced by the shaped field-of-view of the x-ray source.



(a) Siemens C-arm with XRD0820. (b) Image of Leeds QA phantom.

Figure 3.1: X-ray phantom setup at the Grand River Hospital.

3.2 Detective quantum efficiency

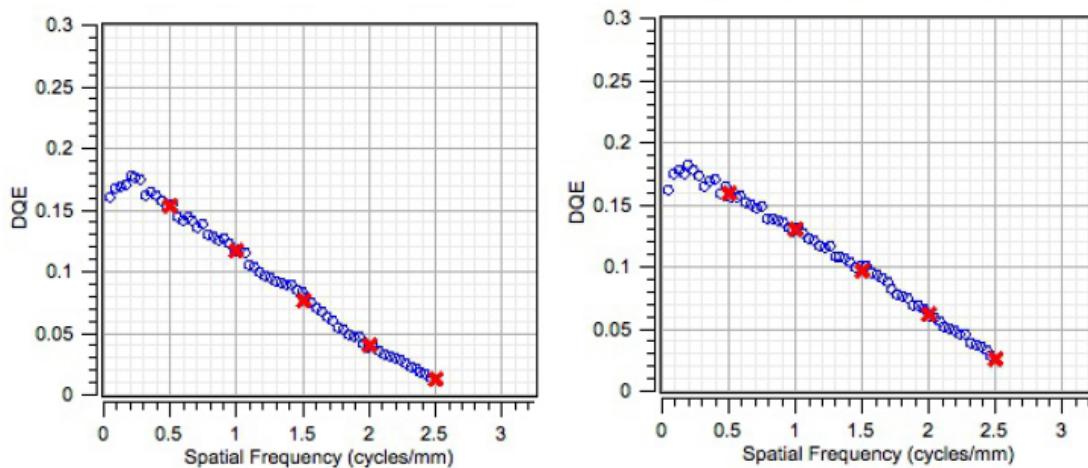
The detector was also characterized mathematically by its LSF and ESF, MTF, NPS and DQE at the Robarts Research Institute at Western University. X-ray pulses were generated using a validated IEC RQA-5 spectrum (70kV, 100mA, 100ms, 21mm added Al and a 7.1mm HVL). This generated an average exposure of 1.04mR, a reasonable detector exposure for a chest x-ray. The detector integrated the 1024x1024 pixel frame for 250ms, windowed around the x-ray pulse. The integrated DQE measurement tool *DQEPro* from DQE Instruments was used to characterize the device. *DQEPro* consists of hardware and software with several x-ray masks for edge images and noise images, and automated data collection. Figure 3.2 shows part of the measurement setup. Not pictured is the x-ray generator, to the right of the photo.



Figure 3.2: XRD0820 with the *DQEPro*.

The DQE is shown in Figure 3.3. If the curve is extrapolated toward the zero spa-

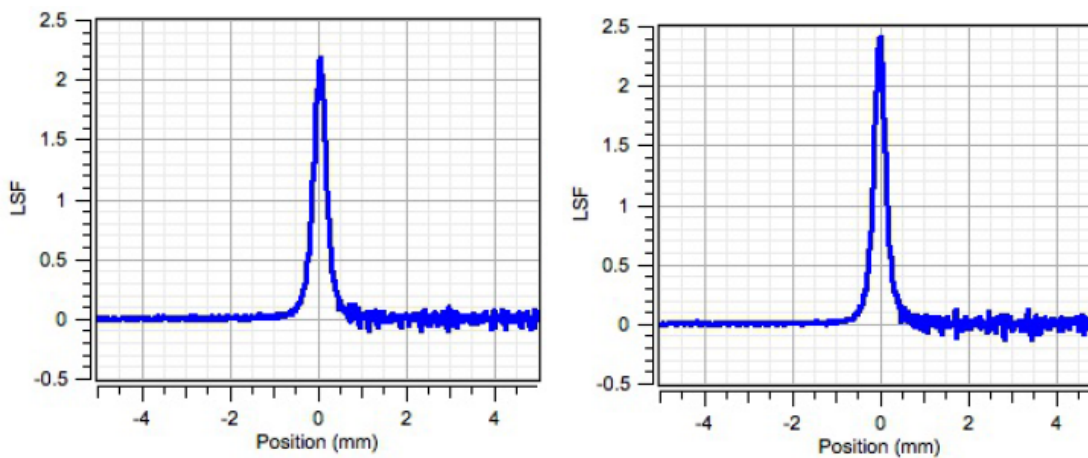
tial frequency, the DQE(0) is around 20%. Also shown are the LSF, MTF and NPS, in Figures 3.4, 3.5, and 3.6.



(a) DQE in the x direction.

(b) DQE in the y direction.

Figure 3.3: DQE for XRD0820.



(a) LSF in the x direction.

(b) LSF in the y direction.

Figure 3.4: LSF for XRD0820.

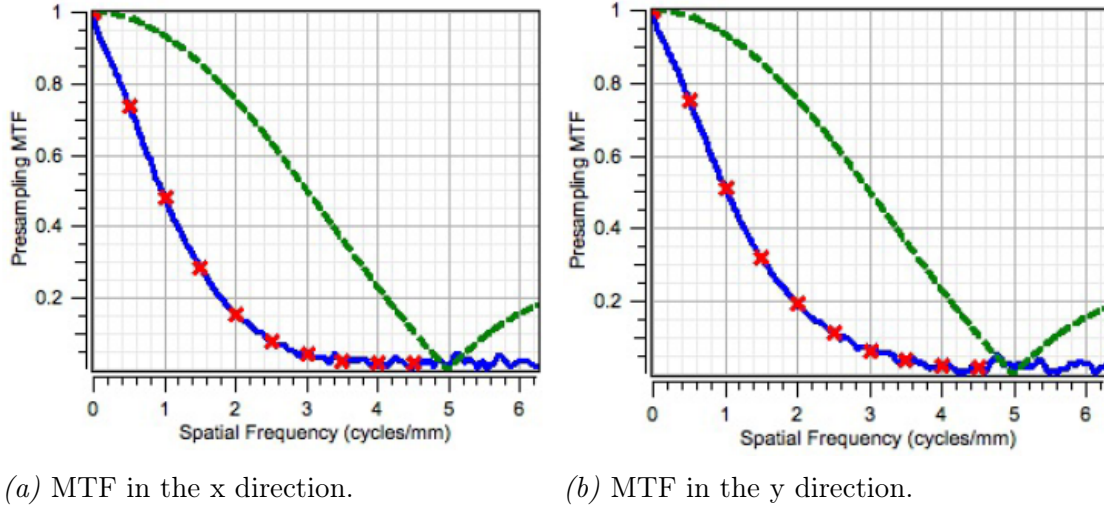


Figure 3.5: MTF for XRD0820. The green dashed line represents the ideal MTF.

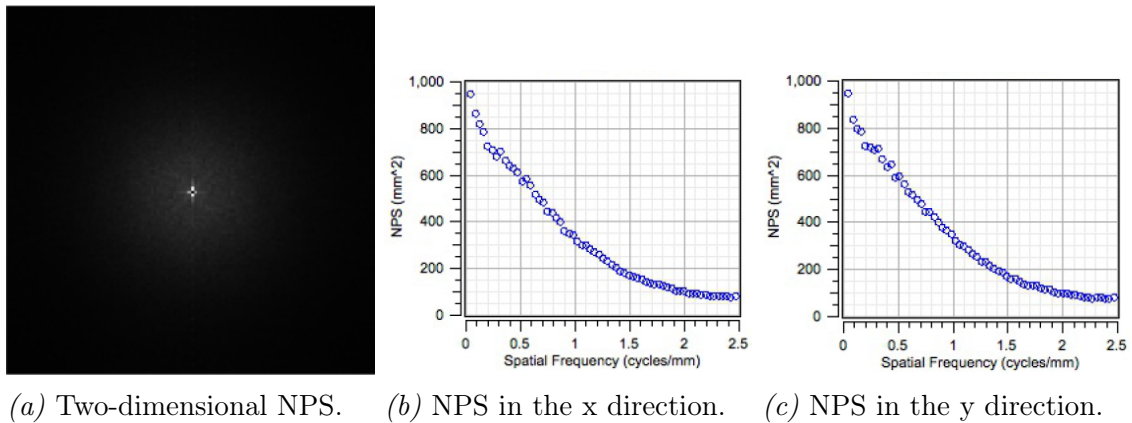


Figure 3.6: NPS for XRD0820.

To determine its relative performance to other detector systems used for chest x-ray imaging, the DQE of the XRD0820 was compared to the DQE numbers from other sources, like a similar comparison for mammography applications by Monnin and team [18]. Sandrik and Wagner characterized radiographic film-screen systems [19], while Dobbins and his group characterized computed radiography (CR) systems [20], and Bertolini and team characterized digital radiographic systems [21].

As examples, the XRD0820 is compared to a Kodak film screen, a Philips PCR ACe Type IIIN ST computed radiography panel with $200\mu\text{m}$ pixels, and a Carestreamhealth DRX-1 digital radiography a-Si TFT panel with $139\mu\text{m}$ pixel pitch, using a Gd₂O₂S:Tb scintillator. The XRD0820 TFT array has a pixel pitch of $200\mu\text{m}$ and uses the same scintillating material as the DRX-1. The DQE comparisons are shown in Figure 3.7.

While the high-frequency responses of all four systems are comparable (between 2% and 8% at 2.5cycles/mm), the low-frequency performance of the XRD0820 is most similar to the older imaging systems.

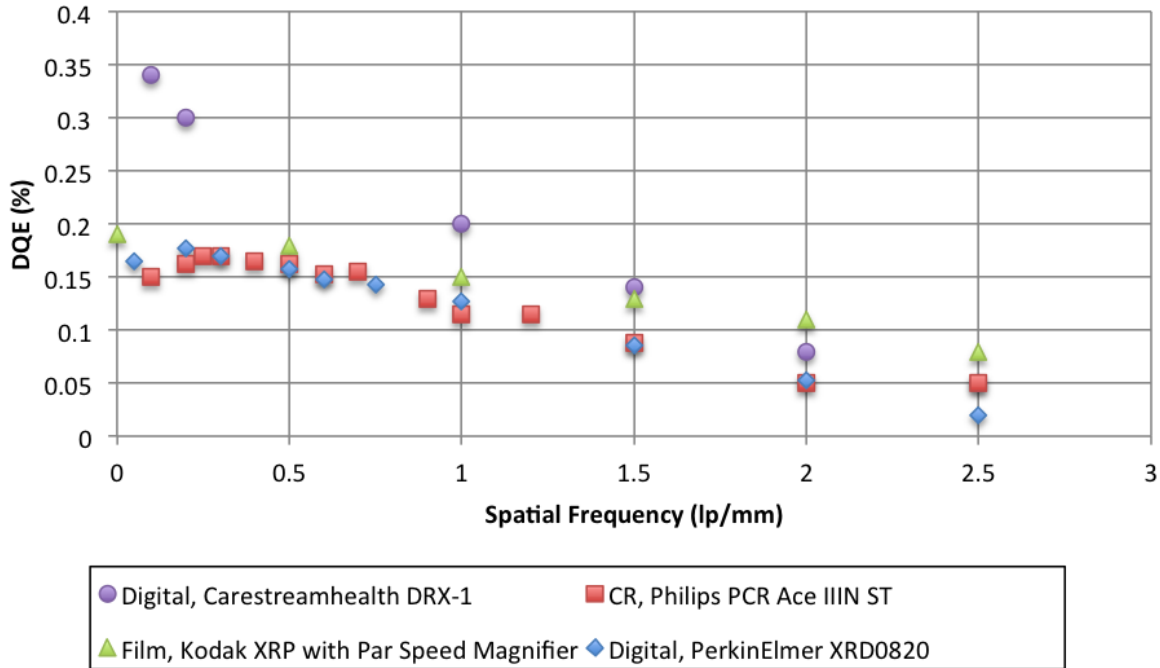


Figure 3.7: Comparison of the XRD0820 DQE(f) with computed radiography (CR), film and medical-grade digital x-ray systems.

3.3 Discussion

The XRD0820 was equipped with a DRZ-PLUS phosphor with a thickness of $208\mu\text{m}$ and a density of $100\text{mg}/\text{cm}^2$ [22], adhered to the active electronics with an optically opaque glue. Using a thinner phosphor material (the DRZ-STD alternative has a thickness of $140\mu\text{m}$ and a density of $68\text{mg}/\text{cm}^2$, with a quoted MTF at 1 lp/mm of 82%) would improve the MTF while decreasing the sensitivity, possibly improving the overall DQE compared to the DRZ-PLUS screen with a quoted MTF at 1 Lp/mm of 72%. However, this incremental improvement may not be enough: Using an x-ray detector with a phosphor material that is built directly onto the TFT panel using thin-film techniques would also increase its performance.

Furthermore, pixel array data could be gathered for the detector for the expected exposure mR and seconds so that software corrections can be made for the systematic differences in pixel gain and offset. Using a series of dark images, offset data can be calculated, and gain correction data can be calculated from series of dark images and uniformly exposed images.

Positively, the industrial nature of the XRD0820 means that it is rugged, with a high likelihood of surviving drops and environmental fluctuations.

With regards to the design components listed in Section 2.1, Table 3.1 shows pertinent information to the XRD0820.

Table 3.1: PerkinElmer XRD0820 design criteria ranking.

Detector cost	\$15000
Synchronization hardware cost	\$300
Weight	22kg
Ruggedness	High: industrial ruggedness
AC power	North American 110V
Integration	Difficult
Image performance	Comparable to older technologies

3.4 Summary

In this chapter, the characterization of the PerkinElmer XRD0820 industrial, indirect-detection x-ray detector was shown, using the metrics of MTF, NPS, and DQE. It was shown that this detector has similar performance to older x-ray imaging systems based on film-screen and computed radiography technologies. Although this x-ray detector is comparable, it will not compete with state-of-the-art in terms of performance.

The following chapter will discuss the characterization of another x-ray detector, the DRTech FLAATZ-330N neo-natal, direct-detection x-ray detector. This characterization will show its feasibility for the application of tuberculosis screening.

4 | Neo-natal x-ray detector characterization

This chapter explains the characterization of the DRTech FLAATZ-330N 8"x10" neo-natal digital x-ray detector, based on the system integration described in Section 2.5. This characterization will enable the comparison between x-ray detectors currently used for chest radiography, and this neo-natal x-ray detector, which is less expensive than the full-size alternatives.

4.1 Phantom characterization

Phantoms are used in medical physics for qualifying imaging systems or cancer radiation treatment systems. They are an expected part of any quality analysis of a medical imaging system.

4.1.1 Phantom design

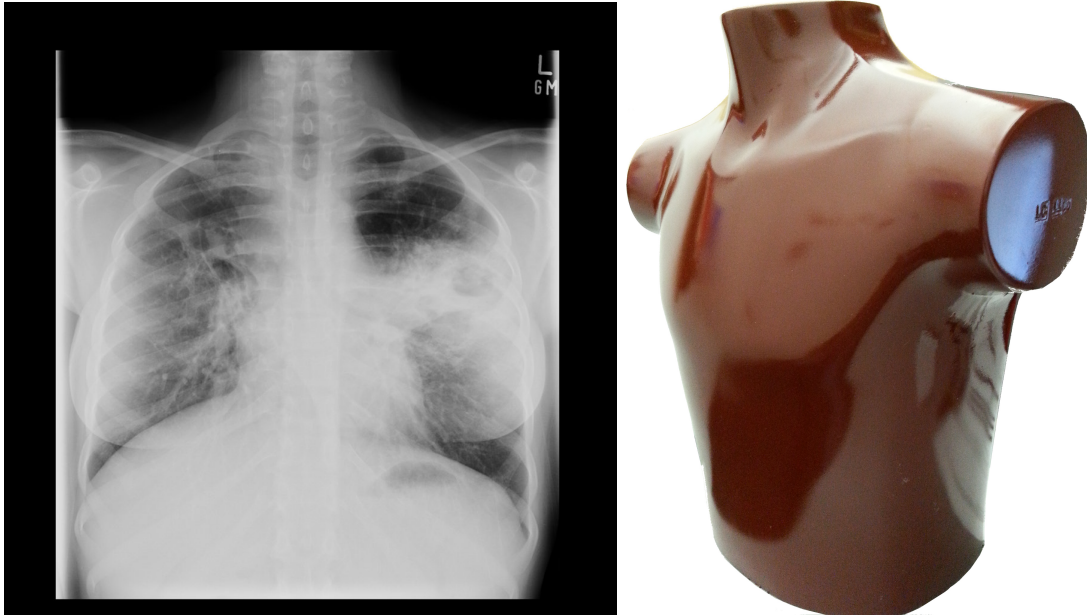
For this project, with a recommendation from Dr. Cari Borrás of the World Health Organization in Washington, DC, an anthropomorphic phantom was chosen from Radiology Support Devices. Other choices are listed in Table 4.1.

Table 4.1: Comparison of phantom choices.

Manufacturer	Description	Price
Harpell Associates	Opaque Thorax Phantom	\$8200
Imaging Solutions	Lung/Chest Phantom with removable diaphragm and coronary artery	\$17,326
Radiology Support Devices	Lung/Chest Phantom with removable diaphragm and coronary artery and added custom pathology	\$9162

The lung/chest phantom with custom tuberculosis pathology (for an extra \$260) was chosen over the Imaging Solutions phantom because of price, and over the Harpell Associates because it fit the requirements more closely and was recommended by the expert medical physicist, Dr. Borrás.

To design the custom phantom with tuberculosis, the manufacturer required an example x-ray. Five x-rays from the efficacy study were chosen that were always correctly diagnosed by all radiologists who saw them, regardless of the size of the image shown. Of these five, one image was particularly clear and of good quality. This image was used as the basis of the phantom design, shown in Figure 4.1a).



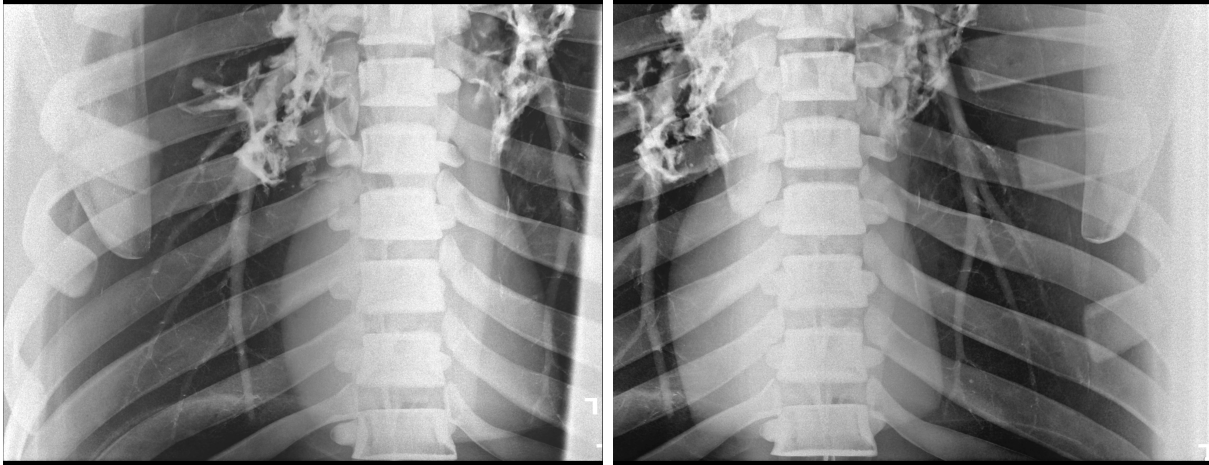
(a) The model x-ray image used for the lung phantom with added tuberculosis. (b) The anthropomorphic phantom used to qualify the x-ray system.

Figure 4.1: The custom anthropomorphic phantom was based on a lung x-ray of a tuberculosis case sent from the Aga Khan University Hospital (AKUH). The phantom came with two lung inserts: one with tuberculosis, and one without.

A standard lung insert was also ordered that swaps with the lung insert that has tuberculosis. Both fit into a solid chest cavity, which is shown in Figure 4.1b).

4.1.2 Images

The lung phantom was imaged in the lab with the FLAATZ-330N direct x-ray detector, shown in Figure 4.2 . Because the distance between the x-ray source and the detector is so low inside the lead-lined cabinet, the lung field does not completely fit into the image. In the future, an x-ray source at another institution may be used to capture the full region-of-interest. These images were taken with the phantom’s chest facing toward the source. In a standard chest x-ray, the patient normally faces away from the source, toward the detector. However, this is not feasible in the small x-ray cabinet used in the lab.



(a) Right lung.

(b) Right lung.

Figure 4.2: Phantom images, taken with the FLAATZ-330N.

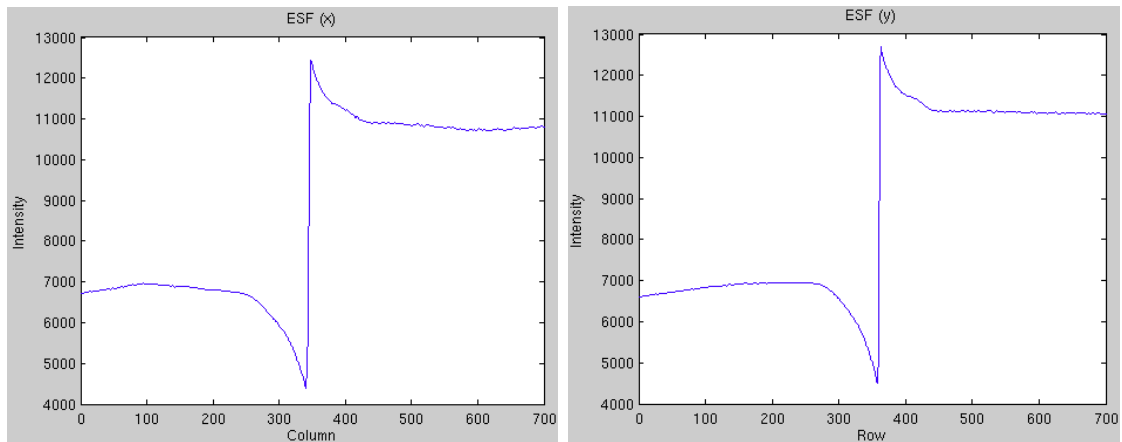
4.2 Modulation transfer function

The DRTech FLAATZ-330N direct detection x-ray detector was also characterized mathematically by its LSF, ESF, and MTF at the Robarts Research Institute at Western University, without the use of a DQEPro, unlike the procedure for the PerkinElmer XRD0820 indirect x-ray detector. X-ray pulses were generated using a validated IEC RQA-5 spectrum (70kV, 50mA, 100ms, and a 7.1mm HVL). This generated an average exposure of 0.69mR, a reasonable detector exposure for a chest x-ray. The detector integrated the 2008x1496 pixel charge for 250ms, windowed around the x-ray pulse. Figure 4.3 shows part of the measurement setup. Not pictured is the x-ray generator, inside the cabinet, and to the right of the photo. The post-processed ESF, LSF, and MTF are shown in Figures 4.4, 4.5, and 4.6, which were calculated in MATLAB® (documented in Appendix H) using the edge images captured at Robarts Research Institute. The curves are approximate, as the DRTech FConsole1 image acquisition software performs some edge enhancement post-processing (which is clearly demonstrated in the ESF curves), as well as dynamic contrast enhancement. Both of these features make it impossible to discern the detector's inherent performance accurately. Specifically, noise performance could not be calculated because of the dynamic contrast enhancement.

For alternate calculations of the ESF and MTF by Dr. Ian Cunningham, see Figure 4.7. In his calculations, there are some unexpected zero-crossings of the MTF that are not seen in the calculations using the code presented in this work. As well, the MTF appears to rise above 1 before dropping quickly down to 0. The zero crossings imply that a pixel averaging technique is being applied in the post-processing; therefore some frequencies are completely missing from the image.



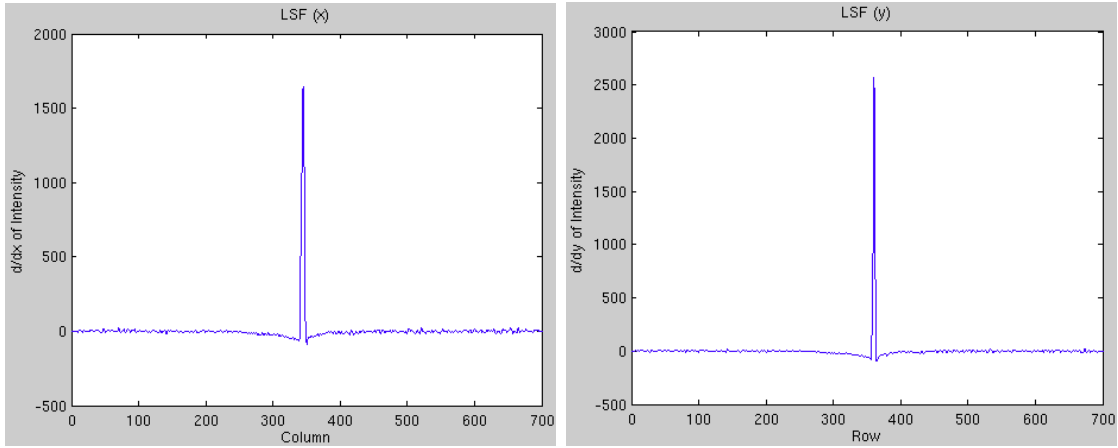
Figure 4.3: FLAATZ-330N set up for DQE measurements.



(a) ESF in the x direction.

(b) ESF in the y direction.

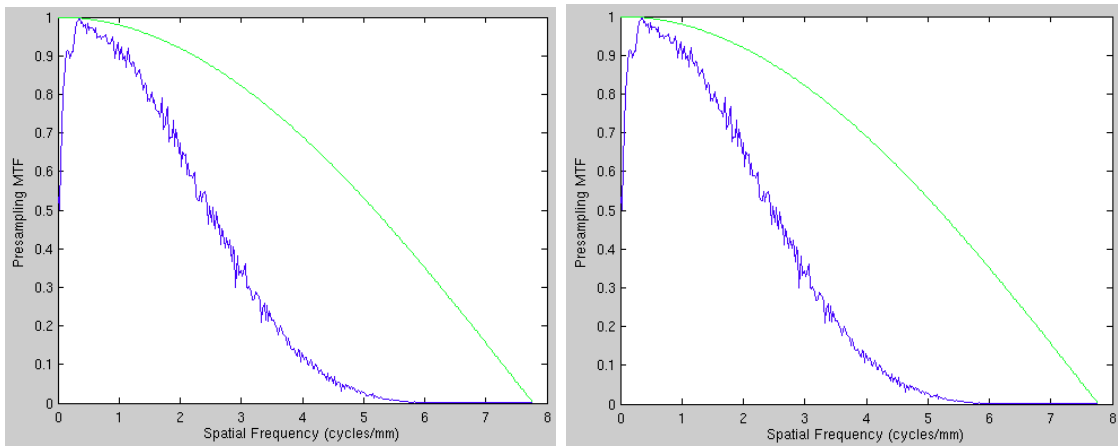
Figure 4.4: ESF for FLAATZ-330N.



(a) LSF in the x direction.

(b) LSF in the y direction.

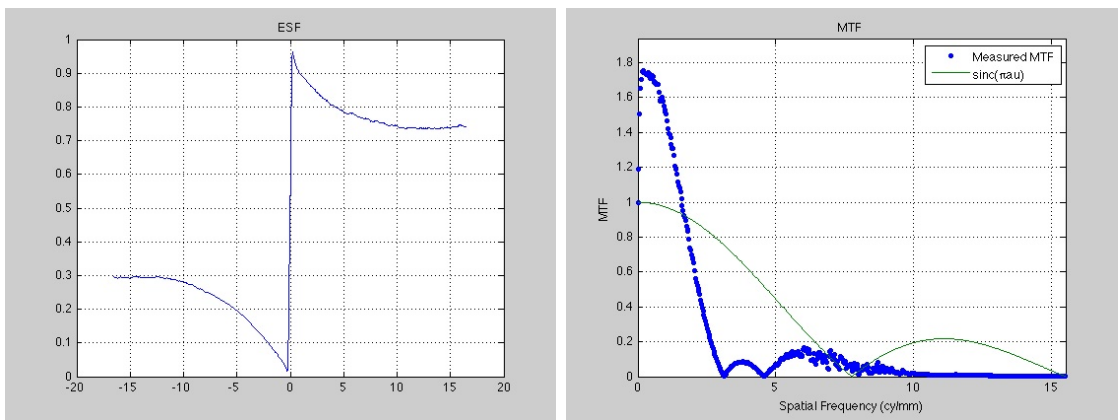
Figure 4.5: LSF for FLAATZ-330N.



(a) MTF in the x direction.

(b) MTF in the y direction.

Figure 4.6: MTF for FLAATZ-330N. The green dashed line represents the ideal MTF.



(a) ESF.

(b) MTF.

Figure 4.7: ESF and MTF for FLAATZ-330N, calculated by Dr. Ian Cunningham.

4.3 Discussion

Further measurements should be taken for anthropomorphic phantom tests, specifically to find whether the lung region of interest is small enough to be captured in a half-size x-ray detector. Initial phantom images —and expert advice —hint that the phantom would be sufficient for answering this question.

A major problem in the calculation of DQE for the DRTech FLAATZ-330N is the automatic post-processing done in the image acquisition software. Two algorithms are used that do not seem to be user-specifiable: edge enhancement (which shows up in the calculation of the ESF, and therefore the MTF), and dynamic contrast adjustment (which makes the NPS measurements wildly inaccurate).

Despite these major drawbacks, approximate MTF curves were calculated for the FLAATZ-330N. Remembering that the pixel pitch of the 330N is $129\mu\text{m}$, and that the pixel pitch of the 0820 is $200\mu\text{m}$, the theoretical limit of the MTF for the 330N is higher: about 7.75cycles/mm. The theoretical limit of the MTF for the XRD0820 is 5 cycles/mm.

Comparing the MTF measurements for the XRD0820 and the 330-N, keeping in mind that the actual pre-sampling MTF may be much worse than the MTF after software edge enhancement, both the low-frequency and high-frequency MTF of the 330-N are better than those of the 0820. At 1 cycle/mm, the MTF of the 330-N ($\sim 90\%$) is around twice that of the 0820 ($\sim 45\%$). At 3 cycles/mm, its MTF ($\sim 30\%$) is six times higher than that of the 0820 ($\sim 5\%$).

Without the NPS or accurate MTF measurements, the two detectors cannot be precisely compared. However, initial comparison shows great promise that the DRTech FLAATZ-330N has significantly better spatial response than the PerkinElmer XRD0820. Further investigation, with the removal of the software post-processing, would be needed to more accurately determine x-ray detector quality.

With regards to the design components listed in Section 2.1, Table 4.2 shows pertinent information to the FLAATZ-330N.

Table 4.2: DRTech FLAATZ-330N design criteria ranking.

Detector cost	\$15000
Synchronization hardware cost	\$50
Weight	2.7kg
Ruggedness	Low, with environmental constraints
AC power	European 220V
Integration	Easy
Image performance	High MTF*

*MTF could not be accurately measured due to unspecified edge enhancement algorithms.

4.4 Summary

In this chapter, the characterization of the DRTech FLAATZ-330N neo-natal, direct-detection x-ray detector was shown, using phantom images, and its estimated MTF. It was shown that this detector has much higher MTF values compared to the industrial x-ray detector, although the true MTF could not be determined, due to unspecified edge enhancement algorithms in the image acquisition software. Looking at images of the phantom, the detector appears to have high contrast and high resolution.

The preceding chapters described the system integration and characterization of two x-ray detectors for the purposes of tuberculosis screening. The following two chapters will investigate the effects on the diagnostic accuracy of having smaller x-rays or lower quality images compared to the standard, full-size, digital chest radiography x-ray detectors.

5 | Region-of-interest efficacy study

This chapter was originally submitted to the journal *Tuberculosis*, with some modifications.

5.1 Objective

Given that the proposed low-cost x-ray machine will only be able to capture an image of one lung at a time, this study aims to assess whether this restriction will have any impact on a radiologist’s ability to identify TB. Formally this study will assess if there is a statistically significant difference between the sensitivity or specificity of TB diagnosis using two images each containing one lung as compared to the traditional full chest x-ray containing both lungs. It is hypothesized that there will be no significant difference in either measure of diagnostic accuracy.

5.2 Methods

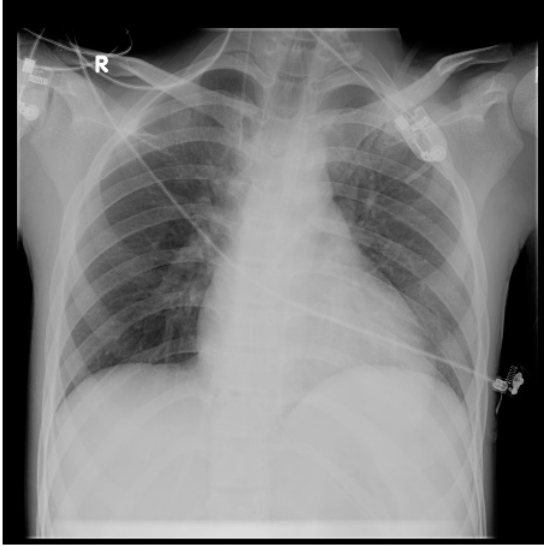
An experiment was designed wherein radiologists were asked to identify whether there were signs of TB in a collection of x-ray images from patients with and without TB. The images were given to radiologists in one of two formats: one format was the conventional full chest x-ray image; the other with two smaller, cropped images—one for each lung. The two-image format was designed to be consistent with what the low-cost x-ray machine would be able to capture in the field. The experiment was conducted using an online survey. In Figure 5.1 are two sample questions from the online survey—one for each format.

There were three phases of the study each with two versions. A completely new set of images were used for each phase. The two versions of the test were opposite in the sense that every image that was presented in the two-image format in version A was presented in the full image format in version B, and vice versa. The following tables (Tables 5.1, 5.2, and 5.3) describe the number of images used and number of measurement obtained during each of the three phases. Note that there were a total of 21 sessions logged and that in each of these 21 sessions all questions were completed.

**Investigation Into Chest X-ray Region of Interest
Tuberculosis Diagnosis**

Question 6: Determine if there are any signs of TB, or no signs at all.

- No sign of TB
- Sign(s) of TB

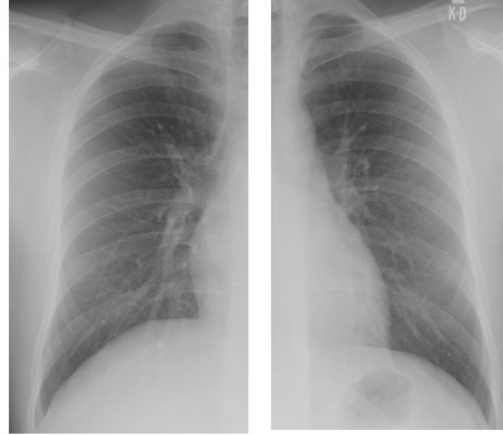


(a) Full image example.

**Investigation Into Chest X-ray Region of Interest
Tuberculosis Diagnosis**

Question 44: Determine if there are any signs of TB, or no signs at all.

- No sign of TB
- Sign(s) of TB



(b) Two-image example.

Figure 5.1: Examples of questions on web survey.

Table 5.1: The number of radiologists/raters in each survey are shown.

Survey Version	Phase 1		Phase 2		Phase 3		Overall
	A	B	A	B	A	B	A & B
Number of Raters	3	2	5	3	4	4	21

Table 5.2: The number of x-rays in each survey are shown.

Survey Version	Phase 1		Phase 2		Phase 3		Overall
	A	B	A	B	A	B	A & B
Complete TB	6	9	14	14	26	26	95
Two-image TB	9	6	14	14	26	26	
Complete non-TB	14	11	26	26	14	14	105
Two-image non-TB	11	14	26	26	14	14	
Total Unique Images	40	40	80	80	80	80	200

5.2.1 Statistical analysis

Taking verbatim from the publication [23]:

“To analyze the data, a generalized linear model with a logistic link function was used [24]. One model was fit for the data involving images of patients with TB which is related to sensitivity. A second, separate model was fitted for the

Table 5.3: The number of rater observations in each survey are shown.

Survey Version	Phase 1		Phase 2		Phase 3		Overall
	A	B	A	B	A	B	<i>A & B</i>
Complete TB	18	18	70	42	104	104	<i>356</i>
Two-image TB	27	12	70	42	104	104	<i>359</i>
Complete non-TB	42	22	130	78	56	56	<i>384</i>
Two-image non-TB	33	28	130	78	56	56	<i>381</i>
Total Observations	<i>120</i>	<i>80</i>	<i>400</i>	<i>240</i>	<i>320</i>	<i>320</i>	<i>1480</i>

data involving images of patients without TB; the second model is related to specificity. For each model the response variable was a sequence of 42 binomial observations, the first 21 representing the classification of cropped images for each rater/session and the second 21 representing the classification of full images for each rater/session. Both models included a covariate representing the contrast between cropped and full x-ray images: the coefficient of this covariate is of primary interest in the analysis. The models also included 20 binary covariates to block by rater/session: removing the effect of raters should increase the precision of estimating the contrast covariate coefficient. After fitting each model, a standard Wald test was done on the contrast covariate coefficient. This test looks for evidence that the coefficient is non-zero. In this context, a coefficient of zero indicates no difference between the accuracy on cropped and full x-ray images. A positive coefficient would indicate radiologists were more accurate on cropped images and a negative coefficient would indicate radiologists were more accurate on full images. In accordance with our hypothesis that cropping the images will have no impact on the ability of a radiologist to identify TB, we expect neither Wald test will find any evidence against the hypothesis that the contrast covariate coefficient is zero.”

5.2.2 Patients

The x-ray images used in the experiment were graciously provided by AKUH which is located in Karachi, Pakistan. The images provided by AKUH included 370 x-ray images from patients with confirmed tuberculosis cases, and 200 x-ray images of patients free from tuberculosis. The images provided were from previous patients at AKUH. This study was approved by the institutional review boards at the University of Waterloo and the AKUH. The need for obtaining signed consent of patients was waived for this retrospective analysis. All the x-ray images were purged of personal and health information, before being re-ordered randomly by a researcher who did not see any of the personal or health information. The images provided by AKUH were captured using either a digital x-ray machine or computed radiology. AKUH did not track which images came from which source. This could be a concern but it is not likely to matter since people cannot visually discern the image type at the given screen resolution.

5.2.3 Image cropping

The original digital x-ray images were stored as 1 megapixel TIFF-format images, and then converted to JPEG format for viewing on the web survey after cropped copies were made. The two image format was created by cropping two 5x9 sections from the image. Please see Figure 5.2, which shows what the cropped images include in terms of body parts.

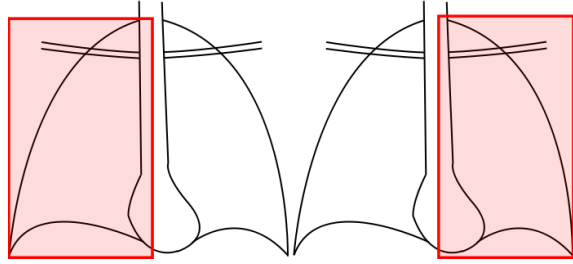


Figure 5.2: Diagram showing important body parts included in cropped images.

5.2.4 Image selection

Not all images provided by AKUH were used in the experiment: 200 of the 570 provided were used. Because the image cropping procedure was done to keep the body region shown the same in all cases this allowed for some variability in the pixel dimension. I noticed that the non-TB cases tended to have smaller pixel dimensions than the TB cases. As a result, images were randomly selected from a smaller set of images that had less difference in pixel dimensions as possible, within one standard deviation.

5.2.5 Radiologists

The radiologists who participated in the experiment did so on a volunteer basis and have the sincere thanks of the authors. The majority of participants were consultant radiologists from AKUH but there was one radiologist from Canada participating as well. No personal information was collected about the involved radiologists when they consented to participating by logging on to an online survey hosted on a secure server at the University of Waterloo. No information about the relative performance of a radiologist could be traced back to their identity. The statistical analysis implemented allowed for differences in skills or experience of radiologists. Twenty-one separate sessions were logged over the course of the study. Some of the radiologists were asked to return for the second or third phases and given different images to diagnose. The survey took an average of one half hour to complete per session.

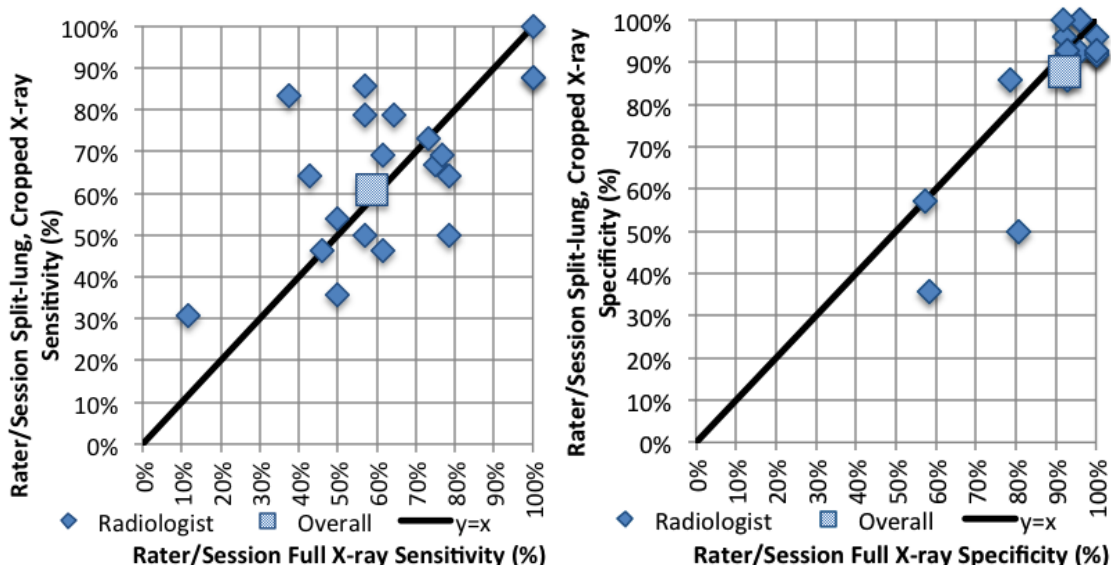
5.3 Results

The sensitivity and specificity to tuberculosis were separately measured for complete chest x-rays and cropped x-rays. Combining the results from the 21 sessions, the results are shown in Table 5.4. Alternatively, the data is shown on a rater/session basis represented as scatter plots in Figures 5.3a and 5.3b. In the two graphs the black line represents the equal accuracy line where a radiologist/session has the same accuracy when using the

Table 5.4: Overall sensitivity and specificity results for tuberculosis with full chest x-ray and two-image, cropped x-rays.

Full x-ray sensitivity	209/356 = 58.7%
Full x-ray specificity	354/384 = 92.2%
Two-image, cropped x-ray sensitivity	219/359 = 61.0%
Two-image, cropped x-ray specificity	335/381 = 87.9%

complete images and the cropped images. Based on our hypothesis we expect to see most points near the line, or at least that there are an equal number of points above and below the line. The authors believe that both plots are consistent with our hypothesis.



(a) Sensitivity for full vs. two-image. (b) Specificity for full vs. two-image.

Figure 5.3: For each radiologist/session, full chest x-ray sensitivity/specificity is compared with two-image, cropped x-ray sensitivity/specificity.

The two statistical models were fit and the analysis conducted as described in the methods section. The p-value for the Wald test of the contrast covariate coefficient in the sensitivity model was 0.576. This indicates there is no difference in the sensitivity of the radiologists when they use two cropped images relative to the full images. The p-value in the specificity model was 0.03695. This indicates there is some evidence of a difference in the specificity when the radiologists use the two smaller images. However as can be seen in Figure 4 this is entirely due to two radiologist sessions. Indeed this evidence is entirely dependent on these two points as the p-value becomes 0.41422 when the two data points are removed.

5.3.1 Outliers

Looking at Figure 5.3b, we see that most radiologists/sessions had very high individual specificities with both full and cropped images. However there are three outlying points with very poor specificities. Figure 5.4 makes clear how much worse the performance of these radiologists is. Notice that each of these three radiologist/sessions, represented by the 3 leftmost bars, made many errors on cases that no other radiologist made an error. This is very different from the remaining radiologists which rarely made an error unless at least one other radiologist made an error on the same image.

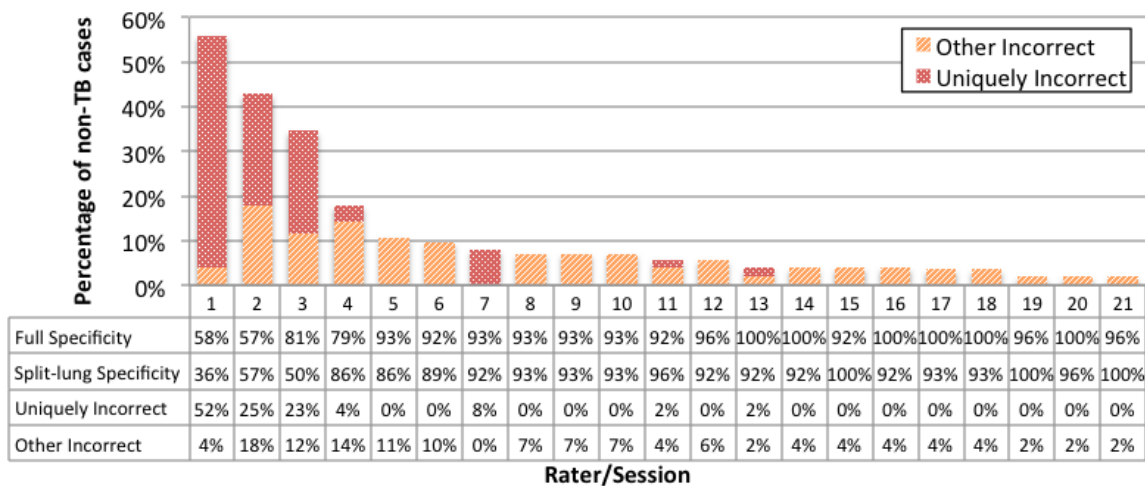


Figure 5.4: This plot shows the percentages of non-TB images seen by each rater/session that were diagnosed incorrectly. These are segmented into errors that are unique and non-unique. Also shown are the measures for each of the raters with both the complete and two image formats.

The authors feel these three points are very atypical and do not represent the ability of a typical radiologist. Ultimately the evidence against our hypothesis, on the specificity side, is these two outlying points below the line in Figure 5.3b. Given the atypical nature of these points the authors do not feel this warrants a rejection of our hypothesis and feel confident saying there is no reduction of the ability of a radiologist to diagnose TB when using the two cropped images versus the complete image.

5.3.2 Qualitative questionnaire

As part of the TB screening experiment, participants were asked some qualitative questions. Prior to the diagnosis questions the radiologists were asked “On a scale from 1 to 5, where 1 is ‘not difficult’ and 5 is ‘very difficult’, how difficult do you feel it would be to diagnose TB given two smaller x-ray images with the lungs separated?” Following the diagnosis questions “On a scale from 1 to 5, where 1 is ‘not difficult’ and 5 is ‘very difficult’, how difficult was it to diagnose TB given two smaller x-ray images with the lungs separated?” A summary of results is in Table 5.5, also showing the average change in perception of difficulty.

Table 5.5: Radiologists’ perception of difficulty of split-lung diagnosis before and after completing the survey.

	Pre-survey	Post-survey	Change from pre- to post-survey
Average Difficulty	2.923	1.462	-1.461
Standard Deviation	1.037	0.660	-0.377

85% of radiologists who were asked this question perceived the difficulty to be lower after having gone through the survey. The remaining 15% perceived the difficulty to be the same before and after. No correlation was found between radiologists’ perceived difficulty and their split-lung sensitivity or specificity.

5.4 Conclusions

The radiologists had comparable performance with the complete and two cropped images. There was no evidence of a difference in sensitivity when using complete versus cropped images. There was some evidence of a difference in specificity but that conclusion was dependent on two radiologists with very atypical performance. The authors feel confident that restrictions in the low-cost x-ray will not reduce a radiologist’s ability to identify signs of tuberculosis.

5.5 Summary

In this chapter, an efficacy study was described that shows that radiologists are equally accurate in their tuberculosis diagnosis when shown two single-lung x-rays as when shown a standard, full chest x-ray. This shows that lowering the cost of a digital x-ray system by decreasing the detector area will not affect the diagnostic accuracy of tuberculosis screening.

In order to make this study more suited to the particular x-ray detectors under test in this project, the following chapter examines the possibility of simulating x-rays as they would be captured by the x-ray detectors under test, without a clinical trial. If clinical x-rays can be modified to mimic the image performance of the XRD0820 and the FLAATZ-330N, some conclusions may be made about their feasibility for tuberculosis screening without clinical trials.

6 | DQE simulations

After the efficacy study, another way to determine the theoretical efficacy of the x-ray detectors for tuberculosis screening was as follows: First, we know that all detector systems (film, CR and DR) can be characterized by a DQE curve. Detector systems may be easily compared to each other using this method. Knowing the DQE of the digital x-ray detector used to take the images in the efficacy study, and knowing the DQE of the XRD0820 and the FLAATZ-330, these systems may be compared objectively. It was proposed that image processing techniques (adding blur and noise) could be applied to the images from AKUH to simulate the image quality of the lower-cost detectors under test, before requiring a clinical trial.

To that end, some MATLAB® code was written, first, to be able to calculate the DQE of a detector, and second, to determine the blur or noise to add to the high-quality chest x-rays in order to simulate the lower performance detectors' "theoretical chest x-ray." This code is documented in Appendix H.

To calculate the DQE of a detector, given several dark images and two edge images (to calculate MTF in both x- and y-axes), the following steps must be taken:

1. Calculate the edge spread function in x- and y-directions using the edge images.
 - (a) Determine the edge angle by rotating the image until the edge appears vertically oriented. Record this angle.
 - (b) Sum along the columns and take the average based on the number of rows. This gives the average intensity of x-rays in each column.
2. Calculate the line spread function in x- and y-directions using the edge images. Using backward (for first two pixels), central, and forward (for last two pixels) differencing, calculate the numerical differentiation of the edge spread function along this row. The resulting curve should be as in Figure 3.4.
3. Determine the modulation transfer function [25].
 - (a) Take the absolute values of the fast Fourier transform of the line spread function.
 - (b) If necessary, apply a smoothing function to the curve. The resulting curve should appear as in Figure 3.5.
4. Determine the noise power spectrum from the (several) noise images.

- (a) Calculate the average pixel value in all pixels across all the noise images. Then, subtract this “dc” (zero spatial frequency) value from each pixel in all the noise images. This will result in some pixels having negative values.
 - (b) Calculate the modulus of the 2D fast Fourier transform of each of these images, then square this value (similar to electrical signal noise calculations).
 - (c) Cycling through all pixels of the 2D FFTs (representing the intensities at those spatial frequencies), calculate the average intensity at each spatial frequency across all the 2D FFTs. The result will now be only one 2D FFT that is the average of all the 2D FFTs.
 - (d) Take the square of the modulus of this image.
 - (e) Apply noise detrending techniques [26] (This step was not implemented in this project). The result should be as in Figure 3.6.
5. Calculate the DQE simply by dividing the MTF by the NPS, element-wise (assuming the dimensions of the two arrays are compatible).

The code documented lists three separate functions, `CalculateImageMTF`, `CalculateImageNPS`, and `CalculateImageDQE`:

- `function [ESF, LSF, MTF]=CalculateImageMTF(edge_image, smoothness)`
The argument `edge_image` is the edge image captured by the x-ray detector. `smoothness` is an integer used to add optional windowed averaging to the curve after it is calculated. `ESF`, `LSF`, and `MTF` are one-dimensional arrays holding the values of these curves calculated from the edge image.
- `function NPS=CalculateImageNPS(image_set, smoothness)`
The argument `image_set` is the collection of dark images for the noise calculations. The integer `smoothness` applies optional averaging to the NPS measurement. `NPS` is the two-dimensional Wiener noise spectrum.
- `function [ESF, LSF, DQE, MTF, NPS, NPS_2D]=CalculateImageDQE(edge_image, open_images, MTF_smoothness, NPS_smoothness)`
This function calls the previous two functions in its calculation of detector metrics. Thus, the arguments may be passed on unchanged to `CalculateImageMTF` and `CalculateImageNPS`. `NPS_2D` is simply one row of the two-dimensional NPS matrix.

After developing this procedure, it was speculated that some blur and noise addition to a “perfect” edge image would result in a specific DQE curve, and that this blur and noise could be added to the image from AKUH to simulate the relative detector performance of the XRD0820 or the FLAATZ-330N. After implementing the simulations, it was realized that a DQE curve is not uniquely associated with a specific blur. In fact, an infinite number of combinations of certain amounts of blur and noise may result in the same DQE curve. As explained by Dr. Ian Cunningham from the Robarts Research Institute, the DQE curve does not present enough information to be traced back to a single “amount” of blur or

noise. One must know all about the pixel pitch, the thicknesses of the photodetectors and scintillators, the materials involved in each, and other physical traits. In his expert experience, such a simulation would be worthy of an entire PhD, if it turned out to be possible.

There are many publications on simulating lower dose or added noise for CT applications ([27], [28], [29]), but nothing published on simulating different pixel pitches or architectures, simply because of the physical limitations and unknowns. Thus, the MATLAB® development was halted after this realization. However, other academics may be interested to pursue a solution to this problem.

6.1 Summary

In this chapter, code was documented to try to simulate the chest x-rays that would be taken by the x-ray detectors under test, by using their relative detector performance. It was determined that much more would need to be known about the physics of the system to be able to simulate this. Despite this, the MATLAB® code was useful to calculate the MTF, NPS and DQE of x-ray detectors, given slanted edge images and a series of dark images.

7 | Conclusions and recommendations

7.1 Contributions

The following is a list of the achievements in this work:

- SourceRay SR-115 x-ray source
 - Design of door interlock for lead-lined x-ray cabinet.
 - Met the safety certifications for the Electrical Safety Authority and the Ontario Ministry of Labour.
- PerkinElmer XRD0820 industrial x-ray detector
 - System integration with Robarts Research Institute x-ray source, which included the design of synchronization circuitry (PCB) and VHDL software for the Altera DE2 FPGA.
 - Detector performance characterization.
- DRTech FLAATZ-330N neo-natal x-ray detector
 - System integration with SR-115 x-ray source.
 - System integration with Robarts Research Institute x-ray source, which included the design of custom circuitry (PCB).
 - Detector performance characterization.
- Tuberculosis efficacy study for split-lung, two-image chest x-rays
- MATLAB® code to calculate the DQE of a digital x-ray detector, and work to simulate the relative image quality on a chest x-ray from a lower-quality detector

7.2 Conclusions

With reference to the purposes of this project (Section 2.1), the following sections detail the conclusions after the completion of this project.

7.2.1 X-ray generator

The x-ray generator chosen for this project was a SourceRay SR-115, a portable, stationary anode, 1kW, 15mA x-ray source. With a stand, it was the lowest-cost option of those found that were certified for use in North America, and is compatible with both 115V and 230V AC power systems (making it useable in Canada and overseas). This source, though not very powerful, is powerful enough for low-throughput chest x-ray, and was useful for in-lab tests. In Canada, it was only certified to be used inside an x-ray room/cabinet, which made it no longer portable. However, it is very similar to what is used in the field. One challenge that had to be overcome was that the generator is triggered by a hand switch that uses modular connectors and a 4-connector phone cable. This made integration more difficult.

7.2.2 X-ray detector

The indirect x-ray detector chosen was a PerkinElmer industrial-grade, 8"x8" XRD0820 detector. Its cost was determined to be applicable to low- and middle-income countries. Though its size may be too small for the application, and its spatial resolution would be too low for fractures and breaks, its resolution is good enough for finding tuberculosis. Its performance was characterized by Dr. Ian Cunningham at Robarts Research Institute in London, Ontario, using a custom-built synchronization circuit board and FPGA software.

Two challenges were overcome: First, system integration was difficult because of the interface being poorly explained in the technical manuals. This was overcome through collaboration with the engineers at PerkinElmer, and through some reverse engineering techniques. Secondly, the PerkinElmer image acquisition industrial software provided was not very user friendly, including advanced functions that were not translated from German to English.

The MTF was measured, with 48% at 1 cycle/mm, and 5% at 3 cycles/mm. The DQE(0) was about 20%. Compared to medical-grade x-ray detectors on the market, this industrial-grade x-ray detector performed about as well as conventional film-screen or computed radiography systems.

The direct x-ray detector chosen was a DRTech, neo-natal, 8"x10" FLAATZ-330N detector. Its cost was about the same as the XRD0820, but its performance was much higher. Unfortunately, the image acquisition software performed dynamic post-processing, making it impossible to characterize the detector hardware performance accurately. It was characterized by Dr. Ian Cunningham at Robarts Research Institute in London, Ontario, using a custom-built synchronization circuit board.

As with the XRD0820, the FLAATZ system integration was made more difficult with non-standard x-ray generators by several unknowns that were not explained in the technical manual: For instance, it was not known whether the hand switch was driving or pulling current. In the end, it became apparent that the switches were not active, and needed to have power provided to trigger x-ray exposure.

Because of two unspecified post-processing algorithms applied (edge enhancement and dynamic contrast enhancement) by the DRTech image acquisition software, the DQE could not be determined. Approximate, post-processed MTF curves show that the MTF may be significantly higher than that of the XRD0820, in both low frequencies (90% at 1 cycle/mm) and high frequencies (30% at 3 cycles/mm). Further investigation must be done to find more accurate estimations of the pre-sampling MTF.

One thing that makes the selenium-based FLAATZ inapplicable to many low-income countries is that it must be stored between 0 and 40 degrees Celsius, and operated between 5 and 35 degrees Celsius, besides other environmental requirements that would be difficult to ensure in many countries. Conversely, the XRD0820 is a ruggedized, industrial detector that is built for the elements, and will likely survive being dropped.

With regards to the design components listed in Section 2.1, Table 7.1 compares the pertinent information for both detectors.

Table 7.1: X-ray detector design criteria ranking.

Criterion	XRD0820	FLAATZ-330N
Detector cost	\$15000	\$15000
Synchronization hardware cost	\$300	\$50
Weight	22kg	2.7kg
Ruggedness	High	Low
AC power	NA 110V	EU 220V
Integration	Difficult	Easy
Image performance	Comparable to older tech.	High MTF*

*MTF could not be accurately measured due to unspecified edge enhancement algorithms.

7.2.3 Tuberculosis efficacy study

The efficacy of smaller single-lung chest x-rays for tuberculosis was determined using an online survey of radiologists. Results showed that radiologists are equally as good at correctly diagnosing tuberculosis when shown two single-lung x-rays as they are when shown a full chest x-ray. Besides two outlying data points, radiologists were also equally good at correctly diagnosing a TB-free patient when shown two single-lung x-rays as they were when shown a full chest x-ray. These results show that a smaller x-ray detector would be useful to diagnose pulmonary tuberculosis.

7.2.4 DQE simulations

As aforementioned, it was found that DQE is not unique to a specific “amount” of blur or noise. Therefore, knowing the DQE of an x-ray detector is not enough to simulate the relative decrease in image quality of a chest x-ray from another x-ray detector with

a different pixel pitch and architecture. Other papers have been published in simulating reduced x-ray dose for one x-ray detector, but not to simulate changes between different x-ray detectors. However, code was successfully written to calculate DQE for an x-ray detector.

7.3 Recommendations

From the analysis and conclusions presented above, a few recommendations can be made.

7.3.1 X-ray generator

System integration difficulty was mainly due to the unknowns about the trigger interface. Care must be taken about whether the pins are driving current, pulling current, or expected to be open circuits.

7.3.2 X-ray detector

Recommendations about the x-ray detector for this application come in two groups: system integration, and cost.

In the future, system integration should be implemented in a more flexible method. Using software to program system timings worked well, and made the XRD0820 system more easy to customize. The FLAATZ detector came with software controls for x-ray integration time, but the XRD0820 required specific frame reset signals to determine for how long the frame would integrate. A finished product for the XRD0820 should involve programming a microcontroller or an FPGA (without an education board!) and be ready to be customized in software. Ideally, one interface system would work for both detectors and both types of sources used in this project.

To reduce costs further for this application, the x-ray detectors should be designed with this application in mind. Using lateral metal-semiconductor-metal photodetectors instead of PIN photodetectors would lower manufacturing costs because they do not need a p+ doped layer in the manufacturing process.

7.3.3 Tuberculosis efficacy study

To make a future similar medical study more powerful, the identities of the radiologist participants should be recorded so that their performance in the medical study can be associated with the number of years of experience in the profession.

Although the information letter to participants declared that the study would take 1 hour to complete, most participants completed the entire survey within 20 minutes. This fact can be used in the future to increase the sample size of images in each survey.

7.3.4 DQE simulations

Although there was not sufficient time to properly do DQE simulations, as described, there remains a potentially solvable problem: to simulate the detective quantum efficiency of any arbitrary x-ray system using the cascade model, and thereby simulate the relative image quality of a chest x-ray image if the physical properties of the original x-ray detector are known, and the physical properties of the target x-ray detector are known. Potentially a “reverse” Monte Carlo simulation could be implemented to determine a statistical distribution of potential paths of the electrons, visible photons, and incident x-ray photons before they have been sampled by the original detector pixel array. Using well-defined phantoms in the lab, these simulations could potentially be characterized. Then, the mean or “most likely” origination point of each x-ray photon would be used as the starting point of the Monte Carlo simulation of the cascaded system representing the detector under test. This recommendation assumes that a near-perfect detector exists to determine the phantom dimensions with high precision.

References

- [1] World Health Organization. (2011, May). *Asthma* [Online]. Available: <http://www.who.int/mediacentre/factsheets/fs307/en/index.html>
- [2] World Health Organization. (2012, November). *Chronic Obstructive Pulmonary Disease (COPD)* [Online]. Available: <http://www.who.int/mediacentre/factsheets/fs315/en/index.html>
- [3] World Health Organization. (2013, April). *Pneumonia* [Online]. Available: <http://www.who.int/mediacentre/factsheets/fs331/en/>
- [4] World Health Organization, *Global Tuberculosis Report 2012*, World Health Organization: France, 2012.
- [5] National Tuberculosis Control Program (12 July, 2013). *About Us* [Online]. Available: <http://www.ntp.gov.pk/cmsPage.php?pageID=7>
- [6] M. D. Rossman and R. L. Mayock, (D. Schlossberg, editor), “Pulmonary Tuberculosis” in *Tuberculosis and Nontuberculous Mycobacterial Infections*, W.B. Saunders Company, Toronto, 1999
- [7] Anne McB. Curtis, (L. N. Friedman, editor), “Radiology of Mycobacterial Disease” in *Tuberculosis: current concepts and treatment*, CRC Press, Boca Raton, 1994.
- [8] Cuevas, et al, “LED Fluorescence Microscopy for the Diagnosis of Pulmonary Tuberculosis: A Multi-Country Cross-Sectional Evaluation” *PLoS Med.*, vol. 8, no. 7, 2011.
- [9] FINDDDiagnostics. *LED fluorescence and Xpert MTB/RIF* [Online]. Available: <http://www.finddiagnostics.org/programs/tb/>
- [10] V.I. Mikla, V.I. Rusin, P.A. Boldizhar, “Advances in imaging from the first X-Ray images,” *J. of Optoelect. And Adv. Mat.*, vol. 14, no. 7-8, pp. 559-570, Jul-Aug 2012.
- [11] AIP (2012, December). *Marie Curie and the Science of Radioactivity: War Duty (1914-1919)* [Online]. Available: <http://www.aip.org/history/curie/war1.htm>
- [12] I. A. Cunningham, B. K. Reid, “Signal and noise in modulation transfer function determinations using the slit, wire, and edge techniques”, *Med. Phys.*, vol. 19, no. 4, pp. 1037-1044, Jul 1992.

- [13] I. A. Cunningham, Westmore, and Fenster, "A Spatial-Frequency Dependent Quantum Accounting Diagram and Detective Quantum Efficiency Model of Signal and Noise-Propagation in Cascaded Imaging Systems", *Med. Phys.*, vol. 21, no. 3, pp. 417-427, Mar 1994.
- [14] Ikushi Onozaki, "TB Disease Prevalence Survey", Geneva WHO, 2011. Available: <http://www.who.int/tb/IkushiOnozakiLessonsfromTBprevalencesurvey.pdf>
- [15] G.G. Poludniowski and P.M. Evans, "Calculation of x-ray spectra emerging from an x-ray tube. Part I. electron penetration characteristics in x-ray targets.", *Med. Phys.*, vol. 34, no. 6, pp. 2164-74, Jun 2007.
- [16] G.G. Poludniowski, "Calculation of x-ray spectra emerging from an x-ray tube. Part II. X-ray production and filtration in x-ray targets.", *Med. Phys.*, vol. 34, no. 6, pp. 2175-86, Jun 2007.
- [17] G. Poludniowski, G. Landry, F. DeBlois, P.M. Evans, and F. Verhaegen, "SpekCalc: a program to calculate photon spectra from tungsten anode x-ray tubes.", *Phys. Med. Biol.*, vol. 54, no. 19, pp. 433-8, Oct 2009.
- [18] P. Monnin, D. Gutierrez, S. Bulling, D. Lepori, J.F. Valley, and F. R. Verdun, "A comparison of the performance of modern screen-film and digital mammography systems," *Phys. Med. Biol.*, vol. 50, no. 11, pp. 2617-31, 2005.
- [19] J. M. Sandrik and R. F. Wagner, "Absolute measures of physical image quality: Measurement and application to radiographic magnification," *Med. Phys.*, vol. 9, no. 4, pp. 540-9, 1982.
- [20] J. T. Dobbins III, D. L. Ergun, L. Rutz, D. A. Hinshaw, H. Blume, and D. C. Clark, "DQE(f) for four generations of computed radiography acquisition devices," *Med. Phys.*, vol. 22, no. 1, pp. 1581-93, 1995.
- [21] M. Bertolini, A. Nitrosi, S. Rivetti, N. Lanconelli, P. Pattacini, V. Ginocchi, and M. Iori, "A comparison of digital radiography systems in terms of effective detective quantum efficiency," *Med. Phys.*, vol. 39, no. 5, pp. 2617-27, 2012.
- [22] Mitsubishi Chemical. (2012, May). *Fluorescent Screens* [Online]. Available: http://www.mcc-phosphor.com/english/products/x-ray/fluorescent/drz_pi.html.
- [23] Ryan Mann, Daniel Severn, Waseem Mirza, Karim S Karim, "Tuberculosis screening with a single-lung sized digital x-ray detector", *Tuberculosis*, Submitted October 2013
- [24] P McCullagh, J.A. Nelder. *Generalized Linear Models (2nd ed.)*. Chapman & Hall 1989.
- [25] E. Samei and M. J. Flynn, "A method for measuring the presampled MTF of digital radiographic systems using an edge test device", *Med. Phys.*, vol. 25, no. 1, pp. 102-13, Jan 1998.

- [26] Z. Zhou, F. Gao, H. Zhao, and L. Zhang, “Techniques to improve the accuracy of noise power spectrum measurements in digital x-ray imaging based on background trends removal”, *Med. Phys.*, vol. 38, no. 3, pp. 1600-10, Mar 2011.
- [27] A. J. Britten, M. Crotty, H. Kiremidjian, A. Grundy, and E. J. Adam, “The addition of computer simulated noise to investigate radiation dose and image quality in images with spatial correlation of statistical noise: an example application to X-ray CT of the brain”, *The Brit. J. of Rad.*, vol. 77, pp. 323-328, 2004.
- [28] K. W. Hulme, J. Rong, B. Chasen, H. H. Chuang, D. D. Cody, F. C. Wong, and S. C. Kappadath, “A CT Acquisition Technique to Generate Images at Various Dose Levels for Prospective Dose Reduction Studies”, *Amer. J. of Rad.*, vol. 196, pp. 144-151, Feb 2011.
- [29] B. Juste, J.I. Villaescusa, R. Tortosa. and. G. Verdú, “Study of Pediatric CR Dose Reduction Using Noise Addition Simulation Tools,” in *11th International Congress of the IUPESM*, Munich, Germany, vol. 25, no. 2, pp. 879-882, Sept 2009.
- [30] A. G. Michette, C. J. Buckley, “X-ray science and technology,” Bristol: Institute of Physics Publishing, 1993, p. 240-248.
- [31] Karim S. Karim, “ECE 730 T21 Spring 2012 lecture notes”, University of Waterloo, May 2012.
- [32] E. Storm and H. Israel, “Photon cross-sections from 0.001 to 100 MeV for elements 1 through 100.” Report LA-3753, Los Alamos, California, 1967.
- [33] P.F. Liaparinos, I.S. Kandarakis, D.A. Cavouras, D.N. Nikolopoulos, I.G. Valais, G.S. Panayiotakis. “Simulating the emission efficiency and resolution properties of fluorescent screens by Monte Carlo methods”. *Nuclear Science Symposium/Medical Imaging Conference*, 2004, pp. 874-878.
- [34] *ESTAR - Stopping-power and range tables for electrons* [Online]. Available: <http://physics.nist.gov/PhysRefData/Star/Text/ESTAR.html>

APPENDICES

A | Synchronization FPGA code

This is the VHDL code used to program the Altera Cyclone FPGA for the synchronization of the XRD0820 x-ray detector and the x-ray source at Robarts Research Institute.

```
LIBRARY ieee;
USE ieee.std_logic_1164.ALL;
USE ieee.numeric_std.ALL;

-- ENTITY SevenSegment
-- Displays a character/number on a hex display, based on the input
-- In this case, it displays 0-9 and a dash if the input is N/A

ENTITY SevenSegment IS PORT(
dataIn : IN INTEGER;
segmentsOut : OUT STD_LOGIC_VECTOR(6 DOWNTO 0) );
END SevenSegment;

ARCHITECTURE Behavioral OF SevenSegment IS
BEGIN
--These pins are turned on with an low.
WITH dataIn SELECT segmentsOut(6 DOWNTO 0) <=
"1000000" WHEN 0,
"1111001" WHEN 1,
"0100100" WHEN 2,
"0110000" WHEN 3,
"0011001" WHEN 4,
"0010010" WHEN 5,
"0000010" WHEN 6,
"1111000" WHEN 7,
"0000000" WHEN 8,
"0010000" WHEN 9,
"0111111" WHEN others; -- dash
END Behavioral;

LIBRARY ieee;
USE ieee.std_logic_1164.ALL;
USE ieee.numeric_std.ALL;

-- ENTITY NumberDisplay
-- updates the hex displays with the chosen integration time

ENTITY NumberDisplay IS PORT(
Milliseconds: IN INTEGER;
clock: IN STD_LOGIC;
hex4,hex3,hex2,hex1,hex0 : OUT STD_LOGIC_VECTOR(6 DOWNTO 0)); -- hex displays
END NumberDisplay;

ARCHITECTURE DisplayNumbers OF NumberDisplay IS
COMPONENT SevenSegment PORT(-- Declare the 7 segment component to be used
dataIn: IN INTEGER;
segmentsOut: OUT STD_LOGIC_VECTOR(6 DOWNTO 0) );
END COMPONENT;

SIGNAL ms, ms10, ms100, seconds, seconds10: INTEGER:=0;
BEGIN
-- Each hex displays a different decimal place of the milliseconds
Showsms: SevenSegment PORT MAP (ms, hex0);
Show10ms: SevenSegment PORT MAP (ms10, hex1);
Show100ms: SevenSegment PORT MAP (ms100, hex2);
Shows: SevenSegment PORT MAP (seconds, hex3);
Show10s: SevenSegment PORT MAP (seconds10, hex4);
-- Calculate the time to display by modulusing from the milliseconds.
ms <=0;
ms10 <=Milliseconds/10-(Milliseconds/100)*10;
ms100 <=Milliseconds/100-(Milliseconds/1000)*10;
seconds <=Milliseconds/1000-(Milliseconds/10000)*10;
seconds10<=Milliseconds/10000;
END DisplayNumbers;

LIBRARY ieee;
```

```

USE ieee.std_logic_1164.ALL;
USE ieee.numeric_std.ALL;

-- ENTITY XRayInterface
-- This is the main interface between the xray source &
-- the xray detector, and the integration time choices

ENTITY XRayInterface IS PORT(
sw : IN UNSIGNED(17 DOWNTO 0); -- dip switches for trigger and settings
key : IN UNSIGNED(3 DOWNTO 0); -- push buttons
hex5,hex4,hex3,hex2,hex1: OUT STD_LOGIC_VECTOR(6 DOWNTO 0); -- hex displays
ledg : OUT STD_LOGIC_VECTOR(8 DOWNTO 0); -- LEDs for status
ledr : OUT STD_LOGIC_VECTOR(17 DOWNTO 0); -- red LEDs for testing
gpio_0 : INOUT STD_LOGIC_VECTOR(35 DOWNTO 0); -- GPIO 0 pins
clock_50 : IN STD_LOGIC; -- the 50MHz Clock
--gpio_0(1) : NA-OUT N/A
--gpio_0(3) : NA+ OUT
--gpio_0(9) : TRIG_IN+ OUT XRD Ext Trigger
--gpio_0(11): TRIG_IN-OUT
--gpio_0(14): FR_SYNC-IN Output from XRD to synchronize source
--gpio_0(15): FR_SYNC+ IN
--gpio_0(20): FR_EN+ IN Output from XRD to signify start of new frame
--gpio_0(21): FR_EN-IN
--gpio_0(35): XRAY_TRIG IN Sent to xray source to trigger exposure (L19)
END XRayInterface;

ARCHITECTURE SystemInterface OF XrayInterface IS

--Component to display the integration time that is chosen.
COMPONENT NumberDisplay IS PORT(
Milliseconds: IN INTEGER;
clock: IN STD_LOGIC;
hex4,hex3,hex2,hex1,hex0 : OUT STD_LOGIC_VECTOR(6 DOWNTO 0)); -- hex displays
END COMPONENT;

--These are the states for the sequential logic

TYPE states IS ( EDIT_BETWEEN_BUTTON_PRESSES, -- waiting between button presses
EDIT_BUTTON_PRESSED,-- edit the time on the button press
EDIT_UPDATE_DISPLAY,-- update the time on the display
EDIT_WAIT_BUTTON_DEPRESS,-- wait for them to unpress the button
EDIT_WAIT_AFTER_BUTTON_PRESS, -- wait to debounce
RUN_BETWEEN_FRAMES,-- Waiting between frames
RUN_XRAY_PREP_ON,-- Waiting for XRS to turn off
RUN_XRAY_PREP,-- Waiting for the x-rays to prep
RUN_RESET_FRAME,-- Reset the detector frame
RUN_RESET_TIMER1,-- Reset the timer
RUN_INTEGRATION,-- Wait for integration time
RUN_RESEAT_TIMER2,-- Reset the timer
RUN_READ_FRAME,-- Read out the frame
RUN_AFTER_FRAME); -- Reset before waiting for another frame
SIGNAL state: states:=RUN_BETWEEN_FRAMES;
SIGNAL next_state: states;
SIGNAL display_updated: STD_LOGIC:= '0';
SIGNAL IntegrationTime, MillisecondsPassed, TimeToDisplay: INTEGER RANGE 0 to 99999;
SIGNAL TimeCounter: UNSIGNED(15 DOWNTO 0):="0000000000000000"; -- 16 digit binary time counter
SIGNAL accumulator: BIT:= '0';
SIGNAL edit_mode, run_mode, integration_mode: STD_LOGIC; -- flags for different modes of operation
SIGNAL TRIG_IN, X_TRIGGER: STD_LOGIC; -- output to detector, input from source
SIGNAL TEST_LEDS: STD_LOGIC_VECTOR(12 DOWNTO 0):="00000000000000";
SIGNAL ms, ms10, ms100, seconds: INTEGER:=0; -- keep track of decimals of integration time
BEGIN

-- instantiate the hexadecimal number display
DisplayNumbers: NumberDisplay PORT MAP(TimeToDisplay, clock_50, hex5, hex4, hex3, hex2, hex1);
-- the Edit mode is selected by a switch
edit_mode<= sw(0);
-- for ease of code, run_mode is just not when in Edit mode
run_mode <=not sw(0);
ledr(0)<= edit_mode;
-- shines when in integration mode
ledg(8)<=integration_mode;
-- Calculate the differential output signal to the detector
gpio_0(9)<=TRIG_IN;
gpio_0(11)<= not TRIG_IN;
ledg(0)<=TRIG_IN;
-- FR_SYNC
--FRAME_SYNC<=gpio_0(15);
--FRAME_SYNC_TRUE<=gpio_0(15) XOR gpio_0(14);
-- FR_EN
--FRAME_ENABLE<=gpio_0(20);
--FRAME_ENABLE_TRUE<=gpio_0(20) XOR gpio_0(21);
-- XRAY_trigger

-- The input from the source
X_TRIGGER<=gpio_0(35);
ledg(6)<=gpio_0(35);

--TEST leds to show the state machine states
--ledr(17 downto 5)<=TEST_LEDS(12 downto 0);

-- PROCESS stateMachine is the sequential logic for the program
stateMachine: PROCESS(clock_50)

```

```

BEGIN
--Determine the next state to be in on the clock edge
IF (RISING_EDGE(clock_50)) THEN
-- Accumulate the counter when necessary
IF (accumulator='1') THEN
TimeCounter<=TimeCounter+1;
END IF;
-- Every 1 ms, reset timer and count up milliseconds in an Integer
IF (TimeCounter="1100001101010000") THEN
MillisecondsPassed<=MillisecondsPassed+1;
TimeCounter<="0000000000000000";
END IF;

--Determine the next state
CASE state IS

-- EDIT MODE
WHEN EDIT_BETWEEN_BUTTON_PRESSES =>
-- If a key is pressed, move forward to button press
-- If edit mode is turned off, leave edit mode to run mode
-- Otherwise, wait hear for a button press
IF ((key(3)='0' OR key(2)='0' OR key(1)='0' OR key(0)='0') AND edit_mode='1') THEN
next_state<=EDIT_BUTTON_PRESSED;
ELSE
IF (edit_mode='0') THEN
next_state<=RUN_BETWEEN_FRAMES;
ELSE
next_state<=EDIT_BETWEEN_BUTTON_PRESSES;
END IF;
END IF;
WHEN EDIT_BUTTON_PRESSED =>
--This state will automatically change when the button press has been computed
next_state<=EDIT_UPDATE_DISPLAY;
WHEN EDIT_UPDATE_DISPLAY =>
-- This state will automatically change when the update has been made
next_state<=EDIT_WAIT_BUTTON_DEPRESS;
WHEN EDIT_WAIT_BUTTON_DEPRESS =>
-- If a key is still being pressed, wait here
-- If not, move to first stage in Edit mode
IF (key(3)='1' AND key(2)='1' AND key(1)='1' AND key(0)='1') THEN
next_state<=EDIT_WAIT_AFTER_BUTTON_PRESS;
ELSE
next_state<=EDIT_WAIT_BUTTON_DEPRESS;
END IF;
WHEN EDIT_WAIT_AFTER_BUTTON_PRESS =>
-- Wait for a little while before going back to the edit mode base
-- in order to debounce and leave time for math calculations
IF (MillisecondsPassed>=30) THEN
next_state<=EDIT_BETWEEN_BUTTON_PRESSES;
ELSE
next_state<=EDIT_WAIT_AFTER_BUTTON_PRESS;
END IF;

--RUN MODE
WHEN RUN_BETWEEN_FRAMES =>
-- Wait for the signal from the xray source to go active, or enter edit_mode
IF ((X_TRIGGER='1' OR sw(17)='1') AND run_mode='1') THEN

--TEST

--IF (sw(17)='1' AND run_mode='1') THEN
next_state<=RUN_XRAY_PREP_ON;
ELSE
IF (edit_mode='1') THEN
next_state<=EDIT_BETWEEN_BUTTON_PRESSES;
ELSE
next_state<=RUN_BETWEEN_FRAMES;
END IF;
END IF;
WHEN RUN_XRAY_PREP_ON =>
-- Wait for signal from xray source to go back inactive, or enter edit mode
IF (X_TRIGGER='0' AND sw(17)='0' AND run_mode='1') THEN -- x-ray trigger off

--TEST

--IF (sw(17)='0' AND run_mode='1') THEN
next_state<=RUN_XRAY_PREP;
ELSE
IF (edit_mode='1') THEN
next_state<=EDIT_BETWEEN_BUTTON_PRESSES;
ELSE
next_state<=RUN_XRAY_PREP_ON;
END IF;
END IF;
WHEN RUN_XRAY_PREP =>
--Wait for signal from xray source to go active again, or enter edit mode
IF ((X_TRIGGER='1' OR sw(17)='1') AND run_mode='1') THEN -- if the x-ray trigger has gone
--IF (sw(17)='1' AND run_mode='1') THEN
next_state<=RUN_RESET_FRAME;
ELSE
IF (edit_mode='1') THEN
next_state<=EDIT_BETWEEN_BUTTON_PRESSES;

```

```

ELSE
next_state<=RUN_XRAY_PREP;
END IF;
END IF;
WHEN RUN_RESET_FRAME =>
--pulse the xray detector to read a frame to clear it
--Wait for 20us to pass to move on
IF (TimeCounter="0000001111101000") THEN -- after 20us have passed
next_state<=RUN_RESET_TIMER1;
ELSE
next_state<=RUN_RESET_FRAME;
END IF;
WHEN RUN_RESET_TIMER1 =>
--reset timers, then move on to actual integration
next_state<=RUN_INTEGRATION;
WHEN RUN_INTEGRATION =>
-- Count up to the integration time, then move on, or cancel by entering edit mode
IF (MillisecondsPassed=IntegrationTime) THEN --Integration time has passed
next_state<=RUN_RESET_TIMER2;
ELSE
IF (edit_mode='1') THEN
next_state<=EDIT_BETWEEN_BUTTON_PRESSES;
ELSE
next_state<=RUN_INTEGRATION;
END IF;
END IF;
WHEN RUN_RESET_TIMER2 =>
--reset the timers, then move on
next_state<=RUN_READ_FRAME;
WHEN RUN_READ_FRAME =>
-- pulse the xray detector to read the frame
IF (TimeCounter="0000001111101000") THEN -- 20 us have passed
next_state<=RUN_BETWEEN_FRAMES;
ELSE
next_state<=RUN_READ_FRAME;
END IF;
WHEN RUN_AFTER_FRAME =>
IF (X_TRIGGER='0' AND sw(17)='0') THEN
next_state<=RUN_BETWEEN_FRAMES;
ELSE
next_state<=RUN_AFTER_FRAME;
END IF;
END CASE;
END IF;
-- What to do at each state
IF (RISING_EDGE(clock_50)) THEN
state<=next_state;
CASE state IS
-- EDIT MODE
WHEN EDIT_BETWEEN_BUTTON_PRESSES =>
display_updated<='0';
accumulator<='0'; -- don't count time
MillisecondsPassed<=0; -- reset to 0
TimeCounter<="0000000000000000"; -- reset to 0
integration_mode<='0'; -- not integrating
TRIG_IN<='1'; -- inactive high
TEST_LEDS<="100000000000";
WHEN EDIT_BUTTON_PRESSED =>
-- display_updated is a safety so that if these math calculations
-- take more than one clock cycle (they do),
-- the calculation won't be performed twice.
if (display_updated='0') THEN
-- Determine the change in set integration time based on button press
IF (key(3)='0' AND IntegrationTime<99000) THEN -- Up 100
IntegrationTime<=IntegrationTime+1000;
END IF;
IF (key(2)='0' AND IntegrationTime>=1000) THEN -- Down 100
IntegrationTime<=IntegrationTime-1000;
END IF;
IF (key(1)='0' AND IntegrationTime<99990) THEN -- Up 10
IntegrationTime<=IntegrationTime+10;
END IF;
IF (key(0)='0' AND IntegrationTime>=10) THEN -- Down 10
IntegrationTime<=IntegrationTime-10;
END IF;
display_updated<='1';
END IF;
TEST_LEDS<="010000000000";
WHEN EDIT_UPDATE_DISPLAY =>
TimeToDisplay<=IntegrationTime; -- update time
TEST_LEDS<="001000000000";
WHEN EDIT_WAIT_BUTTON_DEPRESS =>
TEST_LEDS<="000100000000";
WHEN EDIT_WAIT_AFTER_BUTTON_PRESS =>
accumulator<='1'; -- don't count time
-- RUN MODE
WHEN RUN_BETWEEN_FRAMES =>
accumulator<='0'; -- don't count time
MillisecondsPassed<=0; -- reset to 0
TimeCounter<="0000000000000000"; -- reset to 0
TRIG_IN<='1'; -- inactive high
TEST_LEDS<="000010000000";

```

```

WHEN RUN_XRAY_PREP_ON =>
-- nothing new
TEST_LEDS<="0000010000000";
WHEN RUN_XRAY_PREP =>
-- nothing new
TEST_LEDS<="0000001000000";
WHEN RUN_RESET_FRAME =>
accumulator<='1'; -- count time
TRIG_IN<='0'; -- active low to pulse detector
TEST_LEDS<="0000000100000";
WHEN RUN_RESET_TIMER1 =>
TRIG_IN<='1'; -- bring back to inactive high
accumulator<='0'; -- don't count time
TimeCounter<="000000000000000"; --reset clock to 0
TEST_LEDS<="0000000010000";
WHEN RUN_INTEGRATION =>
accumulator<='1'; -- count time
integration_mode<='1'; -- flag for this state
TEST_LEDS<="0000000001000";
WHEN RUN_RESET_TIMER2 =>
accumulator<='0'; -- don't count time
TimeCounter<="000000000000000"; --reset clock to 0
integration_mode<='0'; -- integration is over
MillisecondsPassed<=0;
TEST_LEDS<="0000000000100";
WHEN RUN_READ_FRAME =>
accumulator<='1'; -- count time
TRIG_IN<='0'; -- active low to pulse detector
TEST_LEDS<="0000000000010";
WHEN RUN_AFTER_FRAME =>
accumulator<='0'; -- don't count time
TRIG_IN<='1'; -- inactive high
TEST_LEDS<="0000000000001";
END CASE;
END IF;
END PROCESS;
END SystemInterface;

```

B | Synchronization boards

These schematics are for the printed circuit boards used to synchronize the x-ray detectors and the x-ray source at Roberts Research Institute. The x-ray source controller there had a BNC connector that could be used to trigger pulses.

In the case of the XRD0820 sync board, the main purpose is to convert the GPIO signals from the FPGA on the Altera DE2 into LVDS, and vice versa, while sending a signal on a cable to the x-ray source controller.

In the case of the FLAATZ-330N sync board, the board buffers the “X-ray exposure” signal that is sent between the hand switch and the detector as a signal to be sent to the x-ray source controller.

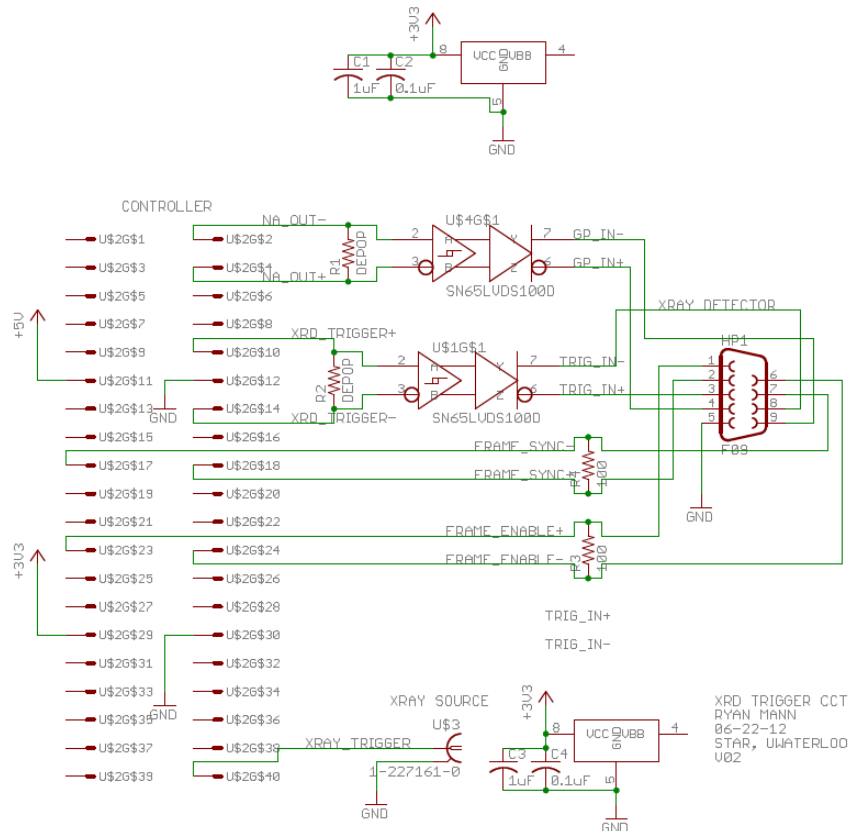


Figure B.1: Synchronization board schematic for XRD0820.

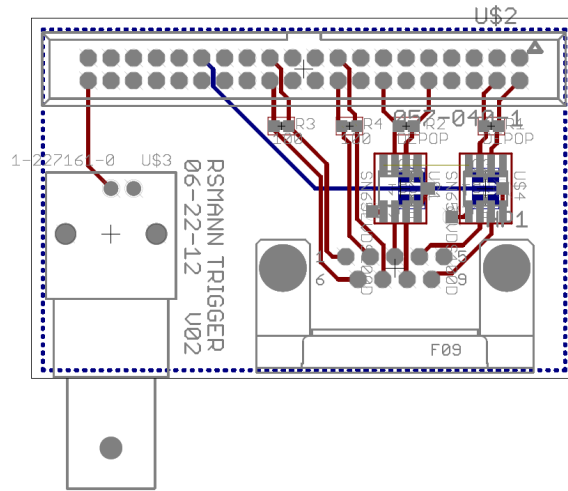


Figure B.2: Synchronization board layout for XRD0820.

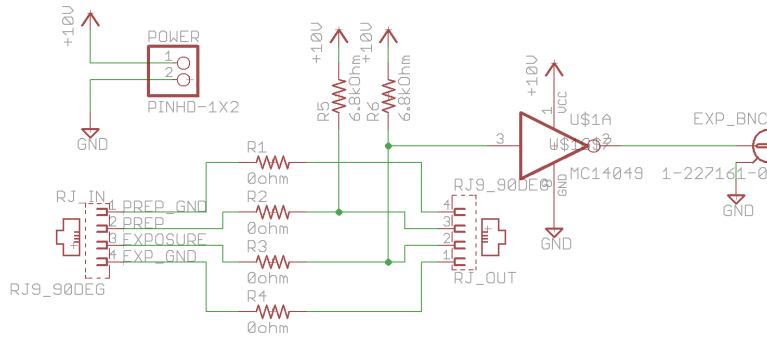


Figure B.3: Synchronization board schematic for FLAATZ-330N.

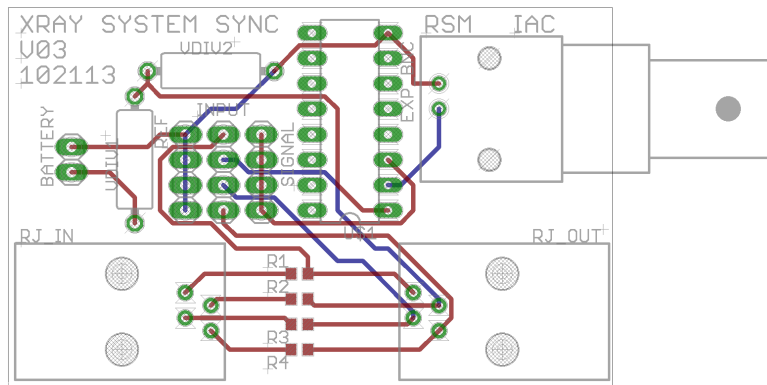


Figure B.4: Synchronization board layout for FLAATZ-330N.

C | X-ray source cabinet

These are the 3D schematics of the x-ray cabinet used in the lab. Also included are the printed circuit board schematics used in the door interlock. A physical switch in the door handle prevents x-ray exposure from occurring while the door is open.

3D FRONT/TOP VIEW

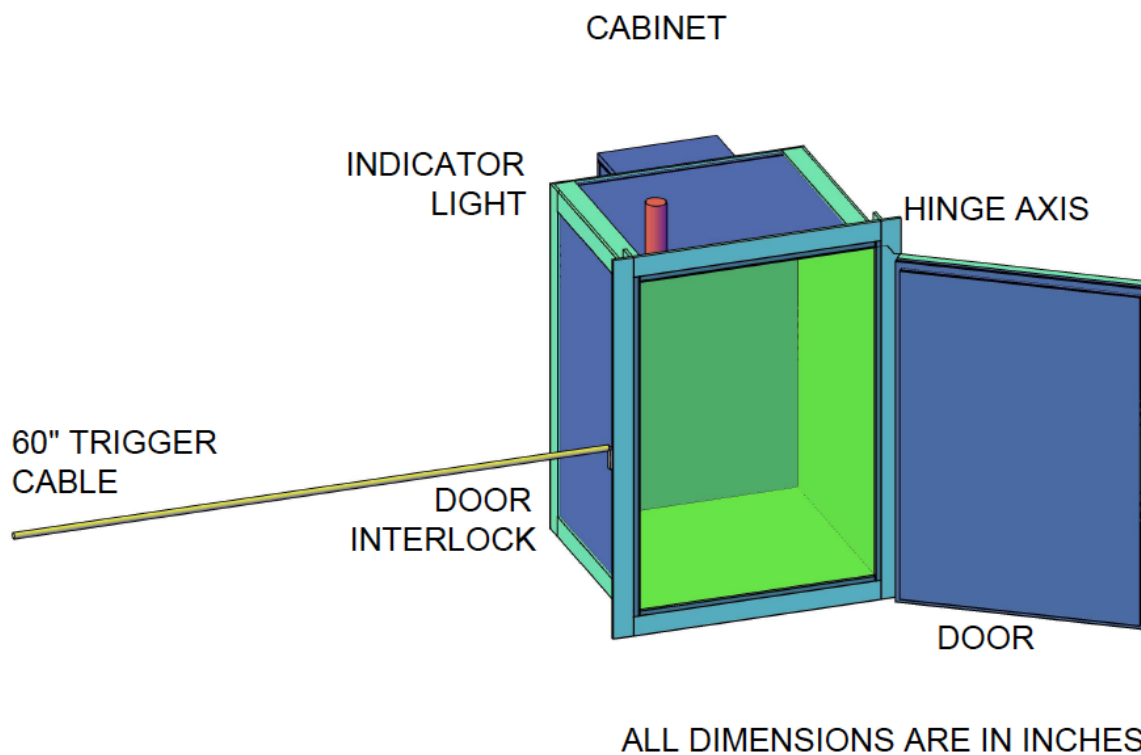
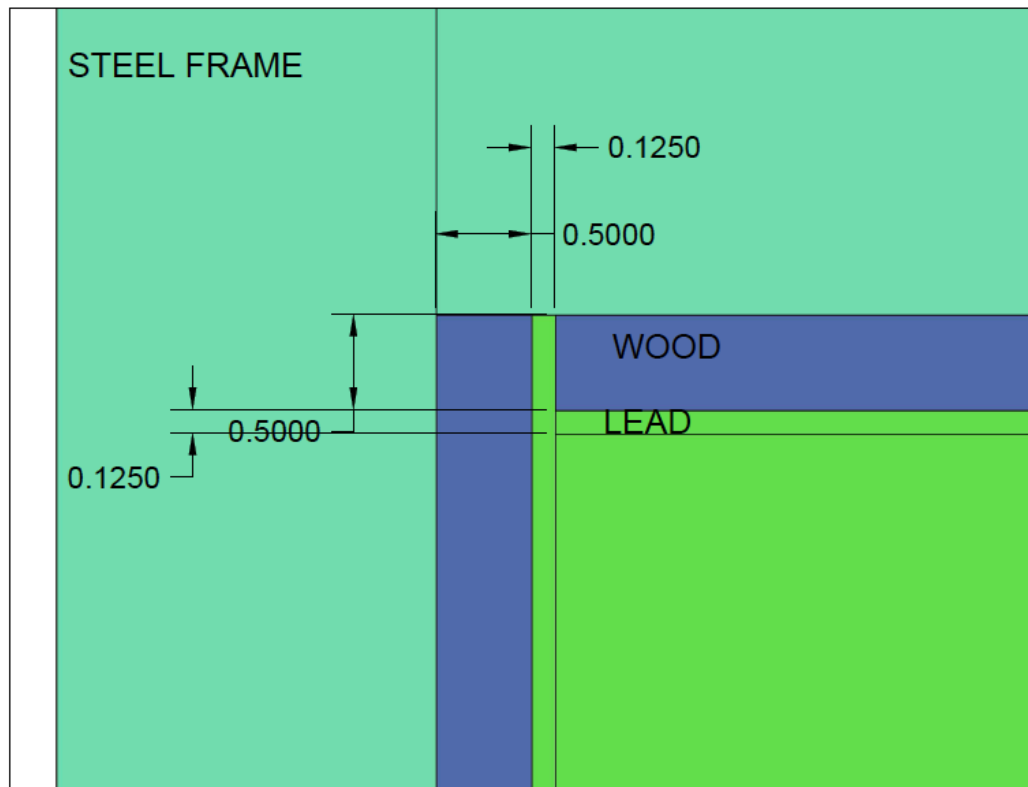


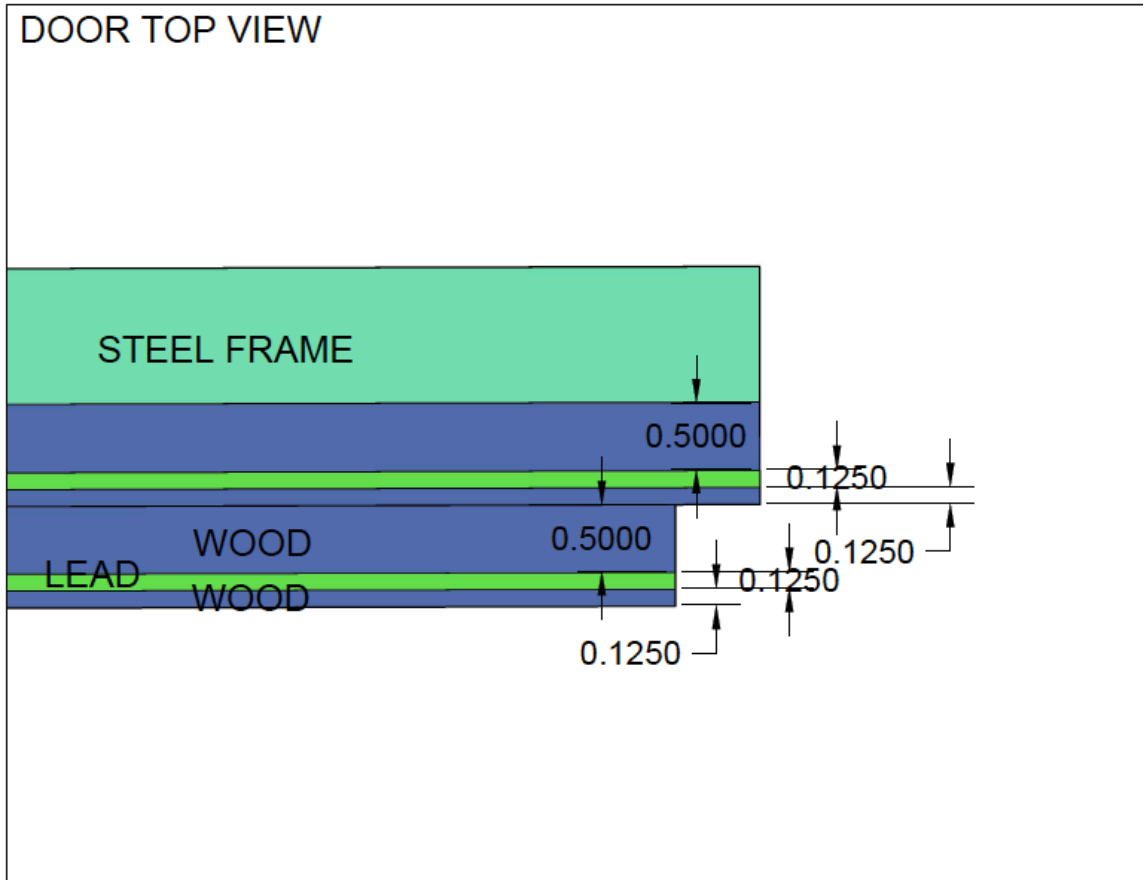
Figure C.1: 3D Front/Top View

CABINET
FRONT VIEW



ALL DIMENSIONS ARE IN INCHES

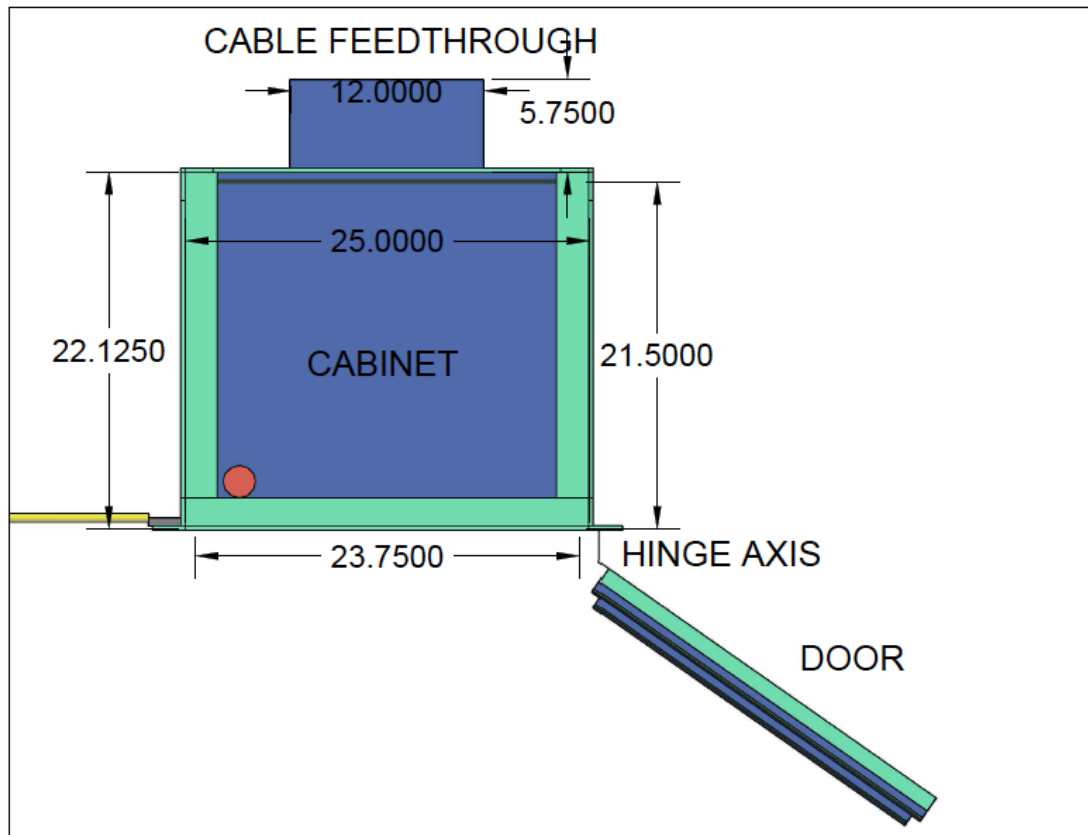
Figure C.2: Cabinet front view



ALL DIMENSIONS ARE IN INCHES

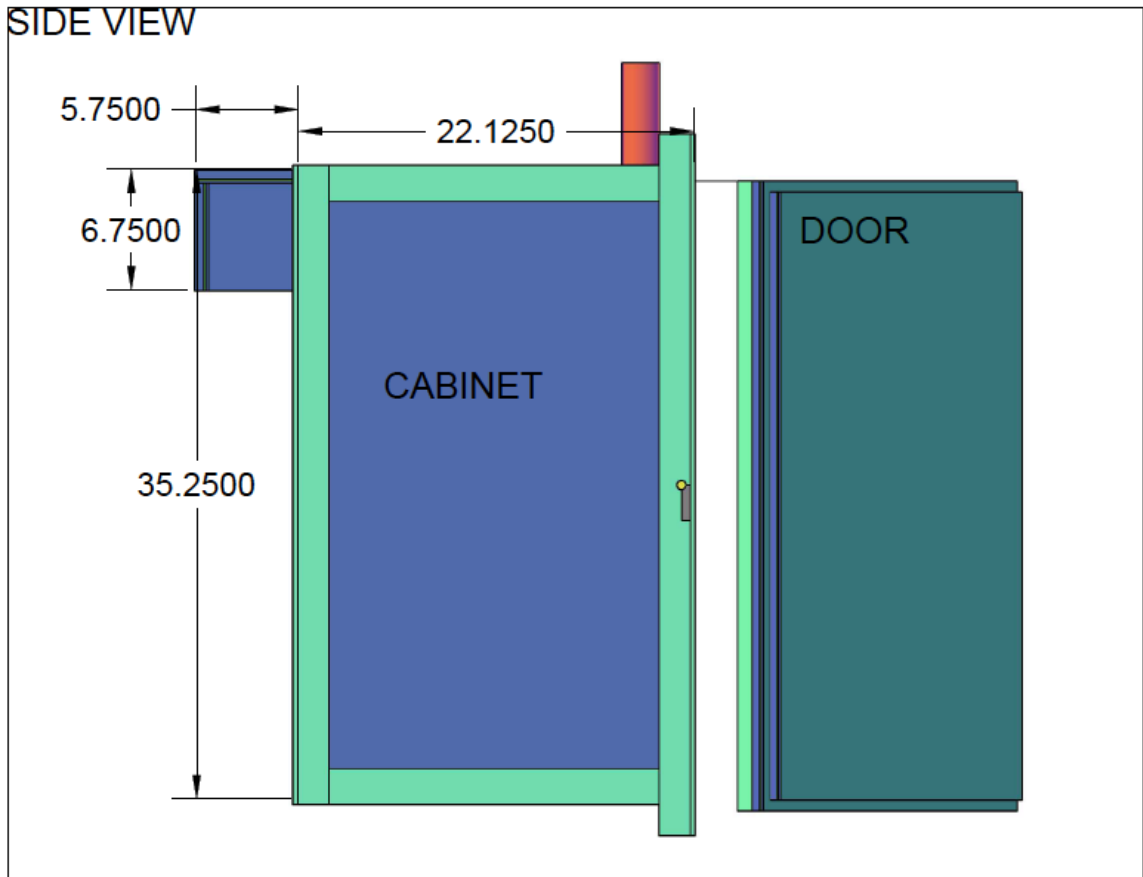
Figure C.3: Door top view

TOP VIEW



ALL DIMENSIONS ARE IN INCHES

Figure C.4: Top view



ALL DIMENSIONS ARE IN INCHES

Figure C.5: Side view

CABLE FEEDTHROUGH
BOTTOM 3D VIEW

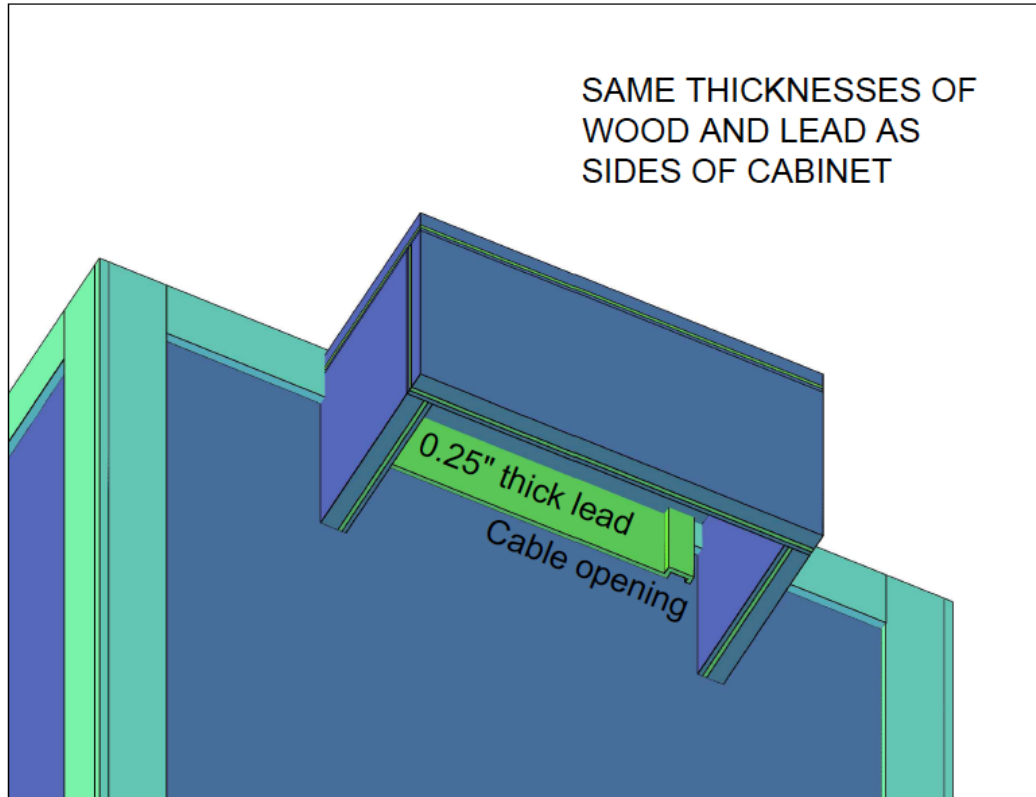


Figure C.6: Cable feedthrough (Bottom 3D View)

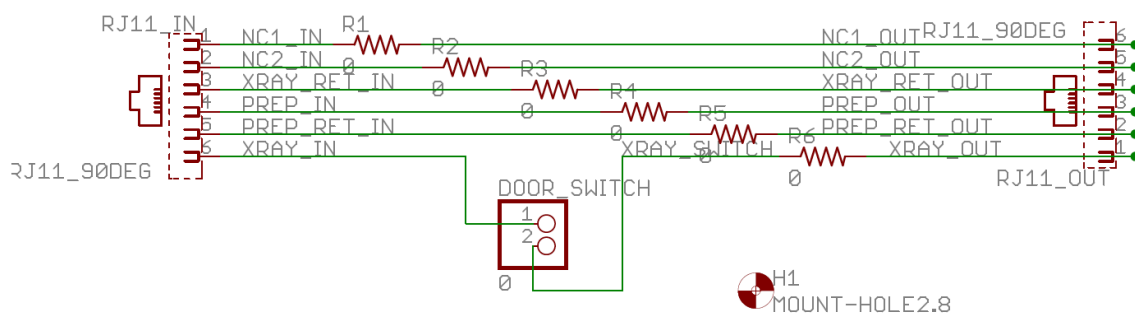


Figure C.7: Interlock board schematic

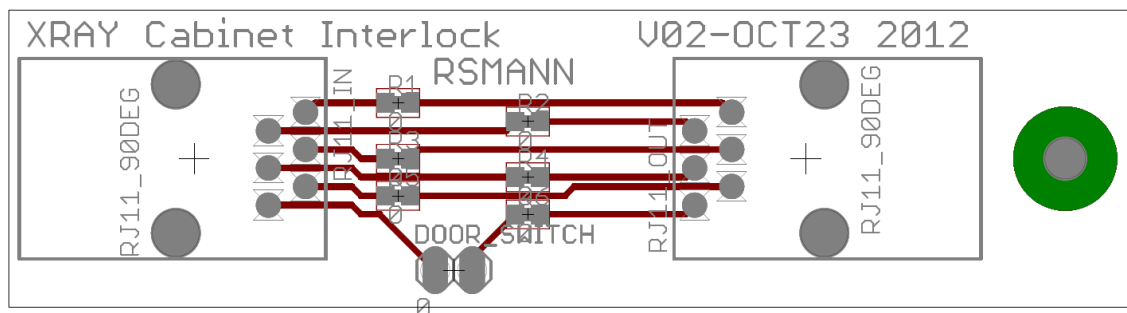


Figure C.8: Interlock board layout

D | Parts lists

The following parts were required for the interlock circuit for the x-ray cabinet, listed in Table D.1.

Table D.1: Parts for the x-ray cabinet interlock

Function	Manufacturer	Part Number	Quantity
RJ11 modular jack	Molex	42878-6218	2
Modular cord 7' 6p6c	Assman WSW Components	A1662R-07-ND	1
Custom PCB	Alberta Printed Circuit	N/A	1
Door-activated switch	Unknown	N/A	1

The following parts were included with the PerkinElmer XRD0820 indirect conversion x-ray detector, listed in Table D.2.

Table D.2: Parts included with the XRD0820

PerkinElmer Part No.	Description
95510214H	PCI Frame Grabber XRD-FG
95510225	Interface Cable 100ft/30.5m
95510254H	Power supply
95510583H	XRD-EPS DC Cable 100ft/30.5m
95510332H	AC Power cable

The following parts were required for the synchronization circuitry for the XRD0820 x-ray system, listed in Table D.3.

The following parts were used with the DRTech FLAATZ-330N direct conversion x-ray detector, listed in Table D.4. Some parts were included with the FLAATZ, but some AC power conversion parts were purchased separately.

Table D.3: Parts for the synchronization circuitry

Function	Manufacturer	Part Number	Quantity
LVDS differential line driver/receiver	Texas Instruments	SN65LVDS050D	2
DB9 plug, right angle	TE Connectivity	1734351-1	1
40-pin header	TE Connectivity	5103308	1
40-pin cable	Assman WSW Components	AK5430-.5-(R)	1
Resistor (100Ohm, 0603 package)	Panasonic Electronic Components	ERJ-3GEYJ101V	2
Capacitors (0.1uF, 0603 package)	Kemet	C0603C104K4RACTU	2
Capacitors (1uF, 0603 package)	Kemet	C0603C105K8PACTU	2
BNC socket, right angle	TE Connectivity	1337543	1
Custom PCB	Alberta Printed Circuit	N/A	1

Table D.4: Parts used with the FLAATZ-330N

Description	Options	Incl.?
Control Box	Ethernet Type	Y
X-ray Hand Switch Box	Wire Type	Y
CD-ROM		Y
Interface cable	MDR type, 15m	Y
X-ray Cable	Wire, 7.6m	Y
AC Power cable	European 220V	Y
X-ray hand switch		Y
LAN cable	15m	Y
LAN card		Y
Calibration software		Y
Transformer	NA 220V to NA 110V	N
Power converter cable	NA 220V to European 220V	N

E | Detector images

The following images were used to calculate the MTF of the PerkinElmer XRD0820 (Figures E.1 and E.2) and the DRTech FLAATZ-330N (Figures E.3 and E.4).



Figure E.1: Edge image for calculating MTF in the x-direction of the XRD0820.



Figure E.2: Edge image for calculating MTF in the y-direction of the XRD0820.

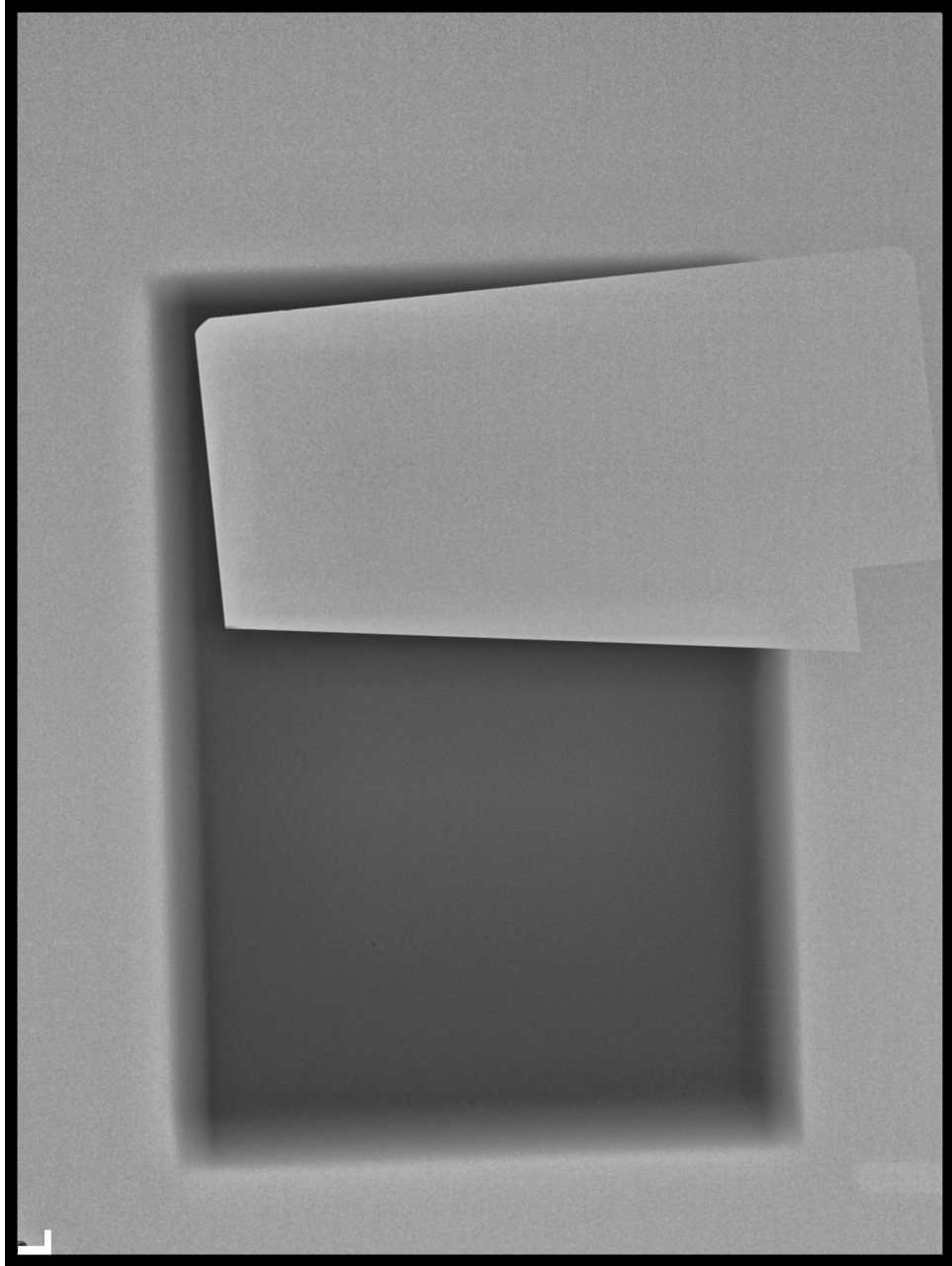


Figure E.3: Edge image for calculating MTF in the x-direction of the FLAATZ-330N (rotated).

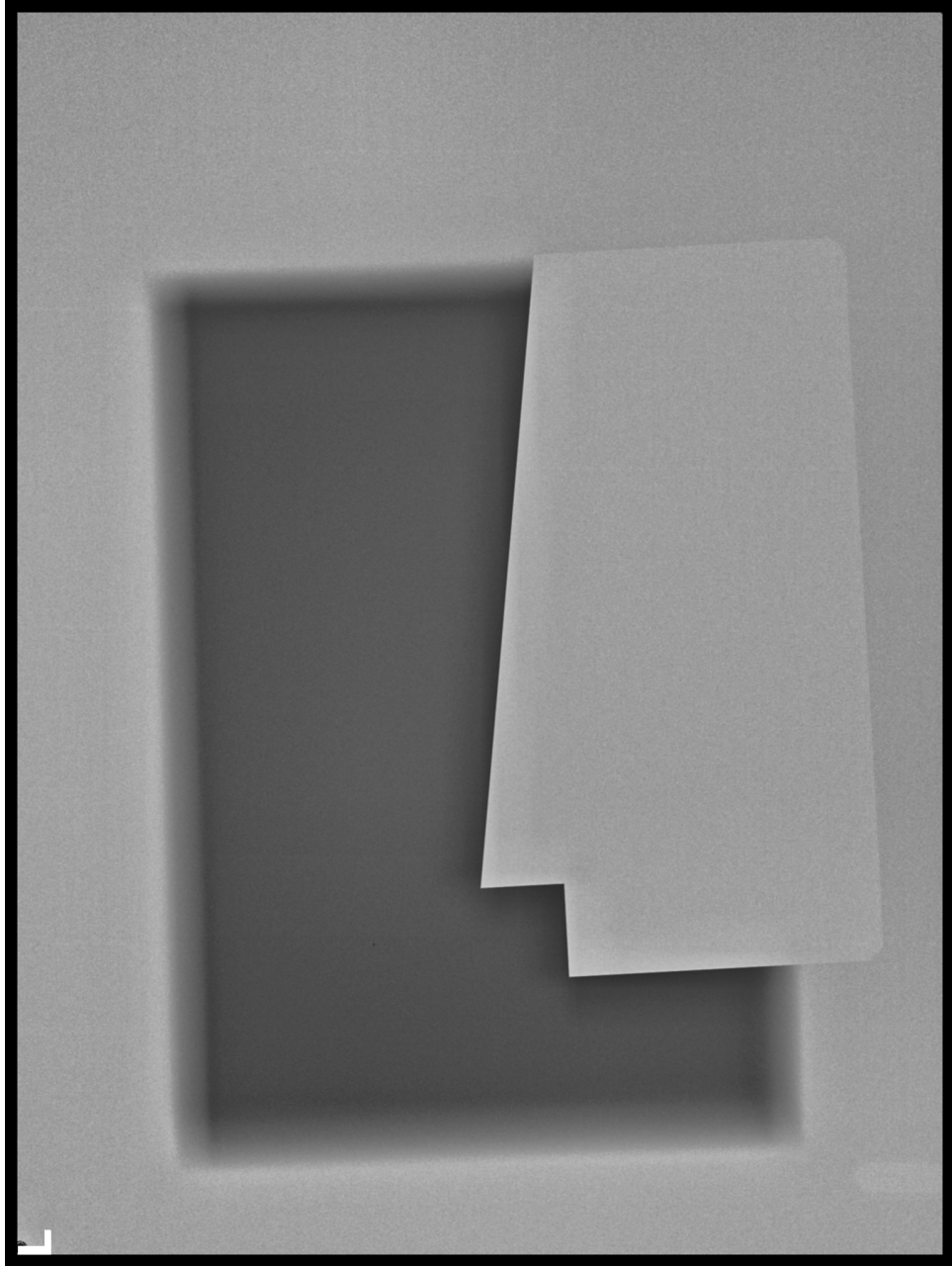


Figure E.4: Edge image for calculating MTF in the y-direction of the FLAATZ-330N (rotated).

F | Efficacy study information letter

This information letter was sent to participants in the region-of-interest efficacy study. A link was provided to the online survey.

Investigation Into Chest X-ray Region of Interest Tuberculosis Diagnosis

You are invited to participate in a research study conducted by Ryan Mann, under the supervision of Prof. Karim Karim, Electrical and Computer Engineering, of the University of Waterloo, Canada. The objectives of the research study are to determine the accuracy of tuberculosis diagnosis given individual lung x-rays.

If you decide to volunteer, you will be asked to complete a 60-minute online survey. Survey questions focus on the diagnosis of pulmonary tuberculosis. Participation in this study is voluntary. You may decline to answer any questions that you do not wish to answer and you can withdraw your participation at any time by not submitting your responses. There are no known or anticipated risks from participating in this study.

It is important for you to know that any information that you provide will be confidential. All of the data will be summarized and no individual could be identified from these summarized results; however, only a few experts are invited to participate in the survey. The web site is programmed to collect responses alone and will not collect any information that could potentially identify you (such as machine identifiers).

The data, with no personal identifiers, collected from this study will be maintained on a password-protected computer database in a restricted access area of the university. As well, the data will be electronically archived after completion of the study and maintained for two years and then erased.

Should you have any questions about the study, please contact either Ryan Mann ([REDACTED]) or Prof. Karim Karim ([REDACTED]). Further, if you would like to receive a copy of the results of this study, please contact either investigator.

I would like to assure you that this study has been reviewed and received ethics clearance through the Office of Research Ethics at the University of Waterloo. However, the final decision about participation is yours. If you have any comments or concerns resulting from your participation in this study, please feel free to contact Dr. [REDACTED] in the Office of Research Ethics at 1-519-888-4567, Ext [REDACTED] or [REDACTED].

Thank you for considering participation in this study.

To complete the survey, click here on the link below and sign in with the following user name and password:

User name: [REDACTED]

Password: [REDACTED]

[REDACTED]

G | Monte Carlo simulations of an indirect x-ray detector

This paper was submitted for academic credit for the course ECE 730 T21, Digital Imaging Circuits and Technology.

G.1 Summary

This report outlines the Monte Carlo (MC) simulations performed in Matlab for an indirect X-ray detector. The report will begin with a background of X-ray and indirect detector physics, then follow with the justification for the Matlab MC code. The actual code will be included as attachments. The results of the simulations will be shown for three different classes of DRZ scintillator and for a range of X-ray photon energies. Also, results will be shown for a simulation of X-ray photons being absorbed immediately in the top layer of the scintillating material. A discussion comparing the different classes of scintillators will follow, with application to X-ray detector pixel size.

G.2 Background

According to [30], there are two principal methods to digitally detect X-rays: direct and indirect. Both methods have a flat-panel CCD or CMOS imager as the base, connected to electronic read-out circuitry and digital processing. In the case of a direct detector, the pixels are themselves constructed of a material that converts from incident X-ray photons into electron-hole pairs, which can be collected as a current and measured. In the case of an indirect detector, a phosphorous material, known as a scintillator, sits above (or beneath, depending on the design) the pixel array. This scintillating material converts the X-ray photons to visible light due to X-ray absorption and electron stimulation and re-emission. The optical photons are absorbed as electron-hole pairs inside the pixel material, which is often amorphous Silicon or another semiconducting material [30].

The focus of this report is on indirect X-ray detectors for the application of chest radiology. The chosen scintillators are from the DRZ line of $\text{Gd}_2\text{O}_2\text{S}:\text{Tb}$ phosphor screens,

Table G.1: Relevant properties of DRZ scintillator screens.

Name	Thickness (μm)	Density (mg/cm^2)
Standard	140	68
Plus	208	100
High	310	145

classified as “Standard”, “Plus” and “High” qualities; their relevant properties are listed in Table G.1.

Chest radiology typically uses X-ray photon energies of and below 80keV. The simulations shown in this report will take this distribution of energies into account.

G.3 Development of simulation code

Several steps were taken to implement the Monte Carlo simulation of X-rays impinging on an indirect X-ray detector:

- Calculating the linear attenuation coefficient curve for $\text{Gd}_2\text{O}_2\text{S:Tb}$
- Simulating the absorption of X-rays into the scintillating material
- Simulating the scattering of X-rays in the scintillator
- Simulating the creation of electron-hole pairs
- Tracing the paths of the electrons through the material as they are scattered
- Simulating the emission of visible-range photons from the interactions of electrons and scintillator atoms
- Simulating the trajectories of emitted visible-range photons

The theory and implementations are listed in the following subsections.

G.3.1 Linear attenuation coefficient calculation

The exponential decay of X-ray beam intensity in a medium is described by Beer-Lambert’s law:

$$I' = I_0 e^{-\alpha x},$$

where α is the linear attenuation coefficient, a material property, I_0 and I' are the incident intensity of light and remaining intensity of light respectively, and x is the displacement of light through the material.

This linear attenuation coefficient can be measured for any element and then calculated for any material based on the atomic mass of each atom in the molecular composition. For

gadolinium oxy-sulfide, the linear attenuation coefficient can be calculated with the sum of linear attenuation coefficients of each of the elements in its makeup, weighted by their respective concentrations. The relevant chemical properties are listed in Table G.2. The concentration can be calculated as follows [31]:

$$N = N_A \frac{\rho}{A_M},$$

where N_A is Avogadro's number, ρ is the density, and A_M is the atomic weight.

Table G.2: Relevant chemical properties of Gd, O, and S.

Element	Z	A_M (g/mol)	ρ (g/cm ³)	N (cm ⁻³)
Gd	64	157.25	7.895	3.0234x10 ²²
O	8	15.9994	1.41	5.3071x10 ²²
S	16	32.065	2.07	3.8876x10 ²²

Using the tabulated linear attenuation coefficients in [32], the linear attenuation coefficient for gadolinium oxy-sulfide can be calculated. These atomic weights can also be used to calculate the probability of hitting gadolinium, the heaviest atom in the molecular structure.

G.3.2 X-ray absorption

X-ray absorption can be simulated by using a random variable and the path length of the x-ray photon, which is based on the linear attenuation coefficient for the particular energy of the photon. When a photon is absorbed by the material, an electron is released with the same energy as the incident photon and this is called the photoelectric effect. The path length of an x-ray photon can be simulated as follows [33]:

$$x_L = -\frac{1}{\mu} \ln(R),$$

where μ is the linear attenuation coefficient at that x-ray energy, and R is a random variable from 0 to 1. It is assumed that the x-rays travel in straight lines between atomic interactions.

G.3.3 X-ray scattering

Besides absorption, there are two other interactions that will be simulated: incoherent scatter (Compton) and coherent scatter (Rayleigh). Rayleigh scattering is very unlikely according to the linear attenuation coefficients, but it will be considered in this simulation. In the case of Rayleigh scattering, the x-ray photon bounces elastically off the atom, changing direction but not losing any energy. In the case of Compton scattering, an incident x-ray interacts with a bound electron, giving some of its energy to the electron

and retaining the majority of its own, causing both particles to fly off in different directions. The new x-ray photon's wavelength is described this way [31]:

$$\lambda' = \lambda + \frac{h}{m_e c}(1 - \cos \theta),$$

where h is Planck's constant, m_e is the rest mass of an electron, c is the speed of light, θ is the angle between the initial photon path and the new photon path, and λ and λ' are the wavelengths of the incident and resultant photons, respectively. The angle will be determined with a random variable (as also in the case of elastic scattering). Using the relation,

$$E = \frac{hc}{\lambda},$$

and rearranging, the energy of the emitted x-ray photon in electron-volts is:

$$E' = \frac{hc}{\frac{hc}{E} + \frac{h(1-\cos\theta)}{m_e c}}.$$

For the purposes of this simulation, it will be assumed that an inelastic scattering will result in a change of direction of the photon of at most 45 degrees.

G.3.4 Creation of electron-hole pairs

As mentioned previously, an electron-hole pair can be created in the case of absorption (the photoelectric effect) or in Compton (inelastic) scattering. In this simulation, it will be assumed that the photoelectric effect will result in an electron being freed from the same point as the absorbed photon, with the same energy in kilo-electron-volts, and the direction will be random. In the case of Compton scattering, the energy of the electron will be the difference between the incident photon's energy and the scattered photon's energy, and its direction will be randomized (although this is an approximation; in general there are complex equations to determine this path).

G.3.5 Electron travel and scatter

As the high-energy (keV) electrons travel through the material, they have an associated "stopping power", a property similar to the x-ray linear attenuation coefficient. These stopping energies are tabulated [34], and, using an analogy to the equation for the path length of x-ray absorption, one can simulate the path length of an electron in the Gd₂O₂S:Tb material. According to the stopping energies for electrons, an electron of the same order of energy as the incident x-ray beam will have a much shorter path length. This is expected, as an electron has mass and is affected by nuclear forces and electromagnetic forces.

In this simulation, two electron collision interactions were simulated: inelastic scattering and bremsstrahlung (braking) scattering [31]. Bremsstrahlung is a radiative interaction that only occurs when the incident electron has an energy greater than the k-shell energy

of a large atom, which results in an emitted x-ray photon with that k-shell energy. This interaction is rare - it only occurs at the intersection of sufficient energy, the impact with a gadolinium nucleus, and the small probability that the reaction will not be elastic or inelastic. This simulation will consider that if this interaction occurs, an x-ray photon with the same energy of the Gd k-shell energy will be emitted, and interact with the material as previously discussed in this report.

This simulation also takes inelastic scatter into account. In this case, an electron-atom collision results in an emitted photon in the visible spectrum (2.25eV) [31], and the incident electron continues in another direction with a slightly lower energy. In the simulations, an interaction where two free electrons are produced was not simulated, for speed of simulation and for simplicity.

G.3.6 Trajectories of visible-spectrum photons

The trajectories of light photons can be assumed to emit isotropically from an electron interaction location, with the direction determined by a random variable between 0 and 2π . Using the same path length equation as in section G.3.2, but assuming the emitted photons to all be of the same wavelength and therefore of the same linear attenuation coefficient, one can determine the distance a photon travels before interacting with the material again.

At the interaction point, the photon can either be absorbed or deflected. The probability of absorption can be described as follows [33]:

$$P_a = \frac{a}{a + s},$$

where the coefficients for a (absorption path length) and s (scattering path length) were 24.2cm^{-1} and 475.8cm^{-1} , respectively [33]. In the simulation, any light photon that reached the bottom of the scintillating material is considered to be detected by the detector below the scintillator. Any photons that do not reach the bottom are not considered.

G.3.7 Code

The developed MATLAB® code can be found in `phosphorXrayMC.m`, `topLayerAbsorption.m` and `linearInterpolation.m`. `phosphorXrayMC.m` contains the main code for simulating the interactions. `topLayerAbsorption.m` assumes that all x-ray photons are absorbed immediately in the top layer of the scintillating material. `linearInterpolation.m` outlines a linear interpolation algorithm, used to determine the linear attenuation coefficient specific to each x-ray photon energy or electron energy.

G.4 Results

Six simulations were run: three of different thicknesses and densities of scintillating material (see Table G.1), and another three simulations assuming the x-ray photons are

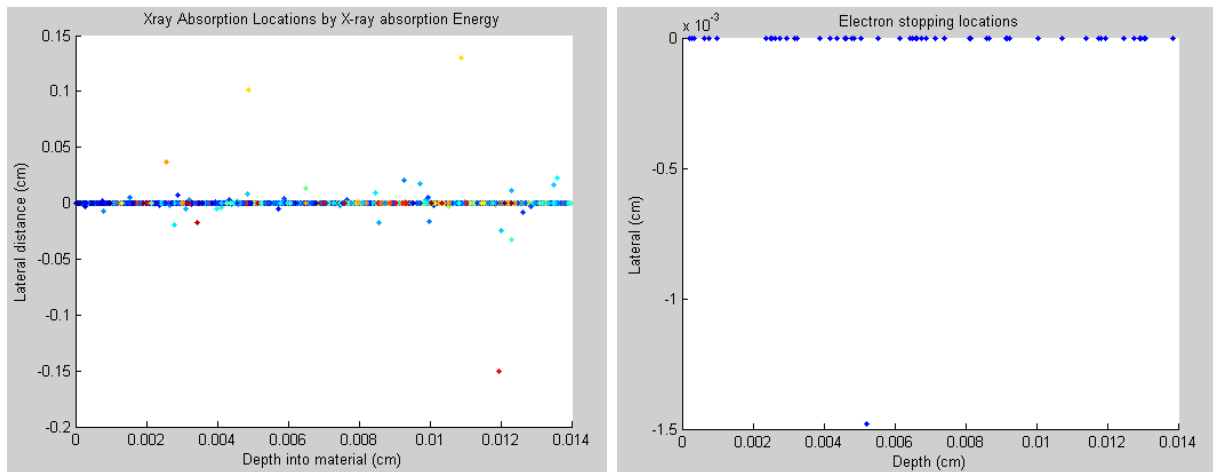
all absorbed within the top layer of the material. The simulation results include graphs showing the final absorption locations of the x-ray photons and of electrons, and the lateral spread of the photons.

G.4.1 Standard screen results

The following are the numerical settings and results from the “Standard” DRZ screen simulation, as outlined in Table G.3.

Table G.3: Numerical settings and results for DRZ Standard simulation.

Simulation	Full	Top Layer Absorption
Incident x-ray photons	10000	10000
Absorbed x-ray photons	3701	10000
X-ray maximum lateral deflection	1.503mm	N/A
Absorbed electrons	59	1
Electron maximum lateral deflection	0.015mm	3.447mm
Absorbed optical photons	716914	2379030
Optical lateral spread	0.75mm	0.8mm



(a) X-ray photon absorption

(b) Electron absorption

Figure G.1: Simulated x-ray photon and electron absorption locations, standard DRZ screen.

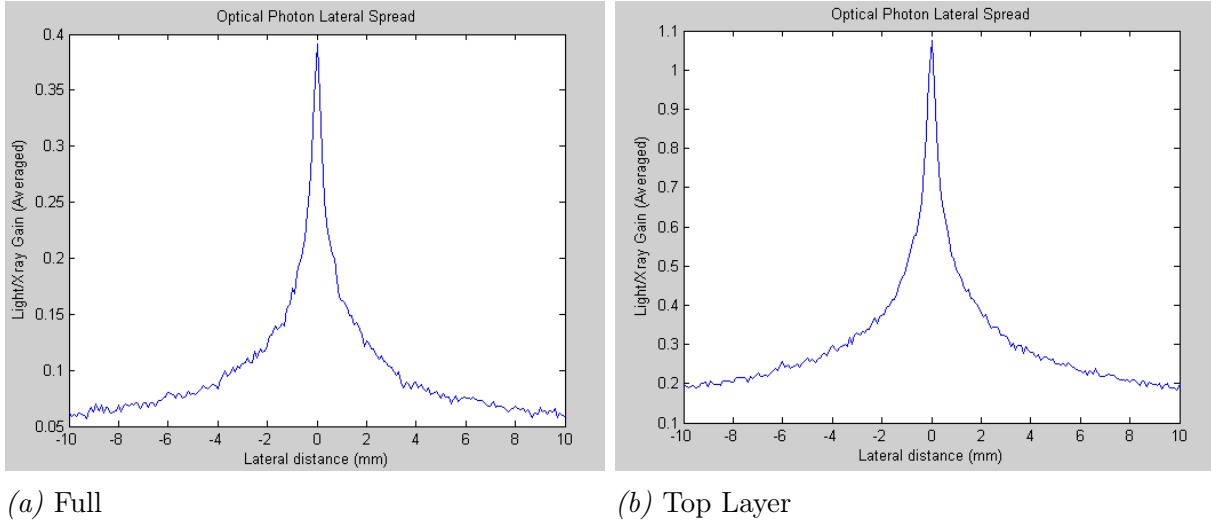


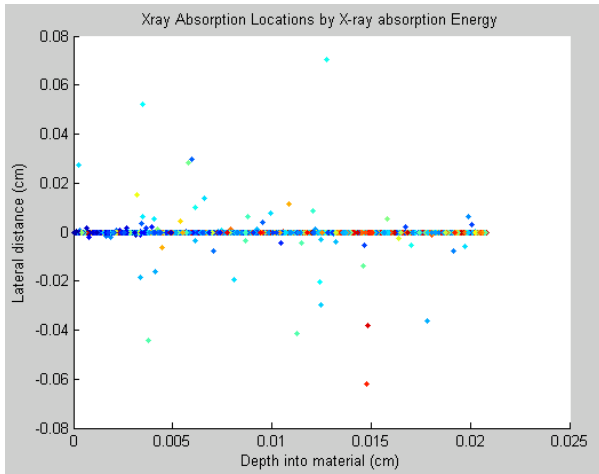
Figure G.2: Lateral spread of visible-wavelength photon absorption locations, standard DRZ screen.

G.4.2 Plus screen results

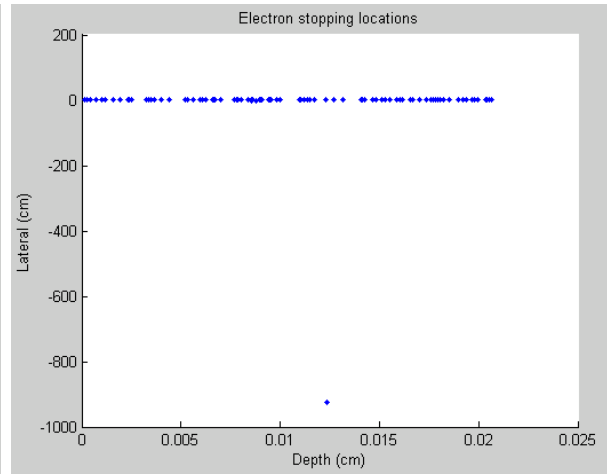
The following are the numerical settings and results from the “Plus” DRZ screen simulation, as outlined in Table G.4.

Table G.4: Numerical settings and results for DRZ Plus simulation.

Simulation	Full	Top Layer Absorption
Incident x-ray photons	10000	10000
Absorbed x-ray photons	4352	10001
X-ray maximum lateral deflection	0.706mm	0.046mm
Absorbed electrons	94	0
Electron maximum lateral deflection	9253mm	N/A
Absorbed optical photons	897015	2409820
Optical lateral spread	0.8mm	1.2mm

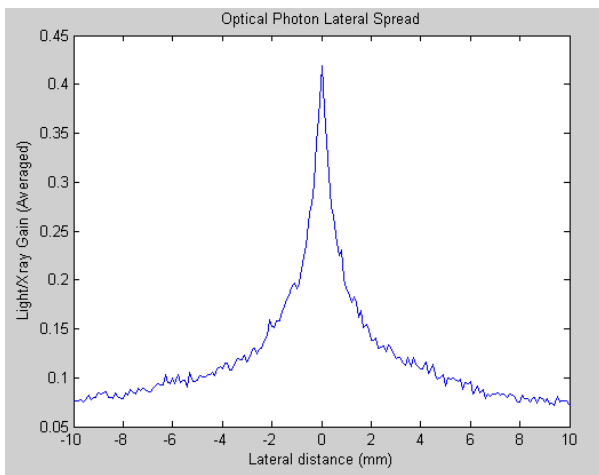


(a) X-ray photon absorption

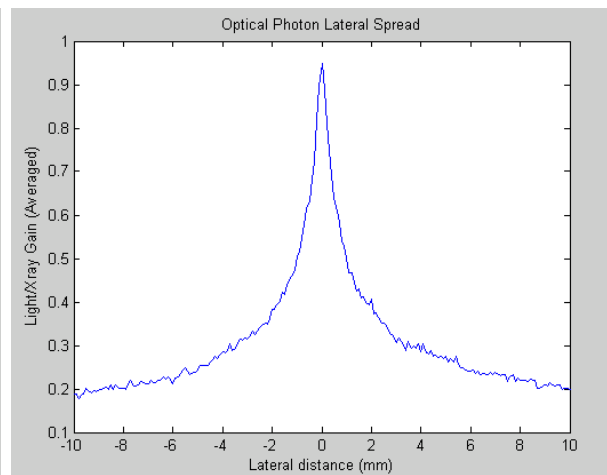


(b) Electron absorption

Figure G.3: Simulated x-ray photon and electron absorption locations, plus DRZ screen.



(a) Full



(b) Top Layer

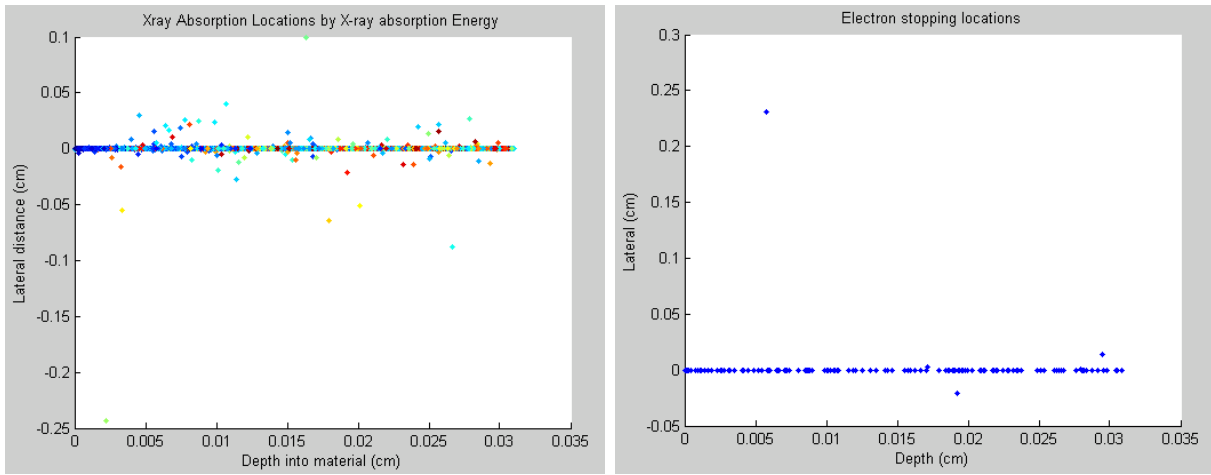
Figure G.4: Lateral spread of visible-wavelength photon absorption locations, plus DRZ screen.

G.4.3 High screen results

The following are the numerical settings and results from the “High” DRZ screen simulation, as outlined in Table G.5.

Table G.5: Numerical settings and results for DRZ High simulation.

Simulation	Full	Top Layer Absorption
Incident x-ray photons	10000	10000
Absorbed x-ray photons	5132	10001
X-ray maximum lateral deflection	2.429mm	716nm
Absorbed electrons	147	0
Electron maximum lateral deflection	2.314	N/A
Absorbed optical photons	1120868	2364363
Optical lateral spread	1.2mm	1.7mm



(a) X-ray photon absorption

(b) Electron absorption

Figure G.5: Simulated x-ray photon and electron absorption locations, high DRZ screen.

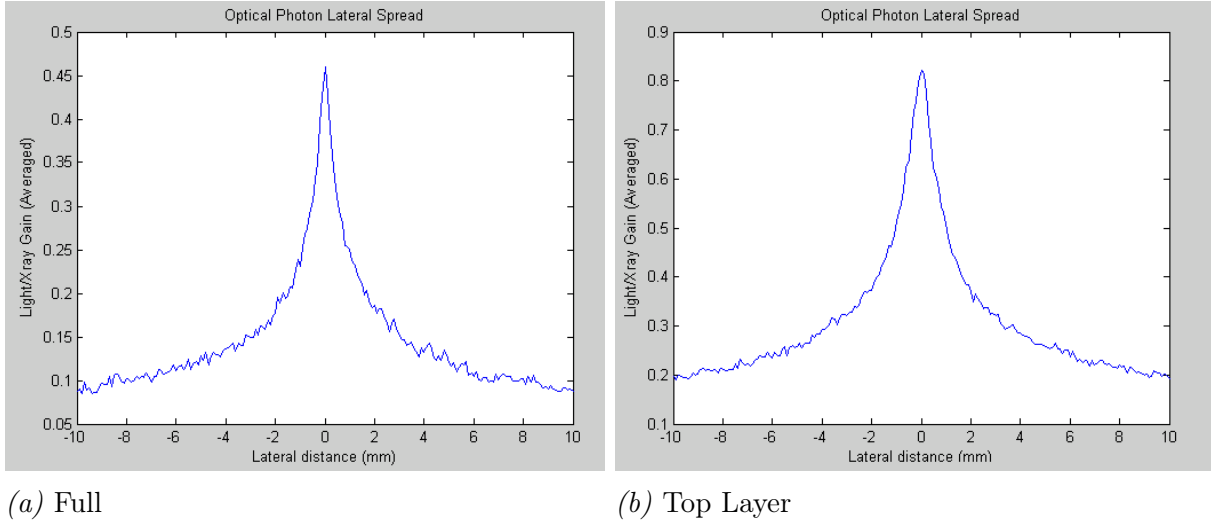


Figure G.6: Lateral spread of visible-wavelength photon absorption locations, high DRZ screen.

G.5 Analysis

A clear result can be seen: for a thicker scintillating material, the photons have a greater chance of being absorbed, but also have a greater lateral spread. This means that thicker scintillating materials are good for x-ray sensitivity, but poor for spatial resolution, compared to thinner scintillating materials, which are good for spatial resolution and poor for sensitivity.

For a pixel size of 1mm, the “High” DRZ screen would be the best, as the resolution is poor (lateral spread of about 1.2mm), but the sensitivity would be the best (about 51% of incident x-rays are absorbed in the material, and, on average, 193 optical photons are detected for every absorbed x-ray).

For a pixel size of 0.25mm, the best bet would be a “Standard” DRZ screen, as the sensitivity is poor (Only 37% of incident x-rays are absorbed in the material, and every absorbed x-ray results in an average of 218 detected optical photons), but the spatial resolution is better (lateral spread of 0.75mm).

As a mid-grade material, “Plus” DRZ would be the choice. In the case of a 0.5mm pixel, it would be a fine choice, with a lateral spread of 0.8mm and a sensitivity of 43% of incident x-rays absorbed and an average of 206 optical photons detected for every absorbed x-ray photon.

As expected, when x-rays are absorbed only in the top-most layer of the scintillator, the spread of detected photons worsens. For standard, plus, and high DRZ screens, the increase in spread is 7%, 50%, and 43%, respectively. Also, for top layer absorption, the sensitivity increases. For standard, plus, and high DRZ screens, the increase in detected light photons per absorbed x-ray photon is 9%, 17%, and 22%, respectively.

H | DQE MATLAB® code

The following three MATLAB® functions were developed to calculate the MTF, NPS, and DQE of a digital x-ray detector, given noise images and edge images.

```
function [ESF, LSF, MTF]=CalculateImageMTF(edge_image, smoothness)
    %Calculate the dimensions of the edge image
    dims=size(edge_image);
    %Project the image onto column axis to determine
    %the edge-spread function

    %We are only considering an edge along one axis, not in two dimensions
    %But we would have to calculate more of these if we wanted blur to
    %Affect rows and columns differently (which it could)

    ESF=zeros(dims(1),1);
    for column=1:dims(1)
        ESF(column)=sum(edge_image(:,column))/dims(2);
    end

    %LSF(x,y)=(dESF/dx,dESF/dy)
    % Use central differencing
    LSF=zeros(dims(1),1);
    %Go along the row of ESF
    for x=6:(dims(1)-5)
        if (x==6)
            %Forward differencing
            LSF(x)=(ESF(x+1)-ESF(x))/2;
        else
            if (x==(dims(1)-5))
                %Backward differencing
                LSF(x)=(ESF(x)-ESF(x-1))/2;
            else
                %Central differencing
                LSF(x)=(ESF(x+1)-ESF(x-1))/2;
            end
        end
    end
end

%Find the MTF by taking the Fourier Transform
MTF=abs(fft(LSF));
MTF=MTF(:,1);
if smoothness>0
    for i=1:smoothness
        for x=2:(dims(1)-1)
            MTF(x)=(MTF(x-1)+MTF(x+1))/2;
        end
    end
end
MTF=MTF-min(MTF);
MTF=MTF/max(MTF);
end
```

```
function NPS=CalculateImageNPS(image_set, smoothness)
```

```

        %Determine the dimensions of the image set
        dims=size(image_set);
        %Reserve memory for their FFTs and for the NPS
        image_set_FFT=zeros(dims);
        NPS=zeros(dims(1),dims(2));
        %Subtract the average DC value
        %Go through every image in the set
        for i=1:dims(3)
            %Calculate the average value
            average=sum(image_set(:,:,i))/(dims(1)*dims(2));
            %Subtract the average (DC) value
            image_set(:,:,i)=image_set(:,:,i)-average;
            %Calculate the 2D-FFT of these images times modulus squared
            image_set_FFT(:,:,i)=abs(fft2(image_set(:,:,i))).^2;
        end
        %Go through the FFTs pixel by pixel
        for x=1:dims(1)
            for y=1:dims(2)
                %Find the average noise at this spatial frequency
                NPS(x,y)=sum(image_set_FFT(x,y,:))/dims(3);
            end
        end
        %Normalize the NPS
        %NPS=NPS-min(min(NPS));
        %NPS=NPS/max(max(NPS));
        %Take the squared, absolute value as the NPS
        NPS=(abs(NPS)).^2;
        %Smooth
        if smoothness>0
            average_hsize=smoothness;
            A=fspecial('average', [average_hsize average_hsize]);
            NPS=imfilter(NPS,A,'same');
        end
        %Scale from 0 to 1 using the log10 scale
        logNPS_2D=log10(NPS);
        logNPS_2D=logNPS_2D-min(min(logNPS_2D));
        logNPS_2D=logNPS_2D/max(max(logNPS_2D));
        NPS=zeros(dims(1),dims(2));
        %Convert back to regular numbers
        for x=1:dims(1)
            for y=1:dims(2)
                NPS(x,y)=10^logNPS_2D(x,y);
            end
        end
        %NPS=NPS-min(min(NPS));
        %NPS=NPS/max(max(NPS));
    end

function [ESF, LSF, DQE, MTF, NPS, NPS_2D]=CalculateImageDQE(edge_image, open_images, MTF_smoothness,NPS_smoothness)
    %Calculate the dimensions of the edge image
    dims=size(edge_image);
    [ESF, LSF, MTF]=CalculateImageMTF(edge_image,MTF_smoothness);
    %Calculate the NPS using the open field images
    NPS_2D=CalculateImageNPS(open_images, NPS_smoothness);
    NPS_2D=fftshift(NPS_2D);
    dims_noise=size(NPS_2D);
    NPS=NPS_2D(dims_noise(1)/2+1,dims_noise(1)/2+1:dims_noise(1));

    %NPS=NPS(1:50)/max(NPS);
    DQE=(MTF(1:floor(dims(1)/2)).^2)./transpose(NPS(1:floor(dims(1)/2)));
    DQE(1)=0;
end

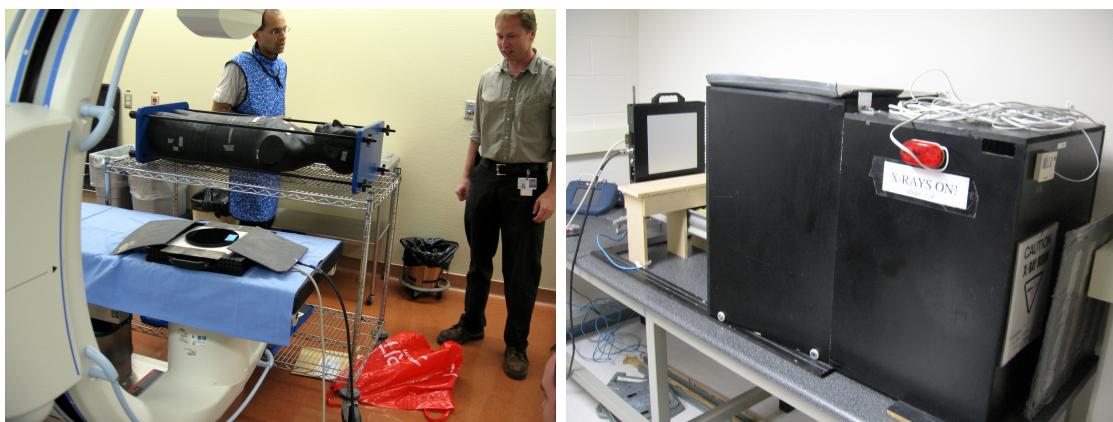
```

I | Photos

These appended photos depict lab equipment and experiments run. Please enjoy!



Figure I.1: X-ray phantom setup at the Grand River Hospital



(a) Grand River Hospital setup

(b) X-ray system at Roberts

Figure I.2: X-ray setups at the Grand River Hospital in Waterloo, and the Roberts Research Institute in London, Ontario.



Figure I.3: SourceRay SR-115 on its stand



Figure I.4: X-ray source safety labels



(a) Oblique view

(b) Side view

Figure I.5: X-ray cabinet door interlock system



Figure I.6: University of Waterloo lab setup with PC

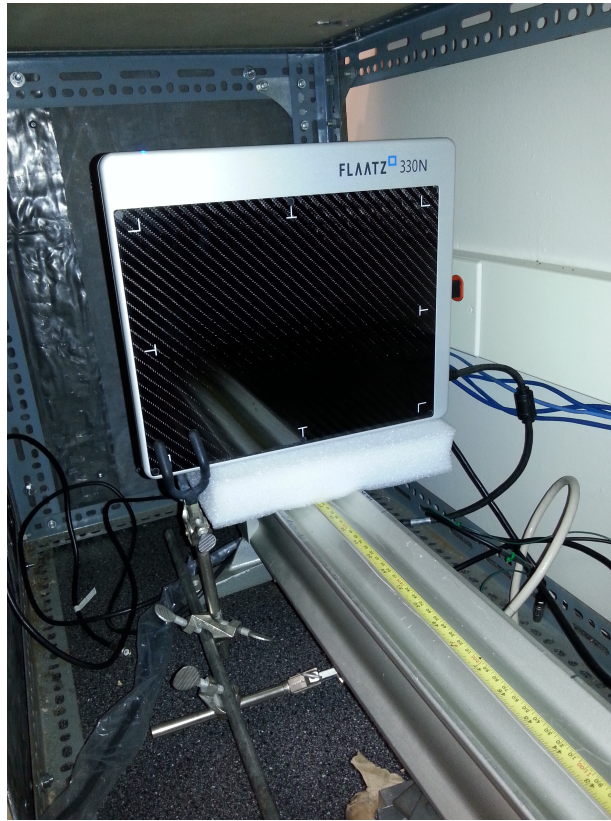


Figure I.7: Roberts Research Institute lab setup with FLAATZ-330N

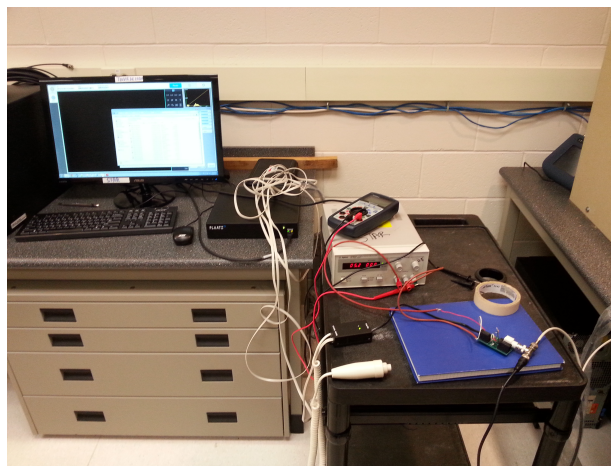


Figure I.8: Roberts Research Institute lab setup for FLAATZ-330N characterization

Glossary

a-Si amorphous silicon. 15, 29

ADC analog-to-digital converter. 15, 21

AKUH Aga Khan University Hospital. 33, 41, 42, 46, 47

anthropomorphic phantom A physical model of human anatomy for the purposes of x-ray imaging built to have similar density of mass as human body parts. 32, 33, 37

BNC Standard two-conductor cable connector. 16, 18, 19, 22, 62, 72

computed tomography a method to use x-rays to obtain images cross-sections of bodily organs. 3

COPD chronic obstructive pulmonary disease. 1

CR computed radiography. 3, 30

DB9 A nine-pin connector used for serial network communications. 18, 19, 72

DQE detective quantum efficiency. xii, 5, 7, 8, 22, 27–29, 31, 37, 46, 48, 51, 89

DQE(0) The DQE value at a spatial frequency of 0 cycles/mm. It must be extrapolated from measurements.. 28, 50

efficacy the ability to produce the intended result. 4, 7, 8, 10, 33, 46, 49, 51, 77

ESF edge spread function. vi, xiii, 4, 5, 8, 27, 34–37, 47

film-screen Light-sensitive film, potentially coupled with an x-ray-sensitive phosphorescent material, that requires development in a dark room.. iii, 3, 29, 50

fluoroscopy a technique to use x-rays to obtain real-time moving images. 3

FM fluorescence microscopy. 2

FPGA field programmable gate array. xii, 16–19, 24, 50, 52, 57, 62

frame A raw x-ray image from the x-ray detector; the pixel array values. x, 15–20, 27, 52, 71

Gadox Common name for $\text{Gd}_2\text{O}_2\text{S}$, an inexpensive scintillator material used in indirect conversion x-ray devices. 15, 21

GPIO general purpose input/output. 18, 19

HDMI high-definition multimedia interface. 19, 23

IC integrated circuit. 19

kVp peak kilovoltage, used to measure the energy of an x-ray beam. 11, 22

LED light emitting diode. xii, 2, 16, 17

LSF line spread function. vi, xii, xiii, 4–6, 8, 27, 28, 34, 36, 47

LVDS low-voltage differential signaling. 18, 19, 62, 72

mammography a technique to use x-rays to locate tumors in breasts. 3, 29

MTF modulation transfer function. xiii, 5–8, 20, 27–31, 34, 36–38, 47, 48, 50, 51, 73–76, 89

N/C Not connected. 19

NAAT nucleic acid amplification test. 2

NPS noise power spectrum. xii, 5, 7, 8, 27–29, 31, 37, 47, 48, 89

PC personal computer. 11, 19, 20, 22–24

PCB printed circuit board. 14, 19, 22, 24

PCI peripheral component interconnect. 15, 16, 18, 20, 23, 24

phantom a specially designed object that is used in medical imaging to characterize or tune an imaging device. xiii, xiv, 26, 32–34, 37, 38, 53, 91

QA quality assurance. 26, 27

region-of-interest In radiography, a term that means to focus on one particular area of interest. e.g. looking at solely the lungs rather than the full chest, when screening for tuberculosis. 1, 10, 77

scintillator a phosphor-based material that absorbs x-ray photons and emits visible-spectrum light. 4, 15, 20, 29, 48

sensitivity proportion of positive test results that are correctly identified as such. 7, 8, 39, 40, 42, 45

SNR signal-to-noise ratio. 7

specificity proportion of negative test results that are correctly identified as such. 7, 8, 39, 41–45

TB tuberculosis. 1, 2, 8, 39–42, 44, 51

tele-medicine Medical diagnosis over internet or cellular networks. iii

tele-radiology Radiology diagnosis over internet or cellular networks. iii

TFT thin-film transistor. 4, 15, 21, 29, 30

throughput the number of patients that can be diagnosed per unit of time. 50

TTL transistor-transistor logic. 16, 22

VHDL very high-speed integrated circuit hardware description language. 17, 18, 49, 57

x-ray generator An electrical tool used to generate a beam of x-rays.. xii, 11–13, 15–17, 21, 22, 27, 34, 50

x-ray source A point from which x-rays are emitted. May also be synonymous with “x-ray generator”. x, 11–14, 16, 18, 20, 22, 26, 33, 50, 57, 62

XIS x-ray imaging software. 15, 16, 19, 20, 24

XRD x-ray detector. 19